Fall 11-15-2017

Integration of Thin Film TPV Cells to CVD Diamond Heat Spreaders

Emma J. Renteria
University of New Mexico

Follow this and additional works at: https://digitalrepository.unm.edu/ece_etds

Part of the Electronic Devices and Semiconductor Manufacturing Commons, Power and Energy Commons, and the Semiconductor and Optical Materials Commons

Recommended Citation

Emma J. Renteria
Candidate

Electrical & Computer Engineering
Department

This dissertation is approved, and it is acceptable in quality and form for publication:

Approved by the Dissertation Committee:

Dr. Ganesh Balakrishnan, Chairperson

Dr. Adam Hecht

Dr. Payman Zarkeh-Ha

Dr. Kyle Montgomery

Integration of Thin Film TPV Cells to CVD Diamond Heat Spreaders

by

EMMA J. RENTERIA

B.S in Chemical Engineering, The University of New Mexico, 2012

DISSERTATION

Submitted in Partial Fulfillment of the
Requirements for the Degree of

Doctor of Philosophy
Engineering

The University of New Mexico
Albuquerque, New Mexico

December 2017

ACKNOWLEDGEMENTS

Integration of Thin Film TPV Cells to CVD Diamond Heat Spreaders

EMMA J. RENTERIA

B.S in Chemical Engineering, The University of New Mexico, 2012

Ph.D., Electrical Engineering, The University of New Mexico, 2017

Abstract

In this work, techniques to isolate thermophotovoltaic (TPV) devices from the growth substrate and their subsequent integration with Chemical Vapor Deposition (CVD) diamond heat spreaders will be discussed, with the envisioned goal of fabricating thermally managed cells. CVD diamond heat spreaders are a great option for thermal management of TPV cells. The key requirement, however, is the bonding of the TPV cell directly onto the diamond wafer without the presence of thick (>350 μm) growth substrates, which can offer significant thermal resistance.

The first approach is to release GaSb epitaxial layers from GaSb substrates. However, this is challenging due lack of highly selective etchants for the GaSb/AlSb/InAs system. Nonetheless, small areas of GaSb films were released.

Another option is to grow GaSb TPVs on GaAs substrates. Taking full advantage of the highly selective etch chemistry of GaAs/AlAs systems large area GaSb thin-films were released from GaAs substrates. However, the threading dislocations due to the 7.8 % mismatch between GaSb and GaAs resulted in devices with poor performance.

Finally, the fabrication and integration of thin film TPV cells to CVD diamond is demonstrated by growing InGaAs TPV cells on InP substrates. Lattice-matched InGaAs/InP is the ideal system since there are no threading dislocations and the system offers high etch selectivity. The many challenges in achieving freestanding thin film TPV devices are described along with structural and electrical characterization data.

TABLE OF CONTENTS

LIST OF FIGURES

viii

LIST OF TABLES

Chapter 1: Introduction

1.1 Generation of Electricity by Thermophotovoltaic Systems

The conversion of heat energy into electrical energy by thermophotovoltaic (TPV) systems is a two-step conversion process [1]. First, heat is converted to light through incandescence and then light is converted to electrical energy by a photovoltaic (PV) cell [1]. Fig 1.1 shows a schematic of the basic components of a TPV system. The first component is the source of thermal energy which can be from the combustion of fossil fuels, waste heat, nuclear energy, or solar energy. The thermal source is used to heat an emitter which is the second component of the TPV system. The emitter is essentially a black body that emits radiative power to the PV cell. The third component, the PV cell, converts the incoming radiation energy into electrical energy and heat. The heat is an unwanted product and it must be removed from the cell to avoid a decrease in efficiency of the cell. Hence, the fourth component of the TPV system is a heatsink.
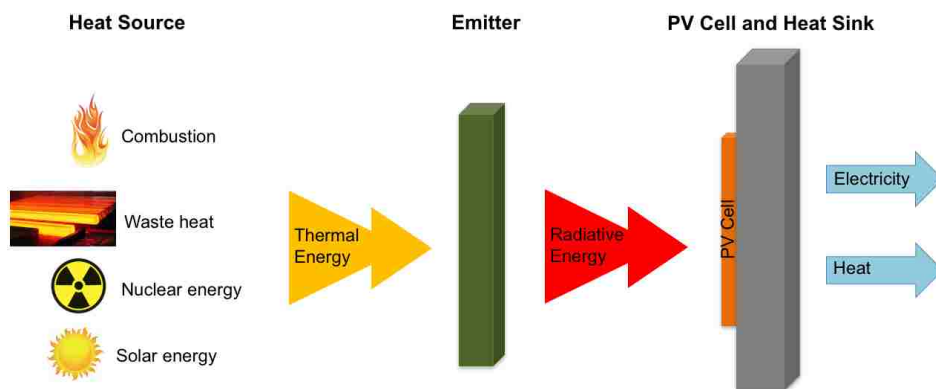
FIG. 1.1 SCHEMATIC OF THE BASIC COMPONENTS OF A TPV SYSTEM

To maximize the efficiency of the TPV system, three things must be considered. First, the heat

1

losses from the heat source to the emitter must be minimized so that most of the inputted thermal power is converted to radiative power. Second, the generation of heat in the cell must be minimized. Finally, the efficiency of the cell should be maximized.

1.1.1 Emitters and PV Cell Converters

To maximize the efficiency of the PV cell, the spectral sensitivity of the PV cell should be matched to the spectral distribution of the emitted radiation. The PV cell can only absorb photons with equal or greater energy than its bandgap energy. Hence, it would be ideal to match the bandgap of the PV cell to the wavelength where the emitter radiates the most power. However, the matching is not straightforward. Emitters are limited to temperatures of 1800 K due to the emission of high concentration of NO_x gases at high combustion temperatures [2]. This, in turn, limits the choice of semiconductor material for the PV cell.

The spectral irradiance emitted by the emitter can be approximated by Planck's radiation law [3].

$$F(\lambda) = \frac{2\pi hc^2}{\lambda^5 \left(exp\left(\frac{hc}{k\lambda T}\right) - 1 \right)}$$

where λ is the wavelength of light in meters, T is the temperature of the blackbody in Kelvin, F is the spectral irradiance in $Wm^{-2}\mu m^{-1}$, h is Planck's constant in J·s, c is the speed of light in m/s, and k is Boltzmann's constant in J/K.

Fig 1.2 shows the spectral irradiance of blackbodies at temperatures ranging from 1000 K to 1800 K which is the temperature range that emitters can operate at. At 1800 K, the spectral irradiance peaks at about 1.6 μm which corresponds to a bandgap of 0.77 eV. As the temperature of blackbody decreases, the emitted power density decreases and the spectral irradiance peak shifts to longer wavelengths which correspond to narrower bandgap

semiconductors. At the lowest temperature, 1000 K, the spectral irradiance peaks about 2.9 µm which corresponds to a bandgap of 0.42 eV. Hence, the bandgap energy of the TPV cell must be between 0.77 eV and 0.42 eV to maximize the absorption of photons radiated by the available emitters.
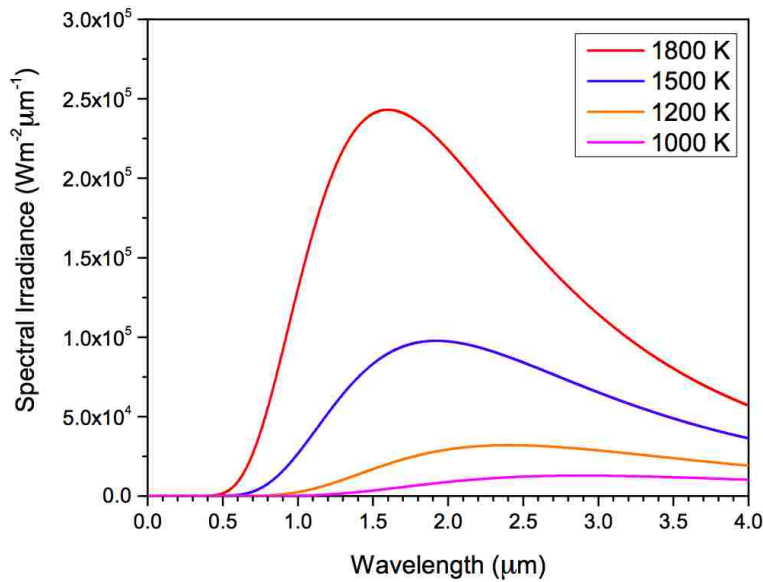
FIG. 1.2 SPECTRAL IRRADIANCE OF BLACKBODIES AT DIFFERENT TEMPERATURES

Yet another constraint is the availability of semiconductor materials at the bandgaps of interest. Fig 1.3 shows a plot of energy bandgap versus lattice constant for III-V semiconductor materials. TPV cells need to have energy bandgaps between 0.77 eV and 0.42 eV and must be grown on one of the commonly available substrates (GaAs, GaSb, or InP). The first obvious choice is GaSb. GaSb has a direct energy bandgap of 0.72 eV and p-n junction diodes can be grown on GaSb substrates. A second choice is an alloy that can be grown lattice-matched on GaSb substrates such as $In_xGa_{1-x}As_ySb_{1-y}$. Its energy bandgap can be varied from 0.40 to 0.70 eV by varying its composition. Yet another option is $In_{0.53}Ga_{0.47}As$ which is lattice matched to InP substrates and has an energy bandgap of 0.74 eV.
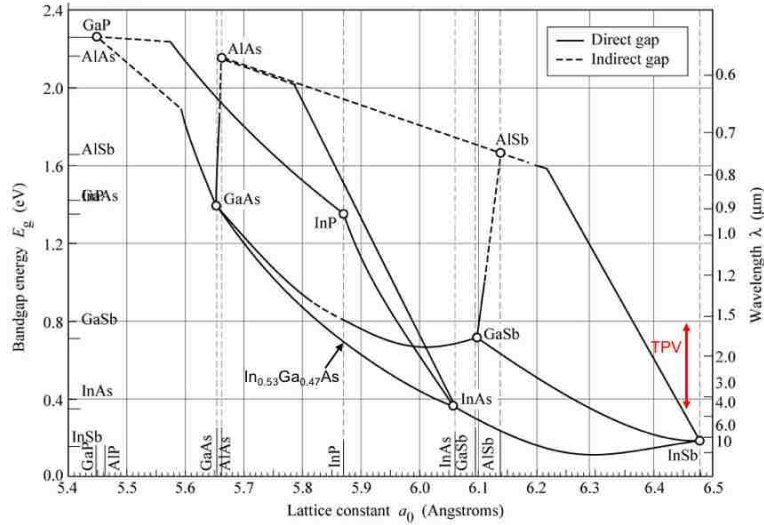
FIG. 1.3 LATTICE CONSTANT VERSUS ENERGY BANDGAP FOR III-V SEMICONDUCTOR MATERIALS

1.2 Basic Operation Principals of TPV Cells

The device principals of a TPV cell are the same as the ones of a conventional solar cell. The incident infrared photons are absorbed by the narrow bandgap TPV cell and the photogenerated charge carriers pass through an external load to do electrical work. Fig 1.4 shows a schematic diagram of the device geometry of a simple PV cell [4]. The n-region is narrow and heavily doped while the p-region is wider and with a lower doping concentration. The gradient in doping concentration allows for the diffusion of carriers from one side to the other until an electrostatic field, E_o, which opposes further diffusion is formed. Electrons from the heavily doped n-type layer diffuse into the p-type layer, recombine and create negatively charge ions on the p-type side. Holes from the p-type region diffuse into the n-type material, recombine, and create positively charged ions on the n-type side. The space formed by the charged ions is called space charge region or depletion region, W.

When the p-n junction is illuminated, the absorbed photons create electron-hole pairs (EHPs) in all regions. EPHs photogenerated in the space charge region are immediately separated by the

4

electrostatic field. The electrons drift to the neutral n-region making this side more negatively

charged. The holes drift to the neutral p-region making this p-side more positive. Electrons

photogenerated by the absorption of long wavelength photons in the neutral p-region must

diffuse to the depletion region where they can be drift to the n-side. Similarly, holes

photogenerated in the neutral n-region must diffuse to the depletion region where they can be

swept to the p-side. Diffusion of the EHPs can only happen within the minority carrier diffusion

lengths L_h and L_e. Outside of these diffusion lengths, the photogenerated EHPs are lost by

recombination. Therefore, only EHPs photogenearated in the $L_h + W + L_e$ region can contribute

to the photovoltaic effect. Then, if an external load is connected, the excess electrons in the n-

side can travel around the external circuit, do work, and reach the p-side to recombine with the

excess holes there.
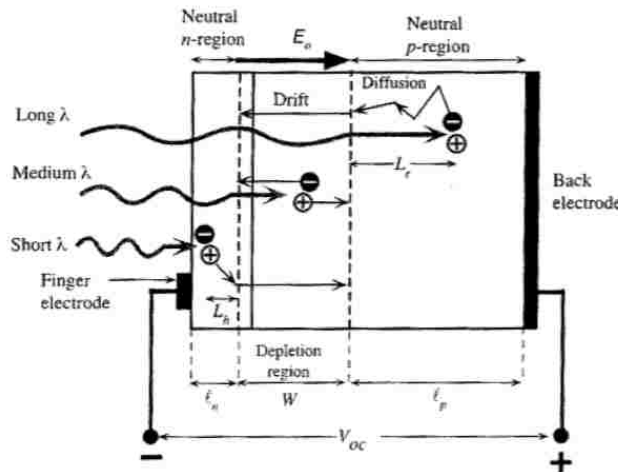
FIG. 1.4 DEVICE GEOMETRY OF A SIMPLE PV CELL (TAKEN FROM [4])

The current voltage characteristics of an ideal photovoltaic cell can be described by the

Shockley diode equation [5],

$$J = J_0 \left(e^{\frac{qV}{kT}} - 1 \right) - J_{sc}$$

where J_o is the dark saturation current density, q is the electronic charge, V is the voltage, k is Boltzmann's constant, T is the temperature of the cell in Kelvin, and J_{sc} is the photocurrent density generated by the solar cell under illumination at short circuit.

The dark saturation current density is highly dependent on the material properties of the PV cell. For direct bandgap materials where absorption is strong, recombination within the depletion region is dominant and hence [6],

$$J_o \approx J_{src,o} = \frac{qn_i(w_n + w_p)}{\sqrt{\tau_n \tau_p}}$$

where q is the electronic charge, n_i is the intrinsic carrier concentration, w_n and w_p are thickness of depletion region in the n-layer and the p-layer, τ_n and τ_p are the electron and hole lifetimes, respectively.

When recombination is dominant by the diffusion process, the dark saturation current density can be approximated by [6],

$$J_o \approx J_{diff,o} = qn_i^2 \left(\frac{D_n}{N_a L_n} + \frac{D_p}{N_d L_p} \right)$$

where D_n and D_p are the electron and hole diffusion coefficients, N_a and N_d are the acceptor and donor doping concentrations, and L_n and L_p are the electron and hole diffusion lengths. Nonetheless, the PV cell not only absorbs radiation but also emits radiation and this affects the dark saturation current as well [5]. Frequently, solar cell's models use an approximation formula for J_o as follows [5],

$$J_o \approx \beta_{(hv_g)} T_{cell}^3 e^{\frac{hv_g}{kT_{cell}}}$$

where

$$\beta_{(hv_g)Wanlass} = 3.165 \cdot 10^{-4} \frac{A}{cm^2 K^3} e^{2.91 hv_g}$$

The dark saturation current density experimental value of a solar cell can be calculated from the J-V characteristics of the solar cell. Rearranging the ideal diode equation with $J = 0$, J_o can be approximated by

$$J_o = \frac{J_{sc}}{e^{\frac{qV_{oc}}{kT}} - 1}$$

J_o is highly dependent on the bandgap of the solar cell. Fig 1.5 shows dark saturation current density vs. bandgap for several TPV materials [5]. As the bandgap energy of the material increases the dark saturation current decreases. GaSb and InGaAs TPVs have a dark saturation current density of about 1 x 10^{-8} A/cm^2 [5].
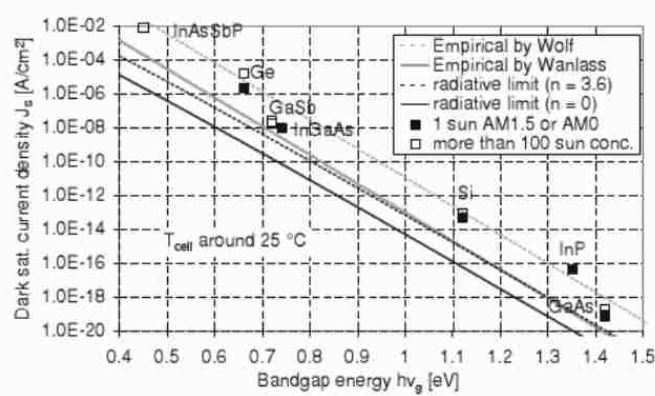
FIG. 1.5 DARK SATURATION CURRENT DENSITY VS. BANDGAP FOR DIFFERENT TPV MATERIALS [TAKEN FROM []]

The short circuit current density generated by an ideal PV cell is given by the following equation [6],

$$J_{sc} = q \int_{E_g}^{\infty} b_s(E)QE(E)dE$$

where q is the electronic charge, $b_s(E)$ is the incident spectral photon flux density, and QE(E) is the probability that an incident photon of energy E will deliver one electron to the external circuit.

The maximum short circuit current density, $J_{sc,max}$, that a PV cell can have is when all absorbed photons with energies greater than the bandgap deliver one electron to the external load that is when quantum efficiency QE(E) = 1. Then, $J_{sc,max}$ only depends on the incident photon flux and the bandgap energy of the PV cell.

$$J_{sc,max} = q \int_{E_g}^{\infty} b_s(E)dE$$

For example, the maximum photocurrent density that a GaSb PV cell can achieve under the illumination of the standard AM1.5G spectrum is 59.5 mA/cm^2. AM1.5G is the standard solar spectrum at the Earth's surface, G stands for global and includes both direct and diffuse radiation [7]. The standard AM1.5G spectrum has been normalized to give 1kW/m^2 [7]. For TPV systems, there is no standard as the radiated spectrum depends on the temperature of the heat source and the type of emitter. Research TPV cells are often characterized under solar spectrum conditions.

Fig 1.6 shows the current-voltage characteristics of an ideal solar cell under dark and light conditions. In the dark, no photocurrent density is generated by photons and hence J_{sc} is zero. Under illumination, in an ideal situation, each photon above the bandgap, E_g, contributes to the generation of current and hence the current-voltage curve is shifted down by J_{sc} to the fourth quadrant [5].
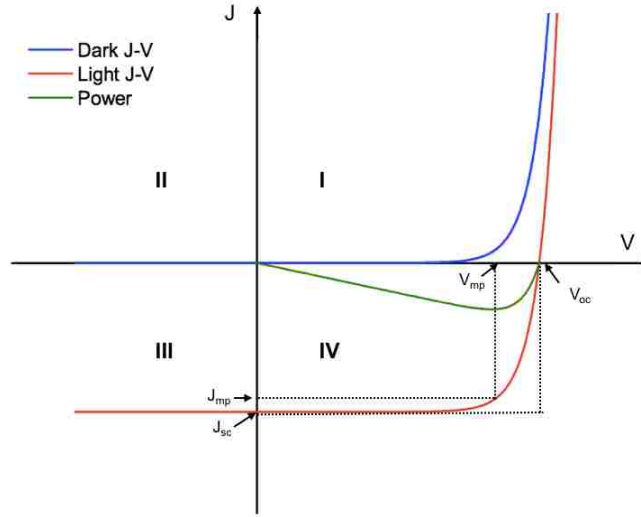
FIG 1.6 CURRENT-VOLTAGE CHARACTERISTICS OF AN IDEAL SOLAR CELL UNDER DARK AND LIGHT CONDITIONS

A solar cell has four key performance characteristics; The short circuit current density, J_{sc}, the open-circuit voltage, V_{oc}, the fill factor, FF, and the efficiency, η [6]. J_{sc} and V_{oc} can be obtained directly from the current-voltage curve as shown in Fig 1.6. V_{oc} is the maximum possible voltage of the cell and it happens when the dark current is equal to the short circuit photocurrent. From the ideal diode equation V_{oc} is,

$$V_{oc} = \frac{kT}{q} ln\left(\frac{J_{sc}}{J_o} + 1\right)$$

Ideally, the maximum possible power for the cell will be the product of J_{sc} and V_{oc}. However, J_{sc} and V_{oc} do not occur simultaneously and at each point the power is zero as shown by the power curve in Fig 1.6. There is a specific current density J_{mp} and voltage V_{mp} where the cell produces the maximum power density.

The Fill Factor FF compares the maximum power density produced by the cell to the maximum possible power that the cell could have as shown by the following equation [6],

$$FF = \frac{J_{mp}V_{mp}}{J_{sc}V_{oc}}$$

9

The FF is a measure of the closeness of the solar cell J-V curve to the ideal rectangular shape.

The efficiency, η, of the cell is the ratio between the maximum power density, P_{max}, deliver by the cell and the incident light power density, P_{in}[6].

$$\eta = \frac{P_{max}}{P_{in}} = \frac{J_{mp}V_{mp}}{P_{in}} = \frac{J_{sc}V_{oc}FF}{P_{in}}$$

The performance characteristics of the TPV cells in this thesis are evaluated by the four parameters mentioned.

1.3 Heat Transfer in TPV Systems

The transport of thermal energy in a TPV system includes all modes of heat transfer conduction, convection, and radiation. Fig 1.7 shows a schematic of the arrangement of a typical TPV system [5]. Different combinations of heat transfer can happen in the different sections of the TPV system. The system is arranged in three main sections: a heat source thermally connected to the radiator, a heat sink thermally connected to the PV cells, and the cavity between the radiator and the PV cells. The cavity of the system includes the radiator, the heat shield, the optical filter, and the PV cells. In the cavity, the maximization of radiative heat transfer and minimization of conductive and convective heat transfer are extremely important for the efficiency of the TPV system. Nonetheless, conduction and convection are essential for the uniform heating of the radiator and effective cooling of the TPV cells. The following sections explain in more detail the three heat transfer modes and the cooling of TPV cells.
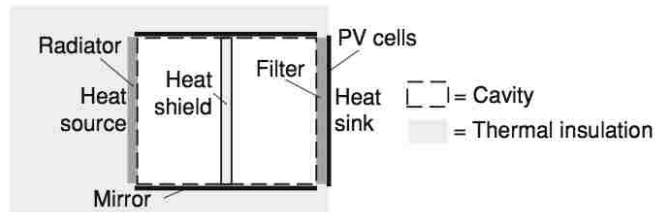
FIG 1.7 SCHEMATIC OF A TYPICAL TPV SYSTEM WITH CAVITY (TAKEN FROM [5])

1.3.1 Conduction

The conduction heat transfer rate in a thermal system under steady-state conditions can be estimated by [5],

$$P = \frac{T_h - T_c}{R_{th}}$$

Where R_{th} is thermal resistance of the material in K/W, T_h is the temperature of the hot surface in Kelvin, and T_c is the temperature of the cold surface in Kelvin. In a TPV system, high conduction heat transfer is important to achieve a uniform radiator surface temperature, and to efficiently transfer the heat generated in the TPV cell to the heat sink [5].

1.3.2 Convection

Convection is the transfer of heat from a surface to another by the combined action of fluid movement and conduction heat transfer [5]. The convective heat transfer rate is given by [5],

$$H = h(T_w - T_F)$$

Where h is the convective heat transfer coefficient in W/(m^{2}K), T_w is the wall temperature, and T_F is the fluid temperature.

Undesirable convective heat transfer can happen in the TPV system as there may be gas inside the TPV cavity. To protect the PV cells from convective heat transfer and combustion products, a transparent high-temperature heat shield can be placed between the radiator and the PV Cell [8]. On the other hand, convection heat transfer is useful to cool the PV cells and to transfer heat from the combustion zone to the emitter [5].

1.3.3 Radiation

Radiative heat transfer in the cavity of a TPV system is desired and should be optimized to achieve high electrical power densities and high efficiencies [8]. As mentioned before, to maximize the

efficiency of the TVP cell, the spectral radiation distribution from the emitter should be matched

to the spectral sensitivity of the TPV cell. Radiative heat transfer of photons with energies larger

than the cell bandgap should be maximized and heat transfer of photons with energies lower than

the cell bandgap should be minimized [5]. This can be achieved by using selective emitters with

high emissivity in the desired wavelengths and by using filters on the surface of the PV cell that

can reflect longer wavelengths back to the emitter [8-9]. Spatial radiation distribution is also

required in TPV systems as the PV cell in the modules should be illuminated uniformly for optimal

performance [8].

The net radiative heat transfer from a hot plate to a cold plate can be calculated by [5],

$$H = \sigma \cdot (T_h^4 - T_c^4) \cdot F_{h-c}$$

Where is σ the Stefan–Boltzmann constant, T_h is the temperature of the hot plate or the radiator,

T_c is the temperature of the cold plate or the PV cell, and F_{h-c} is the view factor. This radiative

heat transfer equation assumes two isothermal blackbody surfaces with no medium between

them. For an infinite parallel plate arrangement, the view factor is equal to one. The radiative

heat transfer between the surfaces of the TPV cavity is highly dependent on the absolute

temperature of the surfaces and the geometry of the cavity.

1.3.4 Cooling of TPV Cells

Unlike PV cells, TPV cells must be placed very close to the heat source. This proximity to the

heat source exposes the TPV cell to conductive and convective heat transfer which can generate

a lot of heat in the cell in addition to the heat generated from radiation not converted to

electricity. The heat generated in the photocell must be removed as it degrades the performance

and lifetime of TPV device. For maximum efficiency, the operating temperature of the TPV cell

12

needs to be kept below 80°C [9]. As mention in the previous section, the use of selective

emitters, SiO_2 heat shields, optical filters, and back surface reflectors minimizes the heating of

the TPV cell [8-10]. However, while radiation losses can be minimized, they cannot be

eliminated completely. Hence, maintaining the operation temperature of the TPV cell at nominal

levels is key to achieving high conversion efficiencies.

TPV systems have adopted the cooling techniques used in concentrated photovoltaics (CPV)

and power electronics [5]. Typically, PV cells in concentrated photovoltaic systems are

thermally connected to a heat sink that is cooled by air or water. The PV cells cannot be placed

directly on the metal heat sink as they must be arranged in series to form modules. Hence, PV

cells must be placed on a substrate that is an electrical insulator and a thermal conductor at the

same time [11]. The same is true for the PV cells in a TPV system.

The solution to this problem is to use printed circuit boards (PCB) in a manner similar to its

usage in power electronics [11]. There are two main types of PCBs as shown in Fig 1.8. The

first one is a directly bonded copper substrate (DBC) where the top surface of a ceramic substrate

is patterned with copper to solder the cells and the bottom surface of the substrate is covered

with copper to solder the DBC to the heat sink [11]. The second is an insulated metal substrate

(IMS) where a metal base-plate is covered by a dielectric that is then patterned with copper for

the interconnection of the devices [11].
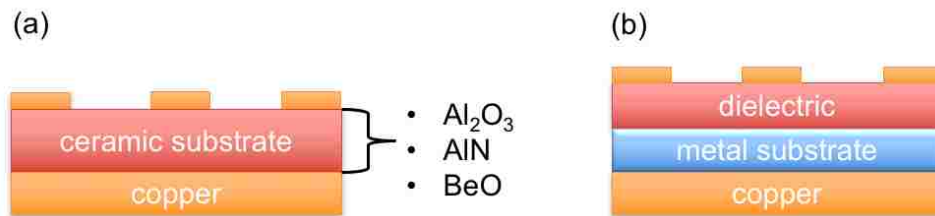
FIG. 1.8 SCHEMATIC OF THE AVAILABLE PRINTED CIRCUIT BOARDS; (A) DIRECTLY BONDED COPPER SUBSTRATE (DBC)
AND (B) INSULATED METAL SUBSTRATE (IMS)

For CPV and TPV cells, DBCs are preferred [12]. Khvostikov *et al*. used patterned Beryllium oxide (BeO) ceramic plates to connect GaSb TPV cells in series [13]. BeO has a good thermal conductivity and its thermal expansion coefficient is close to that of the GaSb cells which is important to avoid mechanical stress. Aluminium nitride (AlN) substrates have also been used for the integration of GaSb TPV cells into modules [14]. However, AlN has a lower thermal conductivity than BeO (material properties are summarized in table 1.1).

TABLE 1.1. Thermal properties of materials in the cell-to-sink interconnect (adapted from [5])

	Material (µm)	Thermal Conductivity (W cm^{-1} K^{-1})	Thermal expansion coefficient (K^{-1})	Thermal resistance for 1 cm^2 (K/A)
Growth substrates	GaAs 500	0.55	5.7×10^{-6}	0.091
	GaSb 500	0.32	7.7×10^{-6}	0.1562
	InP 500	0.68	4.6×10^{-6}	0.0735
Solder	Sn/Ag 100	0.50	25×10^{-6}	0.0200
	Indium 3	0.86	25×10^{-6}	0.0003
Conductor	Copper 100	4.00	17×10^{-6}	0.0025
	Gold 1	3.18	14×10^{-6}	0.0000
Ceramic substrates	AlN 635	1.80	4.5×10^{-6}	0.0350
	BeO 635	2.80	7×10^{-6}	0.0230
Heat spreader	CVD diamond 300	18.00	1×10^{-6}	0.0017

For efficient heat removal, the global thermal resistance in the interconnect between the TPV cell and the heat sink must be minimized. The heat generated in the p-n junction of the TPV cell has to travel through the growth substrate, the solder level used to bond the cells to the DBC, the copper layer that patterns the DBC, the DBC's ceramic substrate, and finally the copper layer that connects the DBC to the heat sink. A schematic of such thermal stack is shown in Fig 1.9.

Table 1.1 summarizes the thermal properties of materials typically used in TPV thermal

stacks.   The global thermal resistance can be calculated by adding the individual thermal

resistance of each layer in the cell-to-sink interconnect. For example, the resulting global thermal

resistance of assembling a GaSb TPV cell with a BeO DBC is calculated to be 0.2059 K/W cm^{-2}

as summarized in table 1.2. About 76% of the global thermal resistance in the cell-to-sink

interconnect is due to the GaSb substrate. The next big contributor to the thermal resistance of

the stack is the BeO ceramic substrate of the DBC with about 11% of the total thermal resistance.

Hence, the global thermal resistance of the cell-to-sink interconnect could be reduced if the TPV

is isolated from the growth substrate and bonded to a heat spreader with higher thermal

conductivity than BeO.

TABLE 1.2. Calculating global thermal resistance for a GaSb cell assembly

	Material (µm)	Thermal resistance for 1 cm^2 (K/A)
Growth substrate	GaSb 500	0.1562
Solder	Sn/Ag 100	0.0200
Conductor	Copper 100	0.0025
Ceramic substrate	BeO 635	0.0230
Conductor	Copper 100	0.0025
	Total thermal resistance	0.2042

Single crystal diamonds have the highest thermal conductivity (4500 Wm^{-1}K^{-1} at 200°K) of

any known bulk material [15]. Diamond heat spreaders have the ability to spread localized thermal accumulation in semiconductor materials and have been successfully used for thermal management of high power lasers [15-16]. Unfortunately, their application in high-volume commercial applications is not feasible due to their low availability and high cost. A cheaper alternative to the single crystal diamond is the polycrystalline diamond synthesized via chemical vapor deposition (CVD). Optical grade CVD diamonds have thermal conductivity values (4000 $Wm^{-1}K^{-1}$ at 200°K) close to that of single crystal diamond [17]. In addition, they are commercially available in large area wafers (up to 6.3" in diameter) [17]. Therefore, CVD diamond heat spreaders are a great option for thermal management in TPV systems and in addition to superior heat dissipation it is also an electrical insulator.

The key requirement, however, is the bonding of the TPV cell directly onto the CVD diamond wafer without the presence of thick (> 350 μm) GaSb substrates. For this to happen, we must be able to isolate the TPV from the growth substrate, process the top and bottom contacts for the fragile thin film, and transfer it to the CVD diamond.

1.4 Epi-layer Isolation Techniques

The isolation of epitaxial films from their growth substrates can be achieved by two different techniques. The first technique is the removal of the substrate by completely etching it away using a selective etchant. The second technique is epitaxial lift-off (ELO), where a sacrificial layer is grown between the epitaxial layers of interest and the growth substrate, which is then laterally etched thus separating the two.

1.4.1 Substrate Removal Technique

In the substrate removal technique, the epitaxial layers are separated from their growth substrate

by completely dissolving the substrate. The epitaxial layers are protected with an etch stop layer that is grown between the epitaxial layers of interest and the substrate as shown in the schematic in Fig 1.10. The solution used to dissolve the substrate must have a higher affinity for the substrate than for the etch stop layer. Subsequently, if the etch stop layer needs to be removed, a highly selective etchant must be used to avoid damage to the material of interest.
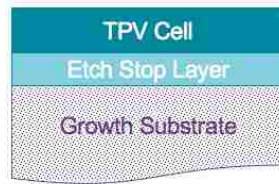
FIG. 1.10 SCHEMATIC OF STRUCTURE PREPARED FOR SUBSTRATE REMOVAL

A selective etchant will etch one semiconductor material faster than another. The selectivity between two materials can be calculated by [18]

$$Selectivity = \frac{Etch\ rate\ of\ material\ 1}{Etch\ rate\ of\ material\ 2}$$

Clawson *et al*. have published a review paper compiling literature on the chemical etching of III-V semiconductors for different applications [19]. It has a section for selective etchants for different material systems.

1.4.2 Epitaxial Lift-off Technique

In 1978, Konagai *et al*. described a technique to separate a 30 μm thick GaAs solar cell from a GaAs substrate by selectively etching a 5 μm thick $Al_{0.70}Ga_{0.30}As$ intermediate layer with hydrofluoric acid (HF) [20]. The samples were coated with black wax to protect the contacts (both n- and p-type contacts were processed on the top surface of the cell) and to provide support

to the thin film after separation. In 1987, Yablonovitch *et al*. revisited this technique, known today as epitaxial lift-off (ELO), and reported that there are two key elements to successfully lift off an epitaxial film from its substrate [21].

1. The selectivity between the intermediate layer and the film to be released must be extremely high. The selectivity of HF for AlAs over $Al_{0.40}Ga_{0.60}As$ was reported to be about 10^7.

2. There must be curvature of the epitaxial film as the lateral etch progresses so that there is space for the exchange of etchant and reaction products.

This ELO technique has become of great interest as it could potentially decrease the cost of III-V solar cells through the reuse of the substrate. Since Yablonovitch *et al*.'s published results, much research has been done by different groups to improve the ELO technique.

A group from Radboud University Nijmegen, the Netherlands focused on increasing the radius of curvature of the epitaxial layer to accelerate the lateral etch rate of the sacrificial layer [22-23]. Fig 1.11 shows the two methods used to increase the curvature (figure from [24]). In both methods, the epitaxial surface is first covered with gold or copper to counteract the tension of the wax and prevent crack formation in the thin film [25]. Then a flexible carrier is bonded to the metallized surface with wax to support the thin film after the ELO. In the first method, the sample is mounted upside down with a weight attached to the flexible carrier to help in the separation of the epitaxial film. In the second method, a cylinder is used to control the radius of curvature by guiding the film as it is being separated from the substrate. These configurations were successful in releasing 1 μm thick GaAs layer from a 2 inch GaAs substrate.

Several other groups have also focused on demonstrating the feasibility of reusing the ELO substrate [26-28]. After ELO, the substrate is left with a rough surface and reaction residues, and hence it must be treated before reuse [26]. Forrest *et al*. have developed a non-destructive ELO technique that uses protective layers to avoid damage to the substrate [27]. They have also left out the usage of black wax and instead bond the metalized surface of the sample to a metalized Kapton film by cold bonding.

The ELO is also being incorporated in several commercial products. Alta Devices Inc. has the best efficiency record for single-junction GaAs solar cells under one sun illumination [29]. Meanwhile, MicroLink Devices have developed epitaxial lift-off process for GaAs- and InP-based materials at a wafer scale to fabricate thin-film multi-junction solar cells [30-31].

1.5 Thesis Overview

Lee *et al.* observed that thin-film GaAs solar cells used with non-tracking mini-concentrators to reduce the cost of CPV systems would heat less than the substrate base GaAs solar cells [32]. Therefore, thin-film TPV cells could have the same effect as these thin-film GaAs CPV cells. In addition to being thermally managed, the thin-film TPV cells have the added advantage of being

able to have effective back surface reflectors that can send the transmitted below-bandgap photons back to the emitter. Recycled photon's energy can be used to reheat the emitter. The metal back-contact of the thin film cells acts as an optical mirror that reflects unabsorbed photons back into the cell increasing their optical path and their chance to be reabsorbed or be reflected to the emitter. The thick solar cells do not have this effect because photons escape into the substrate. Using the photon-recycling effect of thin-film cells with highly reflective mirror, Scranton *et al*. predicted a theoretical efficiency of 48.2% for a thin-film $In_{0.53}Ga_{0.47}As$ photovoltaic cell with a rear reflectivity of 98% at a source temperature of 1200 ºC and a cell temperature of 20º C [33]. Therefore, thin-film TPV cells have a great potential to maximize the overall efficiency of the TPV system. In this thesis, the focus is on developing a process to achieve freestanding TPV cells that can be then transferred and bonded to CVD diamond heat spreaders.

Chapter 2 explains the challenges involved in the growth and isolation of large area GaSb devices from GaSb substrates. Despite being lattice-matched, the growth of GaSb epi-layers on GaSb substrates by molecular beam epitaxy (MBE) can result in a high density of defects. These growth defects inhibit the diode behavior of large area GaSb TPV cells. Chapter 2 explains the origin of these defects and what was done to mitigate them and achieve large area GaSb cells with good performance. Also, the chapter presents the challenges and attempts to isolate the GaSb epitaxial films from GaSb substrates.

In chapter 3, an alternative method for the realization of thin film GaSb TPVs is explored. GaSb devices are grown on GaAs substrates to take advantage of the GaAs/AlAs etch chemistry. The chapter starts by explaining the growth technique used to grow fully relaxed GaSb epitaxial layers on GaAs substrates despite the 7.8 % lattice mismatch. Then, an extensive study of the

etch contrast between GaSb and GaAs is presented along with its effect for the successful isolation of GaSb membranes from GaAs substrates by substrate removal and epitaxial lift-off. Finally, the fabrication and integration of thin film metamorphic GaSb diodes are described.

Chapter 4 presents two optimization techniques to reduce the amount of remaining threading dislocations in the metamorphic GaSb TPV cells. The first techniques focus on minimizing the formation of 60 ° misfit dislocations that result in threading dislocations and the second technique focuses on blocking the propagated threading dislocations. The dislocation density is calculated from plain view and cross-sectional transmission electron microscopy images and x-ray diffraction data. Finally, the threading dislocation density reduction is verified by the improvement of open-circuit voltage in the metamorphic GaSb cells.

Chapter 5 describes in detail the fabrication and integration of thin film InGaAs TPV cells to CVD diamond. InGaAs cells with a bandgap of 0.75 eV can be grown lattice-matched to InP substrates. This eliminates the problems of threading dislocations and growth defects found on the metamorphic GaSb cells and the lattice-matched GaSb cells. In addition, the InGaAs/InP system offers a highly selective etch chemistry. Hence, the focus of the chapter is in the development of a process to integrate freestanding thin film InGaAs cells to CVD diamond heat spreaders.

Finally, chapter 6 discusses conclusions and future work.

References

1. Wedlock, BRUCE D. "Thermo-photo-voltaic energy conversion." *Proceedings of the IEEE* 51, no. 5 (1963): 694-698.

2. Daneshvar, Hoofar, Rajiv Prinja, and Nazir P. Kherani. "Thermophotovoltaics: Fundamentals, challenges, and prospects." *Applied Energy* 159 (2015): 560-575.

3. Planck, Max. "On the law of distribution of energy in the normal spectrum." *Annalen der Physik* 4, no. 553 (1901): 1.

4. Kasap, Safa O. "Optoelectronics and Photonics: Principles and Practices." Prentice Hall, 2001

5. Bauer, Thomas. "Thermophotovoltaics: Basic Principales and Critical Aspects of System Design," Springer Berlin Heidelberg, 2011. ProQuest Ebook Central, http://ebookcentral.proquest.com/lib/unm/detail.action?docID=763551

6. Nelson, Jenny. "The Physics of Solar Cells," Imperial College Press, 2003.

7. Honsber, Christiana, and Stuart Bowden. "Air Mass." Air Mass PVEducation, www.pveducation.org/pvcdrom/2-properties-sunlight/air-mass.

8. Bauer, Thomas, Ian Forbes, R. Penlington, and N. Pearsall. "Heat transfer modelling in thermophotovoltaic cavities using glass media." *Solar energy materials and solar cells* vol. 88, pp. 257-268, 2005.

9. N. Cordero, R. Ginige, B. Corbett, and K. Kennedy. "Thermal modelling of TPV systems." in *Thermal and Thermomechanical Phenomena in Electronic Systems, 2002. ITHERM 2002. The Eighth Intersociety Conference on*, pp. 605-609, 2002.

10. C.A. Wang, P. G. Murphy, P. W. O'Brien, D. A. Shiau, A. C. Anderson, Z. L. Liau, D. M. DePoy, and G. Nichols. "Wafer-Bonded Internal Back-Surface Reflectors for Enhanced TPV Performance." In *Thermophotovoltaic generation of electricity: Fifth Conference on Thermophotovoltaic Generation of Electricity*, vol. 653, pp. 473-481, 2003.

11. Andreev, V. and Luque, A., 2007. Concentrator photovoltaics. *Springer Series In Optical Sciences, ed. Springer*.

12. Micheli, Leonardo, Eduardo F. Fernández, Florencia Almonacid, Tapas K. Mallick, and Greg P. Smestad. "Performance, limits and economic perspectives for passive cooling of High Concentrator Photovoltaics." *Solar Energy Materials and Solar Cells* 153 (2016): 164-178.

13. Khvostikov, V. P., P. Y. Gazaryan, O. A. Khvostikova, N. S. Potapovich, S. V. Sorokina, A. V. Malevskaya, M. Z. Shvarts, N. M. Shmidt, and V. M. Andreev. "GaSb Applications for

solar thermophotovoltaic conversion." In *AIP Conference Proceedings*, vol. 890, no. 1, pp. 139-148. AIP, 2007.

14. Schlegl, T., F. Dimroth, A. Ohm, and A. W. Bett. "TPV modules based on GaSb structures." In *AIP Conference Proceedings*, vol. 738, no. 1, pp. 285-293. AIP, 2004.

15. Dyment, J. C., and L. A. D'asaro. "Continuous operation of GaAs junction lasers on diamond heat sinks at 200° K." *Applied Physics Letters* 11, no. 9 (1967): 292-294.

16. Härkönen, A., S. Suomalainen, E. Saarinen, L. Orsila, R. Koskinen, O. Okhotnikov, S. Calvez, and M. Dawson. "4 W single-transverse mode VECSEL utilizing intra-cavity diamond heat spreader." *Electronics Letters* 42, no. 12 (2006): 693-694.

17. Sussmann, R. S., J. R. Brandon, S. E. Coe, C. S. J. Pickles, C. G. Sweeney, A. Wasenczuk, C. J. H. Wort, and C. N. Dodge. "CVD diamond: a new engineering material for thermal, dielectric and optical applications." *IDR. Industrial diamond review* 58, no. 578 (1998): 69-77.

18. LePore, J. J. "An improved technique for selective etching of GaAs and Ga1− x Al x As." *Journal of Applied Physics* 51, no. 12 (1980): 6441-6442.

19. Clawson, A. R. "Guide to references on III–V semiconductor chemical etching." *Materials Science and Engineering: R: Reports* 31, no. 1 (2001): 1-438.

20. Konagai, Makoto, Mitsunori Sugimoto, and Kiyoshi Takahashi. "High-efficiency GaAs thin film solar cells by peeled film technology." *Journal of crystal growth* 45 (1978): 277-280.

21. Yablonovitch, Eli, T. Gmitter, J. P. Harbison, and R. Bhat. "Extreme selectivity in the lift-off of epitaxial GaAs films." *Applied Physics Letters* 51, no. 26 (1987): 2222-2224.

22. Voncken, M. M. A. J., J. J. Schermer, G. Maduro, G. J. Bauhuis, P. Mulder, and P. K. Larsen. "Influence of radius of curvature on the lateral etch rate of the weight induced epitaxial lift-off process." *Materials Science and Engineering: B* 95, no. 3 (2002): 242-248.

23. Voncken, M. M. A. J., J. J. Schermer, G. J. Bauhuis, A. T. J. Van Niftrik, and P. K. Larsen. "Strain-accelerated HF etching of AlAs for epitaxial lift-off." *Journal of Physics: Condensed Matter* 16, no. 21 (2004): 3585.

24. Schermer, J. J., P. Mulder, G. J. Bauhuis, M. M. A. J. Voncken, J. Van Deelen, E. Haverkamp, and P. K. Larsen. "Epitaxial Lift-Off for large area thin film III/V devices." *physica status solidi (a)* 202, no. 4 (2005): 501-508.

25. Hageman, P. R., G. J. Bauhuis, A. Van Geelen, P. C. Van Rijsingen, J. J. Schermer, and L. J. Giling. "Large area, thin film epitaxial lift-off III/V solar cells." In Photovoltaic Specialists Conference, 1996., Conference Record of the Twenty Fifth IEEE, pp. 57-60. IEEE, 1996.

26. Bauhuis, G. J., P. Mulder, E. J. Haverkamp, J. J. Schermer, E. Bongers, G. Oomen, W. Köstler, and G. Strobl. "Wafer reuse for the repeated growth of III–V solar cells." *Progress in Photovoltaics: Research and Applications* 18, no. 3 (2010): 155-159.

27. Lee, Kyusang, Jeramy D. Zimmerman, Yifan Zhang, and Stephen R. Forrest. "Epitaxial lift-off of GaAs thin-film solar cells followed by substrate reuse." In *Photovoltaic Specialists Conference (PVSC), 2012 38th IEEE*, pp. 001698-001700. IEEE, 2012.

28. Cheng, Cheng-Wei, Kuen-Ting Shiu, Ning Li, Shu-Jen Han, Leathen Shi, and Devendra K. Sadana. "Epitaxial lift-off process for gallium arsenide substrate reuse and flexible electronics." *Nature communications* 4 (2013): 1577.

29. Kayes, Brendan M., Hui Nie, Rose Twist, Sylvia G. Spruytte, Frank Reinhardt, Isik C. Kizilyalli, and Gregg S. Higashi. "27.6% conversion efficiency, a new record for single-junction solar cells under 1 sun illumination." In *Photovoltaic Specialists Conference (PVSC), 2011 37th IEEE*, pp. 000004-000008. IEEE, 2011.

30. Tatavarti, Rao, G. Hillier, G. Martin, A. Wibowo, R. Navaratnarajah, F. Tuminello, D. Hertkorn, et al. "Lightweight, low-cost InGaP/GaAs dual-junction solar cells on 100 mm epitaxial liftoff (ELO) wafers." In *Photovoltaic Specialists Conference (PVSC), 2009 34th IEEE*, pp. 002065-002067. IEEE, 2009.

31. Youtsey, C., J. Adams, R. Chan, V. Elarde, G. Hillier, M. Osowski, D. McCallum et al. "Epitaxial lift-off of large-area GaAs thin-film multi-junction solar cells." In *Proc. of the CS MANTECH Conference (April 2012)*. 2012.

32. Lee, Kyusang, Jaesang Lee, Bryan A. Mazor, and Stephen R. Forrest. "Transforming the cost of solar-to-electrical energy conversion: Integrating thin-film GaAs solar cells with non-tracking mini-concentrators." *Light: Science and Applications* 4, no. 5 (2015): e288.

33. Scranton, Gregg, T. Patrick Xiao, Vidya Ganapati, John Holzrichter, Per F. Peterson, and Eli Yablonovitch. "Highly efficient thermophotovoltaics enabled by photon re-use." In *Photovoltaic Specialists Conference (PVSC), 2016 IEEE 43rd*, pp. 1026-1029. IEEE, 2016.

Chapter 2: Lattice-Matched GaSb TPV Cells

2.1 Introduction

Thermal sources for TPV generators typically operate in the temperature range of 1000 K to 1800 K due to the nature of hydrocarbon combustion and the thermal constraints of materials [1-2]. For high conversion efficiency, the cutoff wavelength of the photovoltaic cells should closely match the peak wavelength of the blackbody emission. GaSb has a direct energy bandgap of 0.72 eV which corresponds to a cutoff wavelength of 1.7 μm, and a temperature of 1700 K. GaSb photovoltaic cells are therefore an excellent choice for TPV applications as they can operate at the higher end of the thermal source temperature range.

GaSb photovoltaic devices were originally developed to boost the efficiency of GaAs/GaSb tandem solar cells [3]. These GaSb photovoltaic cells were fabricated by a pseudo-closed-box diffusion technique where a mixture of zinc and antimony is diffused into an n-type GaSb wafer to form the p-n junction. The diffusion creates a 0.5 μm thick Zn-doped (mid-10^{20} cm^3) p-type GaSb emitter. Realizing the potential for these GaSb infrared-sensitive photovoltaic cells in TPV applications, in 1993, JX Crystals Inc. obtained an exclusive license to this cell technology. The simple and inexpensive Zn-diffusion technique allowed JX Crystals Inc. to make GaSb thermophotovoltaic cells widely available in the market [4-5].

To this day, Zn-diffusion is the preferred method to fabricate GaSb TPV cells and this process, while effective, is limited to binary GaSb based devices. Recently, there has been an increased interest in growing GaSb cells by epitaxy to have more complex structures [6-8]. Epitaxial techniques allow for the growth of ternary and quaternary GaSb based alloys such as InGaSb and InGaAsSb which have lower bandgaps than GaSb [7-8]. Apart from the absorber,

epitaxy also allows for the addition of window and back-surface reflector layers, the control of the base and emitter thickness, the control of doping concentrations, and for change in polarity [7-10]. Beyond these features, epitaxial structures also allow for the possibility of monolithic multi-junction cells.

As mentioned in chapter 1, in this thesis, the main idea is to realize thin film (without substrate) TPV cells. Hence, the envisioned TPV cells must be grown by an epitaxial technique so that the substrate can be removed later. The GaSb cells are therefore grown by molecular beam epitaxy (MBE), which is the preferred epitaxial method for antimonide semiconductors. The following paragraphs describe the challenges involved with the growth and the removal of the substrate.

2.2 Development of Large Area GaSb TPV Cells on GaSb Substrates

The fabrication of efficient large area GaSb photovoltaics grown by MBE presents its own set of challenges due to defects produced during growth [11-14]. Despite being an instance of homoepitaxy, the growth of GaSb epi-layers on GaSb substrates results in a high density of defects that is detrimental to the performance of the devices. In this section, the defects shorting the GaSb TPV devices are described and methods to mitigate them are explored.

2.2.1 Defects that Inhibits Diode Behavior on Large Area MBE grown GaSb TPV Cells

While attempting to study the electrical characteristics of large area epitaxially grown (1 cm x 1cm) p-n GaSb diodes, it was found that almost 100% of the devices fabricated were completely shorted [14]. To uncover the mechanism behind these shorted devices a variety of parameters were studied including the fabrication of smaller (100 μm x 100μm) diodes. The change in device size resulted in better devices with some functional diodes, some extremely leaky diodes

and several that were still shorted. It was found that there was a strong correlation between the reverse bias current density and the number of defect on the diode surface as shown in Fig. 2.1 [12-14]. In Fig 2.1a and 2.1b, the current density versus voltage is plotted for a diode without defects and a diode with defects. The diode with defects shows scientifically higher leakage current than the one without defects. Any diode with more than eight defects shows resistor like properties. Hence, it was determined that the defects in question were responsible for the lack of large area epitaxial grown GaSb TPVs and to be able to fabricate large area GaSb TPV cells these defects must be eliminated or at least minimized.
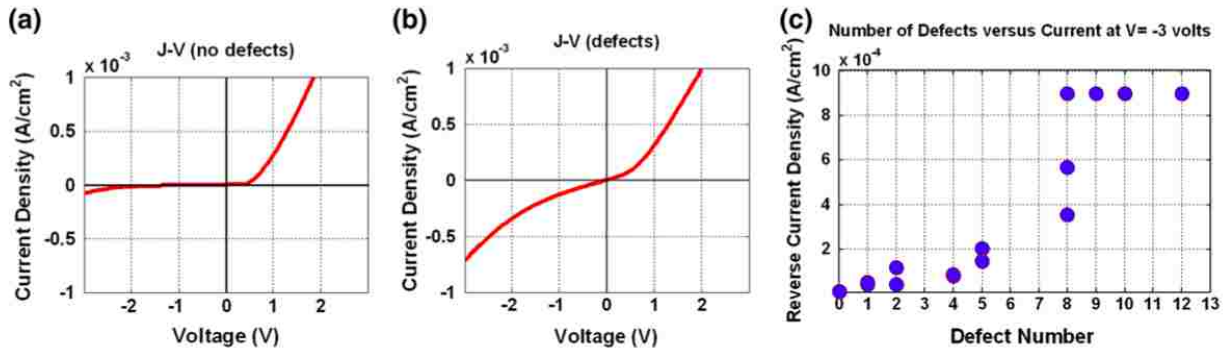
FIG. 2.1 CORRELATION BETWEEN REVERSE CURRENT DENSITY AND DEFECT NUMBER IN EPITAXIAL GASB DIODES: (A) J-V PLOT FOR A DIODE WITH LOW DEFECT DENSITY, (B) J-V PLOT FOR A DIODE WITH HIGH DEFECT DENSITY, AND (C) REVERSE BIAS CURRENT DENSITY VERSUS NUMBER OF DEFECTS (FROM [12]).

To determine the origin of such defects, the surface morphology of homoepitaxial GaSb films was analyzed by scanning electron microscopy (SEM), transmission electron microscopy (TEM), and electron dispersive spectroscopy (EDS). SEM images in Fig 2.2 show the two types of defects that were found [12]. The defect in Fig 2.2a is highly-faceted with pyramidal shape with a circular core in the middle which is present in all pyramidal defects. The defect in Fig 2.2b is an irregular defect that does not show any crystallographic shape.

27
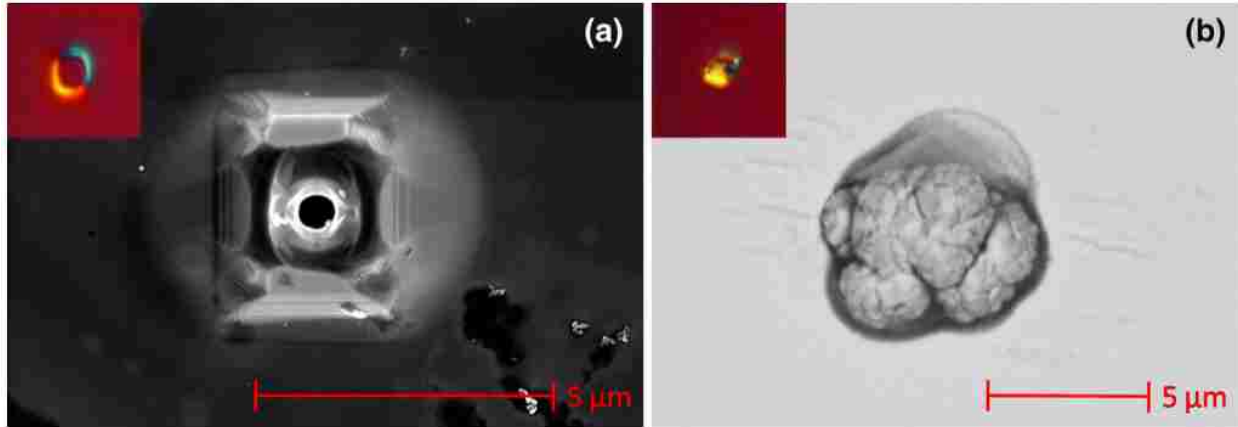
FIG. 2.2 SEM IMAGES OF VISIBLE SURFACE DEFECTS OF HOMOEPITAXIAL GaSb: (A) HIGHLY-FACETED DEFECT AND (B) IRREGULAR DEFECT. INSETS SHOW NOMARSKI MICROGRAPHS OF THE CORRESPONDING DEFECTS (FROM [12]).

EDS analysis of the irregular defect core indicates that it is amorphous or poly-crystalline GaSb [12]. The source of the irregular defect was found to be contaminants on the surface of the GaSb substrate. Fig 2.3 shows a cross-sectional transmission electron microscopy (XTEM) image of the irregular defect [13]. It can be observed that the defect forms over a foreign object that is at the substrate/epi interface. An EDS line scan across the foreign object detected high concentrations of oxygen and silicon as shown in Fig 2.4. In addition to oxygen and silicon, an EDS area scan shows low concentrations of Fe, Mg, and Al as shown by the EDS spectrum in Fig 2.5. The inset XTEM image shows the area of irregular defect that was scanned. It can be concluded that the contaminants on the surface of the substrate are due to polishing remnants and failure of oxide thermal desorption. GaSb substrate technology is not as mature as GaAs and InP and hence the high density of defects on GaSb homoepitaxy compared to other material systems is well documented [15-17]. For instance, Haugan *et al.* observed that quality of InAs/GaSb type-II superlattices were highly dependent on the substrate that they were grown in (wafers from three different manufactures were tested) [17].

28
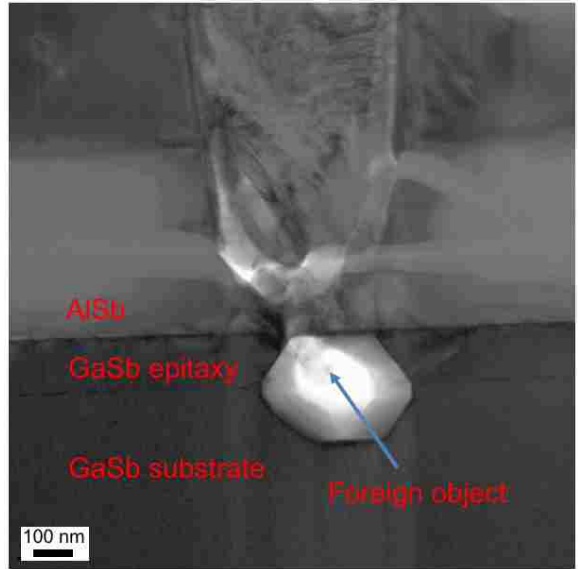
FIG. 2.3 XTEM IMAGE OF IRREGULAR DEFECT
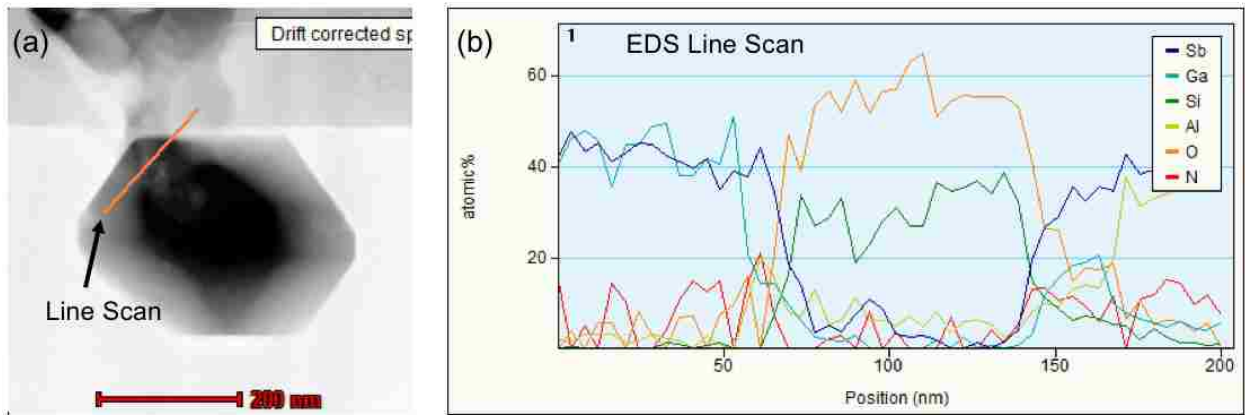
FIG. 2.4 XTEM AND EDS ANALYSIS OF IRREGULAR DEFECT: (A) XTEM SHOWING EDS LINE SCAN OF THE FOREIGN OBJECT THAT CAUSED THE IRREGULAR DEFECT; (B) EDS LINE SCAN SHOWING HIGH COMPOSITIONS OF OXYGEN AND SILICON.
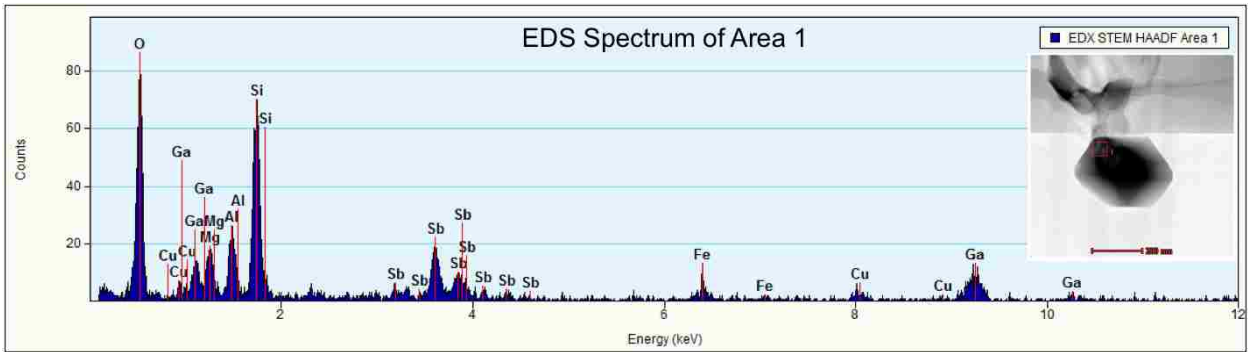
FIG. 2.5 EDS SPECTRUM OF AREA 1. THE INSET XTEM IMAGE SHOWS THE AREA OF IRREGULAR DEFECT THAT WAS SCANNED.

The highly-faceted defect does not originate at the substrate/epi interface; it forms at some point in the epitaxial layer as shown by the XTEM image in Fig. 2.6. An EDS line scan across the defect source detected high concentrations of gallium as shown in Fig 2.7. It is believed that origin of these highly-faceted defects is due to the ejection of Ga droplets from the Ga effusion cell during growth. When such droplets are found on the surface, they have a characteristic oval shape and are hence called "oval defects." Fig 2.8 shows SEM images of an oval defect and a pyramidal defect along with their respective EDS spectrum. The EDS spectrum of the oval defect core, Fig 2.8c indicates that is pure gallium and is hence a Ga droplet. The EDS analysis, Fig 2.8d, of the pyramidal defect indicates the presence of Ga and Sb. We, therefore, hypothesize that the highly-faceted defect starts as a Ga droplet (an oval defect) and ends as a GaSb pyramid.
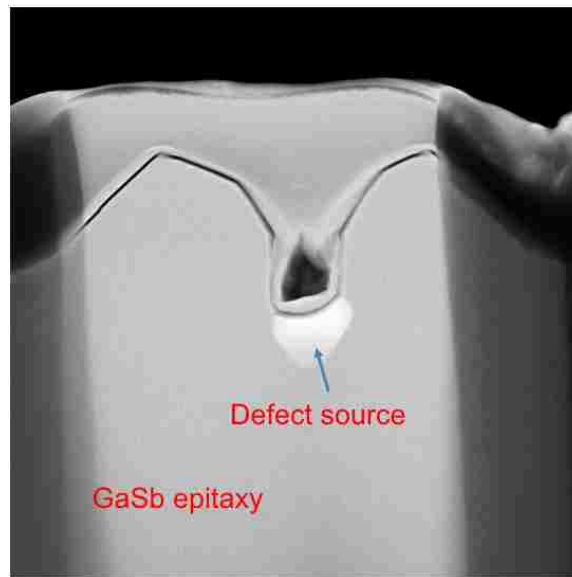
FIG. 2.6 XTEM IMAGE OF HIGHLY-FACETED DEFECT
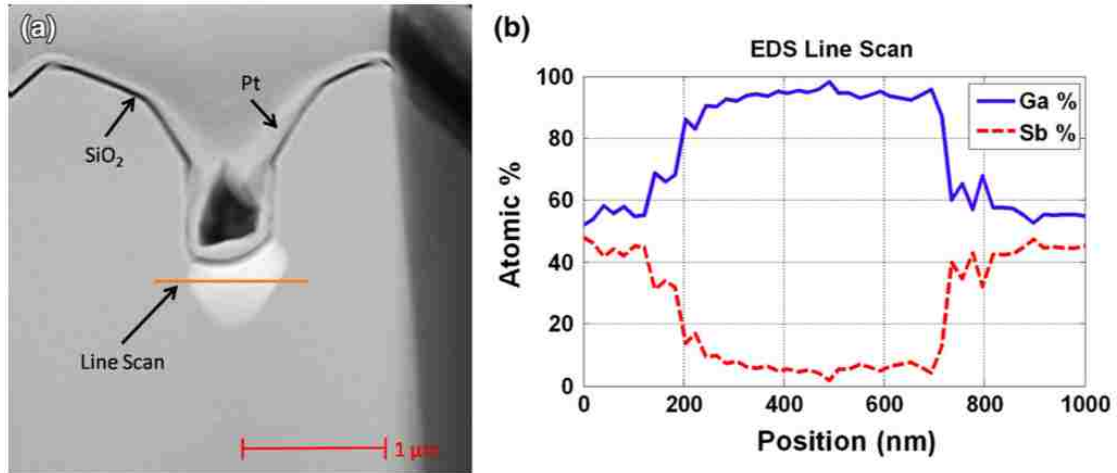
FIG. 2.7 XTEM AND EDS ANALYSIS OF HIGHLY-FACETED: (A) XTEM SHOWING EDS LINE SCAN OF THE DEFECT SOURCE; (B) EDS LINE SCAN SHOWING HIGH COMPOSITIONS OF GALLIUM (FROM [12]).
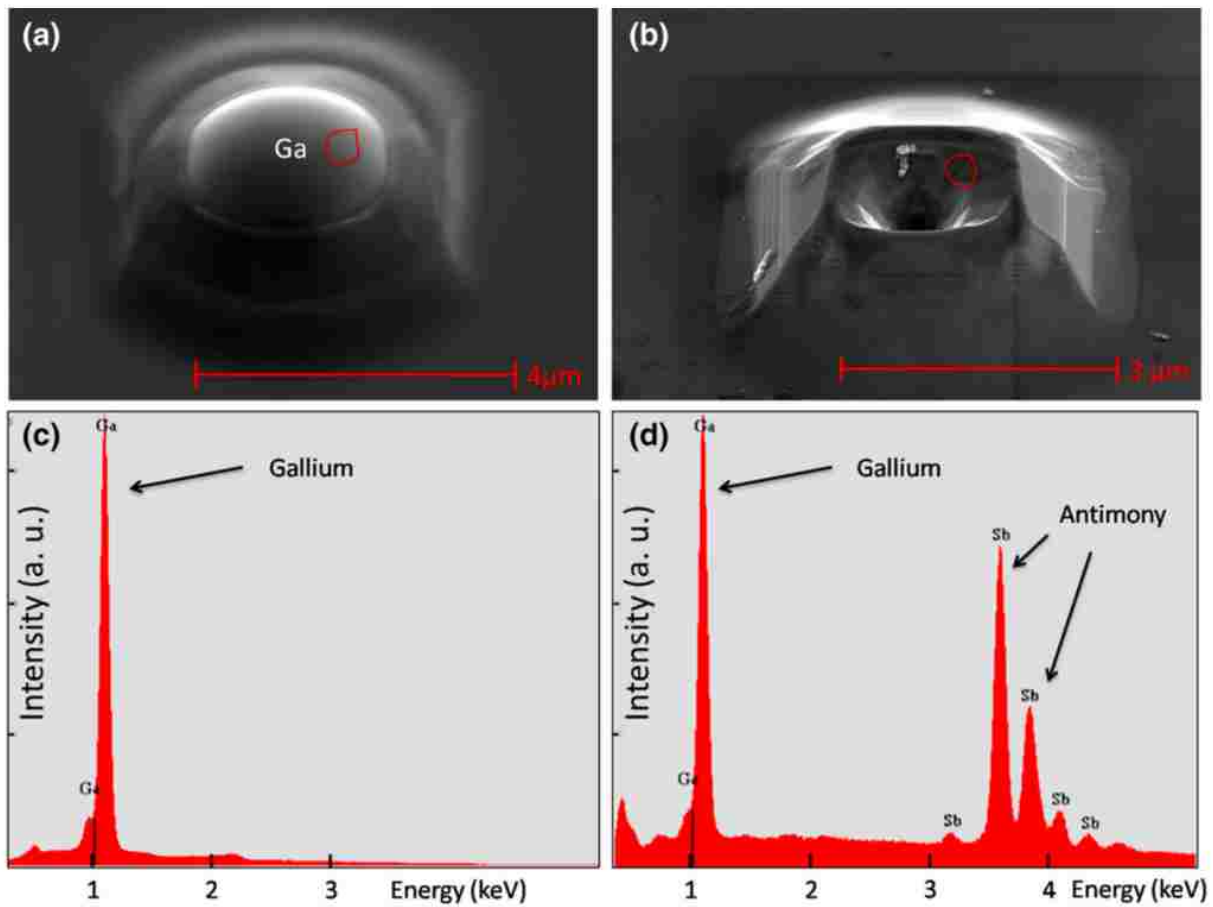
FIG. 2.8 SEM IMAGES OF FACETED DEFECTS WITH THEIR CORRESPONDING EDS SPECTRUM: (A) SEM IMAGE OF OVAL DEFECT, AND (B) HIGHLY-FACETED DEFECT; EDS SPECTRUM OF AREA ENCLOSED BY THE RED LINE (C) ON THE OVAL DEFECT SHOWING A GA PEAK, AND (D) ON THE HIGHLY-FACETED DEFECT SHOWING A GA AND A SB PEAK (FROM [12])

31

The evolution of the Ga droplet to the highly-faceted defect is described by the mechanism shown in Fig 2.9 [12]. First, the Ga droplet falls on the epitaxial surface. Then the Ga droplet becomes a second Ga source for surface epitaxy avoiding any growth on its surface. The growth proceeds around the Ga droplet until the diffusion length of the Ga ad-atoms is less than the droplet depth. This results in a pyramidal shape defect with a void in the center. Such defects are problematic when they form before the PN junction and make it to the surface as metal migration from the top contact into the void will short the devices.
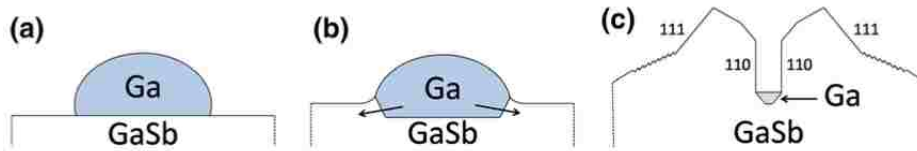
FIG. 2.9 EVOLUTION OF DEFECT DECORATION ON THE EPITAXIAL SURFACE: (A) GALLIUM DROPLET DEPOSITED ON THE EPITAXIAL SURFACE; (B) GALLIUM DROPLET IS A SOURCE FOR SURFACE EPITAXY; (C) HIGHLY-FACETED DECORATION FORMS AROUND THE GALLIUM CORE (FROM [12]).

In the GaSb diodes studied, most surface defects were the highly-faceted defects [12]. Hence, controlling the ejection of Ga droplets is key to achieving GaSb diodes with good electrical properties. The next two subsections describe how the Ga droplet problem and substrate quality were addressed.

2.2.2 Mitigation of Highly-Faceted Defects

The droplets that lead to the detrimental faceted defects in GaSb homoepitaxy come from Ga "spitting" from the Ga crucible. Ga "spitting" is believed to be due to two main reasons [18-20]. The first reason is that in typical single filament effusion cells, the lip of the crucible is cooler than the rest of the cell. Thus, there is condensation of Ga at the mouth of the crucible. Over time these condensates form droplets that fall back into the hot melt and are ejected onto the growth surface. The second reason is that the localized hot spots on the crucible wall cause hot

spots in the Ga melt that generate violent turbulence and ejection of Ga droplets. Therefore, the solution to Ga spitting also lies in the design of the Ga effusion cells.

Conventional Ga sources have a conical crucible that is heated at the base with a single filament. Therefore, the crucible is slightly cooler at the lip and Ga can condense at the crucible's orifice. However, thanks to the advancement in effusion cell technology, controlling the heating of the source from base to tip is now possible. For instance, Veeco ® offers dual filament sources with two independent heaters that control the temperature along the crucible [21]. The dual filament source reduces the oval defect density significantly since a hot-lip can be kept at higher temperatures than the base avoiding condensation of Ga at the crucible orifice [21]. The dual filament design also results in fewer hot-spots and a more uniformly heated crucible.

The diodes in the previous section were grown on a VG V80 MBE reactor equipped with a conventional single filament source for the Ga charge held in a conical crucible. Hence, this growth configuration resulted in the formation of Ga-droplet based defects. To compare the effect of using a single-filament versus a dual-filament source, 2 µm thick GaSb films are grown on different reactors. The V80 MBE reactor has the single-filament Ga source, and the Gen 10 reactor has a SUMO effusion cell with dual-filaments which permits heating of the lip of the crucible and prevents Ga condensation.

(a) V80 Reactor with single-filament source   (b) Gen 10 Reactor with dual-filament source
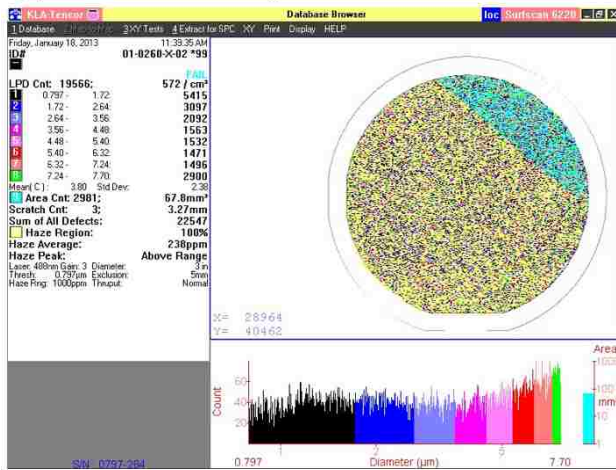
FIG. 2.10 NOMARSKI IMAGES COMPARING SURFACE MORPHOLOGY OF GaSb HOMOEPITAXY GROWN ON (A) THE V80 REACTOR WITH A SINGLE-FILAMENT Ga SOURCE, AND (B) THE GEN 10 REACTOR WITH A SUMO DUAL-FILAMENT Ga SOURCE
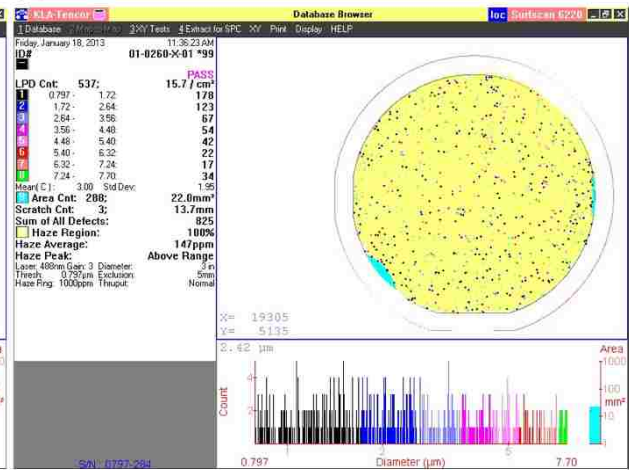
FIG. 2.11 SURFACE SCAN OF SAMPLE GROWN ON ON (A) THE V80 REACTOR WITH A SINGLE-FILAMENT Ga SOURCE, AND (B) THE GEN 10 REACTOR WITH A SUMO DUAL-FILAMENT Ga SOURCE

Fig 2.10 shows Nomarski micrographs of GaSb surface morphology from the samples grown in the different reactors.   Oval defects are still present on both samples. Nonetheless, from surface scan analysis, it can be concluded that the samples from Gen 10 MBE reactor results in less defects. Fig 2.11a shows the surface scan of the sample grown on the V80 reactor with the

34

single-filament source. Fig 2.11b shows the surface scan of the sample grown on the Gen 10 reactor with the dual-filament source. Using the SUMO ® dual-filament source decreases the defect density of GaSb homoeptiaxy by approximately 96 %. Therefore, the single-filament source in the V80 reactor was replaced with a SUMO dual-filament source.

2.2.3 Mitigation of Irregular Defects

The defect density on GaSb homoepitaxy is also dependent on the surface quality of the substrates. Therefore, wafers from two different vendors are tested. Again, 2 μm thick GaSb epitaxial layers are grown on GaSb substrates from the different vendor and to eliminate the oval defect problem; both samples are grown on the Gen 10 MBE reactor with the SUMO dual-filament Ga source that prevents Ga "spitting."

Fig 2.12 shows Nomarski images of the surface morphology. Both samples show oval defects and polishing lines. However, the polishing lines on the sample grown on the GaSb substrate from vendor 1 are not as pronounced as the ones from vendor 2. The other difference is the orange peel surface morphology for samples grown on substrates from vendor 1.
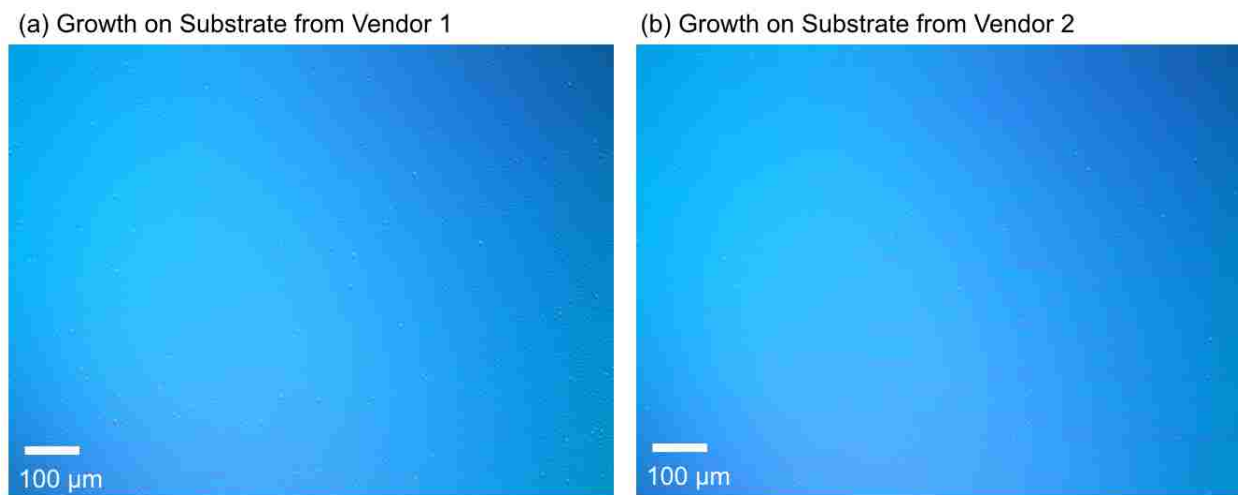
FIG. 2.12 NOMARSKI IMAGES COMPARING SURFACE MORPHOLOGY OF GASb HOMOEPITAXY GROWN ON SUBSTRATES FROM (A) VENDOR 1, AND (B) VENDOR 2

Fig 2.13 shows the surface scan of the samples grown on the different substrates. The defect density of GaSb homoepitaxy on GaSb substrates from vendor 1 is about half of that from vendor 2. However, the diode characteristics of devices grown on GaSb substrates from vendor 2 are better than ones from diodes grown on substrates from vendor 1 as shown in Fig 2.14.
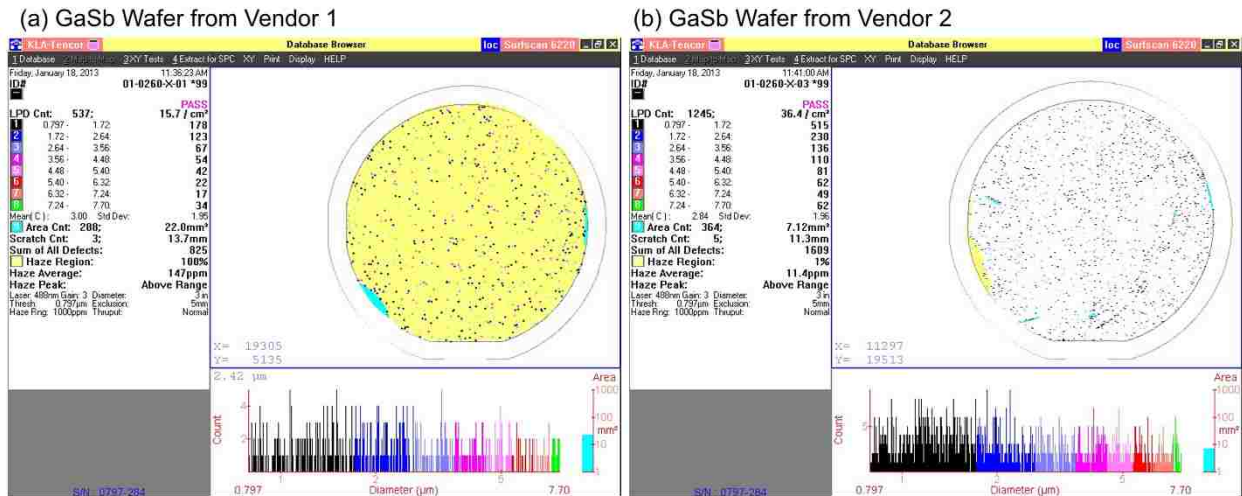
FIG. 2.13 SURFACE SCAN OF SAMPLE GROWN ON GASB SUBSTRATES FROM (A) VENDOR 1 AND (B) VENDOR 2
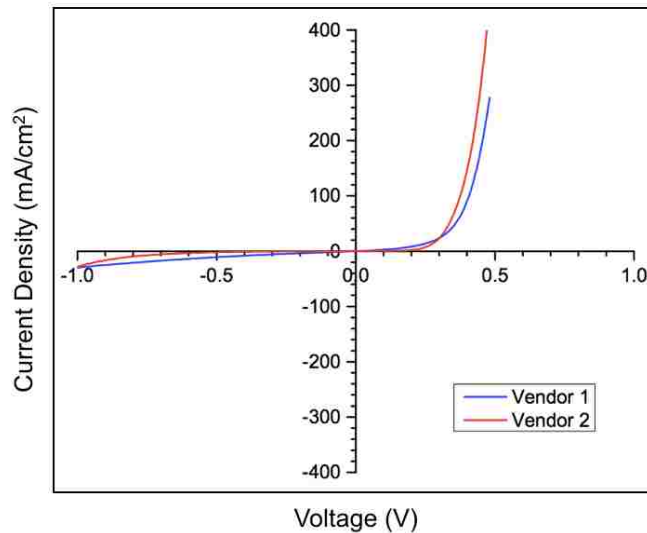
FIG. 2.14 DARK J-V CHARACTERISTICS OF GASB DIODES GROWN ON GASB SUBSTRATES FROM DIFFERENT VENDORS

2.2.4 Design of TPV Cell Mask

Design of top contact grid is a trade-off between resistive losses associated with widely spaced grid and reflection losses caused by surface metal coverage. For GaSb TPV devices, the metal coverage is a concern as some highly-faceted defects may remain. The previous mask design has a 16.83 % metal coverage per cell. The 0.5 cm x 0.5 cm cell has 19 fingers with a width of 25 µm, and a busbar with a width of 300 µm as shown in Fig 2.15a. The highly-faceted defects can have a diameter of up to 5 µm. To minimize the possibility of having metal going into the void of the defects, the metal coverage for the 0.5 cm x 0.5 cm cell has been reduced to 5.67 % by reducing the width of the fingers to 6 µm and the width of the busbar to 55 µm. The new grid design is shown in Fig 2.15b. Table 2.1 compares the element dimensions for the two designs.
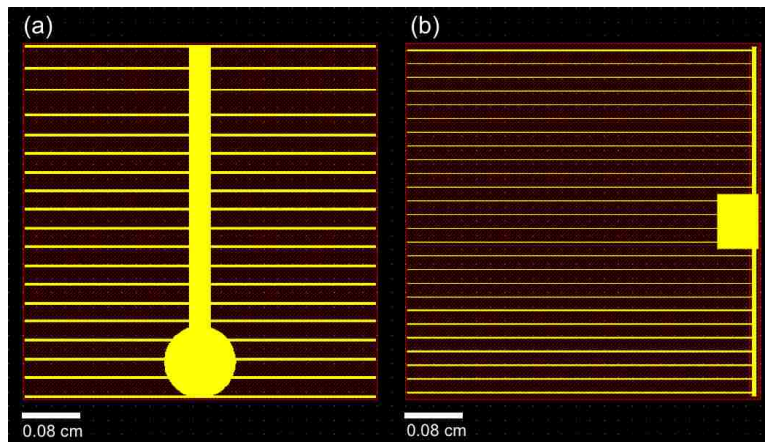
FIG. 2.15 METAL GRID PATTERN (A) PREVIOUS AND (B) NEW DESIGN

TABLE 2.1. Dimensions of the metal grid elements

Design	Fingers per busbar	Finger width (µm)	Busbar width (µm)	Pad Area (µm^2)	Metal Coverage (%)
Previous	19	25	300	785350	16.83
New	26	6	55	423750	5.67

2.2.5 Fabrication of Large Area (1 cm x 1 cm) GaSb TPV Devices

After addressing all the above issues, the GaSb TPV structure in Table 2.1 is grown on GaSb

wafers from vendor 2 in the VG V80 MBE reactor with the new Veeco SUMO dual-filament

source. The native oxide on the GaSb substrates is thermally desorbed at 550 ºC and is verified

by a transformation in the Reflection High Energy Electron Diffraction (RHEED) pattern from a

diffuse scatter showing oxide rings to a distinct 3-D spotty pattern. Oxide desorption is carried

out for ~ 30 min under to ensure the removal of the oxide layer over the entire wafer. Following

oxide desorption, the substrate temperature is brought down to 500 ºC and a 0.20 μm thick n^{++}-

GaSb contact layer is grown followed by a 0.30 μm n^{+}- AlSb back surface field layer (BSF), a

2.50 μm n - GaSb base, a 0.50 μm p - GaSb emitter, a 0.03 μm p^{+}- AlSb window, and a 0.10 μm

p^{++}- GaSb contact layer as summarized in Table 2.2.

TABLE 2.2. GaSb TPV structure

Layer	Material	Thickness (μm)	Doping type & concentration (cm^{-3})
Contact	GaSb	0.10	(p^{++}) 5 x 10^{18}
Window	AlSb	0.03	(p^{+}) 1 x 10^{18}
Emitter	GaSb	0.50	(p) 5 x 10^{17}
Base	GaSb	2.50	(n) 4 x 10^{17}
BSF	AlSb	0.30	(n^{+}) 1 x 10^{18}
Contact	GaSb	0.20	(n^{++}) 5 x 10^{18}
n-type GaSb substrate			

Device fabrication is performed using standard photolithography techniques. Metals are

deposited via e-beam evaporation. For the top grid, p-type 500 Å Ti/ 500 Å Pt/ 3000 Å Au

ohmic contacts are deposited. For the bottom contacts, a metal sequence of 87 Å Ni/ 560 Å Ge/

233 Å Au/ 476 Å Pt/ 3000 Å Au is deposited as a metal blanket on the back of the GaSb

substrate. Prior to each metal deposition, samples are dip in an HCl:H$_2$O 1:3 solution for 60 sec

to remove native oxides from the GaSb surface. To make the n-contacts ohmic, the n-GaSb

contacts are annealed at 290°C for 45 seconds [22]. Finally, the devices are isolated by etching

the mesas below the p-n junction using an inductively coupled plasma reactor with BCl_3 gas. The cells processed have areas of 1 cm x 1 cm and 0.5 cm x 0.5 cm and all revealed good diode characteristics. Fig. 2.16 shows the J-V characteristics of one of the 1 cm x 1 cm GaSb TPV cell along with the theoretical J-V curve of GaSb PV cell with ideal behavior under AM1.5G illumination. The actual GaSb PV cell exhibits an open-circuit voltage (V_{OC}) of 0.28 V, a short-circuit current density (J_{SC}) of 28 mA/cm^2, a fill factor (FF) of 52%, and an efficiency (η) of 4%. On the other hand, an ideal GaSb PV cell is expected to reach a J_{SC} of 59.5 mA/cm^2, a V_{OC} of 0.40 V, a FF of 78%, and an efficiency of 18.5 %. This ideal behavior assumes that the quantum efficiency of the cell is 100% for all photon energies greater than the bandgap. To achieve a J_{SC} close to 59.5 mA/cm^2, the actual cell will need an antireflective coating. The lower FF and V_{OC} of the actual cell in comparison to the ideal cell is due to the remaining defects in the crystal which provide an alternate current path for photogenerated carriers reducing the voltage from the cell.
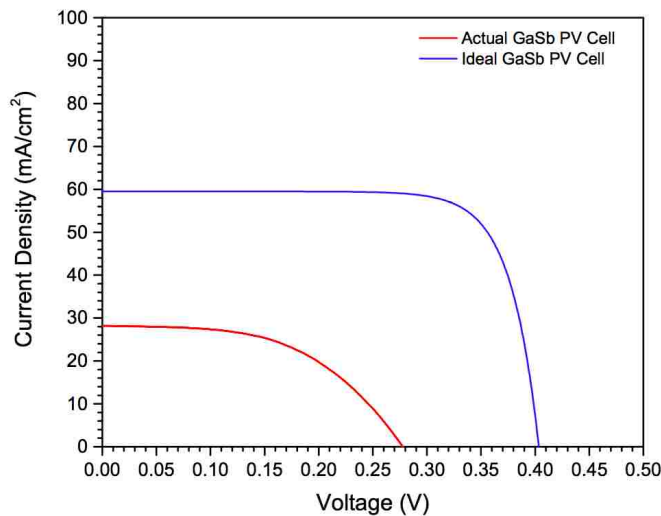
FIG. 2.16 J-V CHARACTERISTICS OF LARGE AREA (1CM^2) GASB TPV UNDER ONE SUN ILLUMINATION

2.3 Isolation of GaSb Membranes from GaSb Substrates

The isolation of narrow-gap antimonide semiconductor layers from GaSb substrates has been of significant interest for infrared detectors and thermophotovoltaics among other optoelectronic devices [23-26]. In the case of infrared focal-plane array (FPA) detectors, removal of the GaSb substrates is crucial since GaSb has a high optical absorption coefficient and a large thermal mismatch in comparison with the Si-based readout integrated circuit [23-25]. In thermophotovoltaics, the monolithic interconnection of TPV devices is often desired to build up the open circuit voltage and reduce parasitic losses [26]. In this thesis, the reason to remove the GaSb substrate is to eliminate its thermal resistance and improve the thermal management of TPV cells.

Although possible, the isolation of III-Sb epitaxial layers from GaSb substrates is rather difficult due to the lack of highly selective etchants in the InAs/AlSb/GaSb material system [27]. In this section, two techniques are described; substrate removal technique which has been used mostly in FPA detectors, and epitaxial lift off technique which has been only used in AlAs/GaAs systems.

2.3.1 Substrate Removal of GaSb

Selective etching within the InAs/AlSb/GaSb material system has been studied by several groups to isolate individual devices on a wafer, or to remove excess substrate material. Weak bases such as Microposit MF319 (a positive photoresist developer) and diluted ammonium hydroxide can selectively etch antimonides over InAs [28-30]. These etchants had been used for shallow etches, where antimonide epitaxial layers need to be removed to reach InAs. Dier $et\ al$. studied three solutions; A citric acid based ($C_6H_8O_7$:H_2O:H_2O_2), a KNa-tartaic acid based

($C_4H_4KNaO_6$:H_2O:HCl:H_2O_2) and hydrochloric acid based solution (HCl:H2O2:H2O) [27]. The citric acid base solution has the maximum selectivity. Citric acid can etch InAs 110.66 times faster than GaSb. The other two etchants do not have viable selectivity. For GaSb over InAsSb, the tartaric acid solution has a selectivity of 16.43, and the hydrochloric acid solution has a selectivity of 5.49. The selectivity of InAs/AlSb/GaSb material systems is extremely low, hence it is difficult to stop the etch precisely at the desired layer.

For the removal of GaSb substrates, a CrO_3:HF:H_2O solution has been used [23, 26]. Although CrO3:HF:H2O is considered to be a selective etchant for GaSb, there is no report of how selective it is. However, its selectivity must be low since it gives a non-uniform etch that causes the disappearance of the etch stop layer in some parts of the sample before the substrate is entirely removed [23]. To minimize this uniformity problem, GaSb substrates are thinned down to at least 50 μm by a combination of mechanical lapping and chemical-mechanical polishing prior to the CrO_3:HF:H_2O etch [23, 26].

Since anything that etches GaSb etches AlSb, the etch stop layer must be InAs based. $InAs_{0.91}Sb_{0.09}$ is lattice matched to GaSb, and consequently a thick etch stop layer can be grown [25]. Since InAs0.91Sb0.09 is slightly etched by CrO3:HF:H2O, the thickness of the etch stop layer is required to be in the micron range. After substrate removal, the $InAs_{0.91}Sb_{0.09}$ etch stop layer can be removed with $C_6H_8O_7$:H_2O:H_2O_2 [24].

For this thesis, it was decided not to try this substrate removal technique due to the safety and hazards related to CrO_3. In addition, the lack of high selectivity in the InAs/AlSb/GaSb material system has proven to be a rather difficult problem to overcome. Thus alternative approaches have to be explored.

2.3.2 Epitaxial Lift Off from GaSb Substrates

Epitaxial lift-off (ELO) has been an effective technique for the separation of GaAs based devices from GaAs substrates. Hydrofluoric acid (HF) is used to selectively etch an AlGaAs sacrificial layer that is inserted between the epitaxial layers and the GaAs substrate. The GaAs epitaxial layers can be released from the GaAs substrate without damage because HF has an extremely high selectivity for AlGaAs ($\geq 10^7$) [31]. The selectivity of wet etchant solutions for antimonide-based compound semiconductors is only in the hundreds which hinders the possibility of ELO for InAs/AlSb/GaSb material systems.

Nonetheless, Fastenau *et al*. reported a high etching selectivity between AlSb and InAs in aqueous HF [32]. Fastenau *et al*. demonstrated the ELO of InAs and GaSb/InAs layers from GaAs substrates by etching away a 1 µm thick AlSb sacrificial layer with diluted HF [32]. The GaSb/InAs samples had to be encapsulated with black wax to prevent GaSb from etching away. As mention before, anything that etches AlSb, etches GaSb and so GaSb is etched by HF.

To try Fastenau *et al*.'s approach of releasing GaSb epitaxial layers by ELO, the structure in Fig. 2.17 is grown. InAs layers are grown before and after the AlSb sacrificial layer to protect the GaSb epitaxial layer and the GaSb substrate from HF. The samples are cleaved into 1 cm x 1 cm squares and their surface is covered with black wax. Then the samples are submerged in HF:H_2O 1:20 solution. However, the GaSb/InAs films did not release from the GaSb substrate. The samples were in HF for months and no sign of ELO was observed. At this point, the idea of releasing GaSb films from GaSb substrates was abandoned. Instead, a GaSb/AlGaAs/GaAs metamorphic structure was explored as will be described in chapter 3.

FIG. 2.17 SCHEMATIC OF ELO STRUCTURE FOR INA/ALSB/GASB MATERIAL SYSTEMS

During ELO of metamorphic GaSb TPV from GaAs substrates (described in chapter 3), the results provided an alternative technique for the ELO of GaSb epitaxial layer from GaSb substrates. The metamorphic GaSb TPV cell had 300 nm AlSb back surface reflector layer and a 30 nm AlSb window layer as shown by the schematic in Fig 2.18a. After leaving the sample in HF:H_2O 1:20 for 10 hours, three pieces resulted as shown in Fig 2.18c. The initial theory (later invalidated by EDS) was that the 300 nm AlSb layer etched along with the AlGaAs sacrificial layer and that the extra piece was the 200 nm GaSb layer above the 300 nm AlSb layer. This meant that GaSb epitaxial layers could be released from GaSb substrates.

FIG. 2.18 SCHEMATIC SPECULATING WHAT HAPPENED DURING ELO PROCESS OF A METAMORPHIC GASB TPV CELL, (A) LATERAL ETCH OF ALSB AND ALGAAS, (B) AND (C) RESULTS AFTER ELO.

Hence, a 3 µm thick GaSb layer is grown on a GaSb substrate with a 300 nm AlSb sacrificial layer. The samples are cleaved in squares of 0.5 cm x 0.5 cm (instead of 1 cm x 1 cm). This time, ELO of GaSb from GaSb was somewhat successful as shown in Fig 2.19. Small area GaSb layers can be lifted off from GaSb substrates if the GaSb layers are protected with an InAs layer and the AlSb sacrificial layer is thick.

The released GaSb film is analyzed by SEM and EDS. Fig 2.20a shows an SEM image of the sample that encloses part of the GaSb film and part of the oxidized edge that appears in Fig 2.19. The GaSb film, zone 001 in the SEM image, is indeed GaSb as shown by strong Ga and Sb peaks in the EDS spectrum in Fig 2.20b. Fig 2.2c has the EDS spectra for zone 002 which shows the presence of Au, Ge, Ni and some Sb. The GaSb on the edges of the sample is etched away and only the n-contact metals are left bonded to the black wax. The surface of the samples is metallized with Ni/Ge/Au/Pt/Au prior to ELO because a metal surface prevents fracturing of the ELO film and gives some support as will be explained in the following chapters.
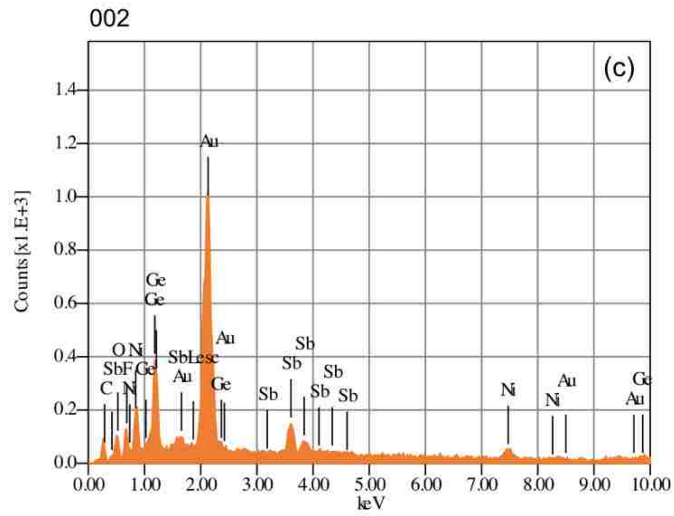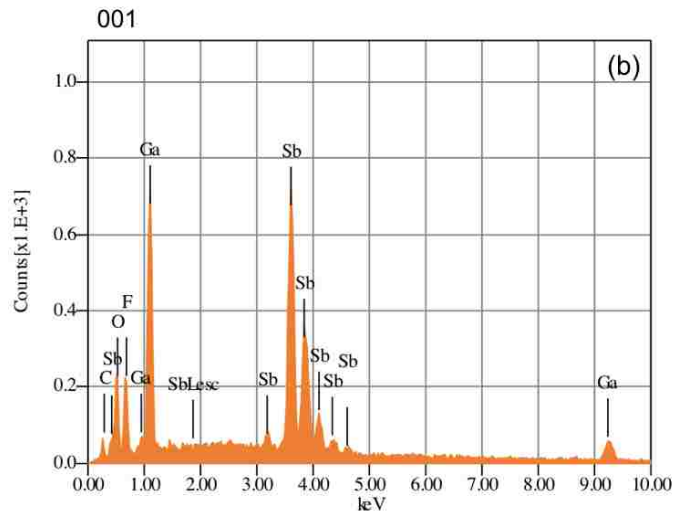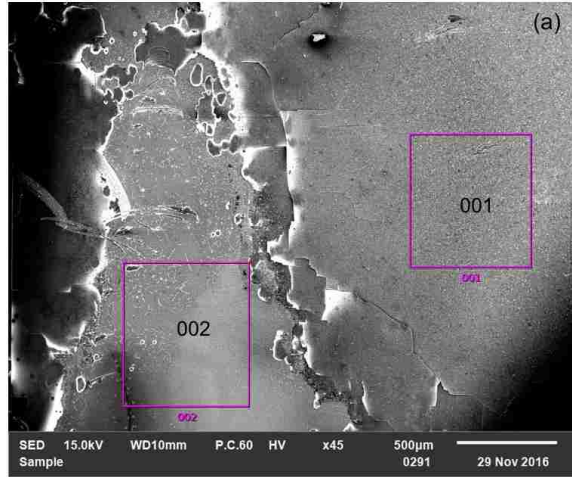
FIG. 2.20 SEM IMAGES AND EDS ANALYSIS OF ELO GaSb FILMS. (A) SEM IMAGE SHOWING THE TWO ZONES WHERE EDS ANALYSIS WAS DONE. EDS SPECTRUM FOR (B) ZONE 001, AND (C) ZONE 002.

2.4 Conclusion

The fabrication of large area (1 cm x 1 cm) GaSb TPV cells with good diode behavior were achieved after addressing the problems with growth defects. Then, the possibility of the lifting of GaSb epitaxial layers from GaSb substrates was demonstrated despite the lack of high selectivity in the InAs/AlSb/GaSb material system. Nonetheless, much work needs to be done to achieve larger ELO GaSb films without etching the edges.

References:

1. Fraas, Lewis M., Han X. Huang, Shi-Zhong Ye, She Hui, James Avery, and Russell Ballantyne. "Low cost high power GaSb photovoltaic cells." In *AIP Conference Proceedings*, vol. 401, no. 1, pp. 33-40. AIP, 1997.

2. Zierak, M., J. M. Borrego, I. Bhat, R. J. Gutmann, and G. Charache. "Modeling of InGaSb thermophotovoltaic cells and materials." In *AIP Conference Proceedings*, vol. 401, no. 1, pp. 55-64. AIP, 1997.

3. Fraas, L. M., G. R. Girard, J. E. Avery, B. A. Arau, V. S. Sundaram, A. G. Thompson, and J. M. Gee. "GaSb booster cells for over 30% efficient solar-cell stacks." *Journal of applied physics* 66, no. 8 (1989): 3866-3870.

4. L. M. Fraas, R. Ballantyne, S. Hui, SZ. Ye, S. Gregory, J. Keyes, J. Avery, D. Lamson, and B. Daniels, "Commercial GaSb cell and circuit development for the midnight sun® TPV stove," In 4th NREL conference on thermophotovoltaic generation of electricity, 1999, p. 480.

5. L. M. Fraas, J. E. Avery, and H. X. Huang, "Thermophotovoltaic furnace–generator for the home using low bandgap GaSb cells," Semiconductor Science and Ttechnology, vol. 18, p. S247, 2003.

6. S. A. Abdallah, D. J. Herrera, B. P. Conlon, N. Rahimi, and L. F. Lester, "Emitter thickness optimization for GaSb thermophotovoltaic cells grown by molecular beam epitaxy," In SPIE Optics+ Photonics for Sustainable Energy, 2015, p. 95620L.

7. Wang, C. A. "Antimony-Based III–V Thermophotovoltaic Materials and Devices." In *AIP Conference Proceedings*, vol. 738, no. 1, pp. 255-266. AIP, 2004.

8. Wang, C. A., H. K. Choi, G. W. Turner, D. L. Spears, M. J. Manfra, and G. W. Charache. "Lattice-matched epitaxial GaInAsSb/GaSb thermophotovoltaic devices." In *AIP Conference Proceedings*, vol. 401, no. 1, pp. 75-87. AIP, 1997.

9. D. Martín, and C. Algora, "Theoretical comparison between diffused and epitaxial GaSb TPV cells," In 6th Conference on Thermophotovoltaic Generation of Electricity, 2004, p 311

10. L. Tang, L. M. Fraas, Z. Liu, C. Xu, X. Chen, "Performance Improvement of the GaSb Thermophotovoltaic Cells With n- Type Emitters," IEEE Transactions on Electron Devices, vol. 62 pp. 2809-15, 2015.

11. Rahimi, Nassim, Daniel J. Henera, Shaimaa Abdallah, Veronika Stelmakh, Walker R. Chan, Ivan Celanovic, and Luke F. Lester. "Epitaxial and non-epitaxial large area GaSb-based thermophotovoltaic (TPV) cells." In *Photovoltaic Specialist Conference (PVSC), 2015 IEEE 42nd*, pp. 1-3. IEEE, 2015.

12. Romero, O. S., A. A. Aragon, N. Rahimi, D. Shima, S. Addamane, T. J. Rotter, S. D. Mukherjee, L. R. Dawson, L. F. Lester, and G. Balakrishnan. "Transmission electron microscopy-based analysis of electrically conductive surface defects in large area GaSb homoepitaxial diodes grown using molecular beam epitaxy." *Journal of electronic materials* 43, no. 4 (2014): 926.

13. Rahimi, N., D. J. Herrera, A. Aragon, D. M. Shima, O. S. Romero, T. J. Rotter, T. Busani, O. Lavrova, G. Balakrishnan, and L. F. Lester. "GaSb thermophotovoltaics: current challenges and solutions." In *SPIE OPTO*, pp. 935816-935816. International Society for Optics and Photonics, 2015.

14. Rahimi, Nassim. *Design, fabrication and characterization of epitaxial and non-epitaxial thermophotovoltaic cells*. The University of New Mexico, 2014.

15. Nosho, B. Z., B. R. Bennett, E. H. Aifer, and M. Goldenberg. "Surface morphology of homoepitaxial GaSb films grown on flat and vicinal substrates." *Journal of crystal growth* 236, no. 1 (2002): 155-164.

16. Murray, Lee M., Asli Yildirim, Sydney R. Provence, Dennis T. Norton, Thomas F. Boggess, and John P. Prineas. "Causes and elimination of pyramidal defects in GaSb-based epitaxial layers." *Journal of Vacuum Science & Technology B, Nanotechnology and Microelectronics: Materials, Processing, Measurement, and Phenomena* 31, no. 3 (2013): 03C108.

17. Haugan, H. J., L. Grazulis, G. J. Brown, K. Mahalingam, and D. H. Tomich. "Exploring optimum growth for high quality InAs/GaSb type-II superlattices." *Journal of Crystal Growth* 261, no. 4 (2004): 471-478.

18. Wood, C. E. C., L. Rathbun, H. Ohno, and D. DeSimone. "On the origin and elimination of macroscopic defects in MBE films." *Journal of Crystal Growth* 51, no. 2 (1981): 299-303.

19. Chai, Young G., and Robert Chow. "Source and elimination of oval defects on GaAs films grown by molecular beam epitaxy." *Applied Physics Letters* 38, no. 10 (1981): 796-798.

20. Tsang, W. T. "Elimination of oval defects in epilayers by using chemical beam epitaxy." *Applied Physics Letters* 46, no. 11 (1985): 1086-1088.

21. http://www.veeco.com/products/dual-filament-source-1

22. Rahimi, Nassim, Andrew A. Aragon, Orlando S. Romero, Darryl M. Shima, Thomas J. Rotter, Sayan D. Mukherjee, Ganesh Balakrishnan, and Luke F. Lester. "Electrical and microstructure analysis of nickel-based low-resistance ohmic contacts to n-GaSb." *APL Materials* 1, no. 6 (2013): 062105.

23. Delaunay, Pierre-Yves, Binh Minh Nguyen, Darin Hofman, and Manijeh Razeghi. "Substrate removal for high quantum efficiency back side illuminated type-II In As∕Ga Sb photodetectors." *Applied Physics Letters* 91, no. 23 (2007): 231106.

24. Rehm, Robert, Martin Walther, Johannes Schmitz, Matthias Wauro, Wolfgang Luppold, Jasmin Niemasz, Frank Rutz, et al. "Substrate removal of dual-colour InAs/GaSb superlattice focal plane arrays." *physica status solidi (c)* 9, no. 2 (2012): 318-321.

25. Klein, B., J. Montoya, N. Gautam, and S. Krishna. "Selective InAs/GaSb strained layer superlattice etch stop layers for GaSb substrate removal." *Applied Physics A* 111, no. 2 (2013): 671-674.

26. Wang, C. A., R. K. Huang, D. A. Shiau, M. K. Connors, P. G. Murphy, P. W. O'Brien, A. C. Anderson, D. M. DePoy, G. Nichols, and M. N. Palmisiano. "Monolithically series-interconnected GaInAsSb/AlGaAsSb/GaSb thermophotovoltaic devices with an internal backsurface reflector formed by wafer bonding." *Applied physics letters* 83, no. 7 (2003): 1286-1288.

27. Dier, Oliver, Chun Lin, Markus Grau, and Markus-Christian Amann. "Selective and non-selective wet-chemical etchants for GaSb-based materials." *Semiconductor science and technology* 19, no. 11 (2004): 1250.

28. Yoh, Kanji, Kazumasa Kiyomi, Akira Nishida, and Masataka Inoue. "Indium arsenide quantum wires fabricated by electron beam lithography and wet-chemical etching." *Japanese journal of applied physics* 31, no. 12S (1992): 4515.

29. Gatzke, C., S. J. Webb, K. Fobelets, and R. A. Stradling. "In situ Raman spectroscopy of the selective etching of antimonides in GaSb/AlSb/InAs heterostructures." *Semiconductor science and technology* 13, no. 4 (1998): 399.

30. Su, Ning, Yong Tang, Ze Zhang, T. F. Kuech, and P. Fay. "Observation and control of electrochemical etching effects in the fabrication of In As∕ Al Sb∕ Ga Sb heterostructure devices." *Journal of Vacuum Science & Technology B: Microelectronics and Nanometer Structures Processing, Measurement, and Phenomena* 26, no. 3 (2008): 1025-1029.

31. Yablonovitch, Eli, T. Gmitter, J. P. Harbison, and R. Bhat. "Extreme selectivity in the lift-off of epitaxial GaAs films." *Applied Physics Letters* 51, no. 26 (1987): 2222-2224.

32. Fastenau, Joel, Gary Tuttle, and Fran Laabs. "Epitaxial lift-off of thin InAs layers." *Journal of electronic materials* 24, no. 6 (1995): 757-760.

Chapter 3: Metamorphic GaSb Thin Film Devices Grown on GaAs Substrates

3.1 Introduction

As mentioned in the previous chapter, the isolation of III-Sb epitaxial layers from GaSb

substrates is a difficult process due to the lack of favorable wet etchant chemistry for

InAs/GaSb/AlSb based materials [1]. In contrast to antimonide compounds, arsenides have a

very favorable and well understood etch technology. GaAs substrates can be removed with a

variety of highly selective etchants using an AlAs or a high aluminium content AlGaAs etch stop

layer [2-5]. Furthermore, the extremely high selectivity of hydrofluoric acid towards AlAs over

GaAs provides an opportunity for lateral etching and subsequently epitaxial lift off [6-7].

Therefore, an alternative method for realizing thin GaSb based membranes would be to grow

GaSb devices on GaAs substrates and take advantage of the GaAs/AlGaAs etch chemistry. The

problem in growing GaSb on GaAs substrates is the 7.78% mismatch between the GaSb and the

GaAs layers which results in a significant amount of stress and subsequently in dislocations in

the GaSb epitaxial layer.

The ability to grow GaSb on GaAs is of significant benefit to more applications than just

photovoltaics. GaAs substrates are an attractive alternative to GaSb substrates because of their

semi-insulating nature, lower optical absorption coefficient, relatively lower cost, and ability to

scale up to large wafer sizes [8-10]. Hence, to take advantage of these benefits, a great deal of

effort has been expended to minimize the propagation of threading dislocations [11-13]. Two of

the main techniques to achieve this are compositionally graded metamorphic buffers and the

induction of 90 ° interfacial misfit (IMF) dislocations arrays [12-13].

During epitaxial crystal growth, epitaxial materials are deposited with atomic registry on the surface of an existing crystalline templated called substrate [14]. When the lattice mismatch between the substrate and the epitaxial layer is more than ~ 0.1%, the strain energy quickly builds up and starts to form defects in the epitaxial layer. The deleterious effects of defect formation have been circumvented for some applications by the development of metamorphic buffers which create defects to alleviate strain, and then filter the defects via lateral propagation at the material interface. Several researchers of whom the prominent ones are Matthews-Blakslee [15] and People-Bean [16] have modeled the mechanisms involved in these growths. Both groups of researchers consider bulk phenomena including the concept of critical thickness to explain the presence of defects in mismatched materials.

However, the mismatch between certain semiconductors can be overcome using specific atomic arrangements that are based on the 2D packing of larger atoms on smaller surfaces thus inducing a single layer of planar misfit dislocations to accommodate the strain. One such material system where interfacial misfit dislocations have resulted in extremely high quality epitaxy is the GaSb growth on GaAs [12-13]. It has been identified that the (2 x 8) Sb reconstruction on Sb-terminated GaAs, in particular, possesses the unique ability to pack two-dimensionally on the GaAs substrate and in the process forms an array of 90° misfit dislocations. These dislocations allow Sb atoms on GaAs to take on the lattice constant of GaSb and thus circumvent the restrictions imposed by strain and critical thicknesses. The IMF growth mode is a key enabler for the separation of GaSb films from GaAs. This is because unlike the metamorphic growth mode where there is a significant compressive strain in the buffer, the IMF growth mode is a fully relaxed structure with the change in lattice constant occurring in one atomic layer. Thus, making it an ideal growth mode for substrate removal and ELO.

In the following paragraphs, the growth of GaSb epitaxial layers on GaAs substrates by IMF technique is explained in detail. Following that, the isolation of GaSb membranes from GaAs substrates is demonstrated. Finally, the process to integrate the thin film GaSb TPV devices to CVD diamond heat spreaders is described, and the resulting electrical characteristics of the thin film devices are presented.

3.2 Growth of GaSb on GaAs

The IMF growth mode allows for the realization of GaSb epitaxial layers with 100% relaxation and reduced threading dislocations density (TDD) by inducing arrays of 90º interfacial misfit dislocations at the GaSb/GaAs interface [13]. The strain produced by the 7.78% lattice mismatch is relieved by misfit and threading dislocations [11]. The threading dislocations in the GaSb epitaxial layer are typically associated with 60 º misfit dislocations [11]. Hence, if the nucleation of 60 º misfit dislocations can be reduced, the detrimental threading dislocations propagating to the epitaxial layer can be eliminated. The formation of 90º rather than 60º misfit dislocations can be controlled by the growth conditions [13].

A highly periodic array of 90º misfit dislocations at the GaSb/GaAs interface, as shown in the cross-sectional transmission electron microscopy (XTEM) image in Fig 3.1, can be obtained by the following growth sequence. First, the native oxide of the GaAs substrate is desorbed at 620º C. Then the substrate is cool down to 580°C to deposit a 100 nm GaAs buffer layer to assure a smooth starting surface. After completion of the homoepitaxy, the Ga shutter and As valves are closed allowing the As surface layer to desorb. When the reflection high electron energy diffraction (RHEED) transitions from an As rich (2 x 4) to a Ga-rich (4 x 2) surface, the Sb source is opened so that Sb can replace the desorbed As. Subsequently, the substrate

temperature is reduced to 510 ° C under Sb overpressure. During this time, the RHEED pattern changes to a (2 x 8) which indicates a Sb-terminated surface. The achievement of a the (2 x 8) Sb reconstruction has been identified as key for the formation of the periodic array of 90° misfit dislocations [18]. The growth of GaSb is then initiated as soon as 510°C is reached.
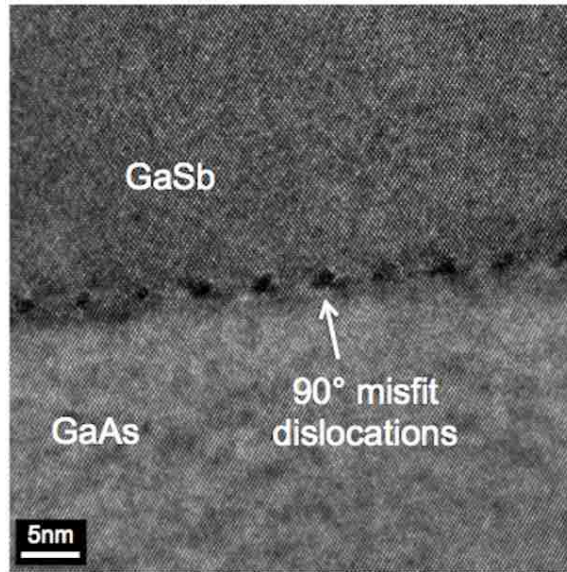
FIG. 3.1 XTEM IMAGES OF THE GASB/GAAS INTERFACE.

3.3 Isolation of GaSb membranes from GaAs substrates

To demonstrate the isolation of GaSb membranes from GaAs substrates, the structures shown in Fig 3.2 are grown. Structure A is grown with a 100 nm $Al_{0.85}Ga_{0.15}As$ etch stop layer (or sacrificial layer) on GaAs substrate followed by a 100 nm layer of GaAs on which a 3 μm thick GaSb epitaxial layer is grown. In structure B, the thin GaAs epitaxial layer was left out, and GaSb was directly grown on the AlGaAs etch stop layer. In structure C, GaSb was directly grown on GaAs without an etch stop layer. The purpose of structure A is to explore the possibility of using well established GaAs substrate removal techniques to isolate the GaSb/GaAs epitaxial layers. The purpose of structure B is to see if the 90° misfit dislocations array would form at GaSb/AlGaAs interface and to establish its effect on the etch process.

53

Structure C is grown without an etch stop layer to investigate the etch contrast between GaSb and GaAs.
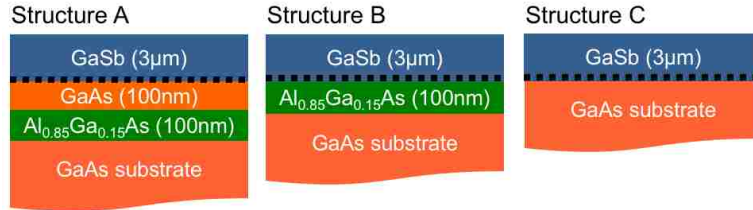
FIG 3.2. SCHEMATIC OF EPITAXIAL STRUCTURES GROWN FOR THE ETCH STUDY

The epitaxial structures are analyzed with cross-section transmission electron microscopy (XTEM), and high-resolution X-Ray diffraction (HR-XRD). The ω - 2θ (004) HR-XRD spectra of structures A, B, and C are shown in Fig 3.3. The diffraction spectra show two distinct peaks without a pseudomorphic growth region, further showing that GaSb epi-layers grown by inducing IMF arrays are spontaneously relaxed from the interface on. The GaSb epitaxial layers of all structures are 100% relaxed according to strain calculations done by analysis of symmetric (004) and asymmetric (115) XRD spectra.
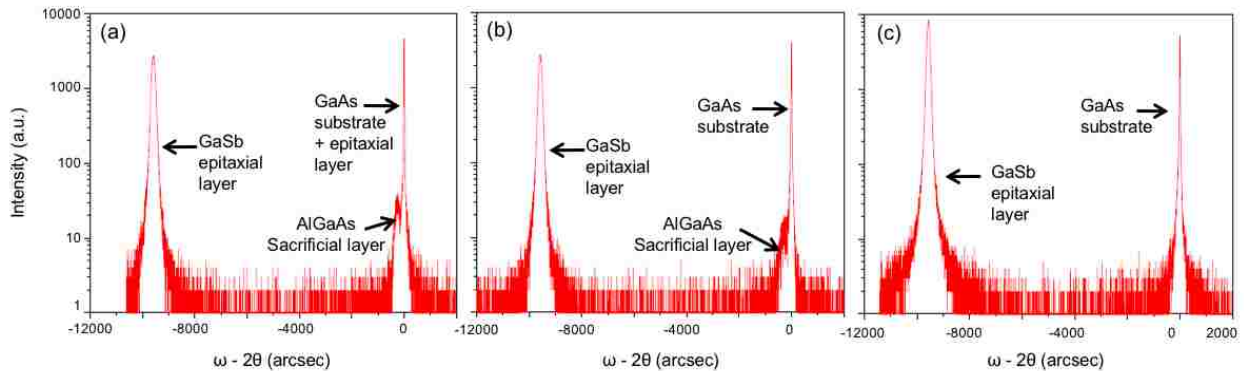
FIG 3.3. Ω - 2Θ (004) X-RAY DIFFRACTION SPECTRA OF (A) STRUCTURE A, (B) STRUCTURE B, AND (C) STRUCTURE C

Fig 3.4 and 3.5 show XTEM images and the SAED patterns of structure A and B, respectively. The epitaxial layers of the structures are distinctly shown by the low resolution XTEM images in Fig 3.4a and 3.5a. Fig 3.4b shows a higher resolution XTEM image of structure A that focuses on the GaSb/GaAs interface where the formation of 90° misfit dislocations is distinguished by the dark spots at the interface. The SAED double spot pattern, on Fig 3.4c, clearly shows the presence of two distinct lattice constants and no pseudomorphic region, indicating that there is spontaneous and complete relaxation of the GaSb epi-layer. Figure 3.5b shows a high resolution XTEM image of structure B focusing on the GaSb/AlGaAs interface, again exposing the dark spots where the IMF array forms. Figure 3.5c shows the GaSb/AlGaAs interface SAED pattern. The highly resolved diffraction spots in the SAED pattern, again, demonstrate two different lattice constants and no pseudomorphic region, indicating that the GaSb epitaxial layer grown on the AlGaAs is spontaneously relaxed.
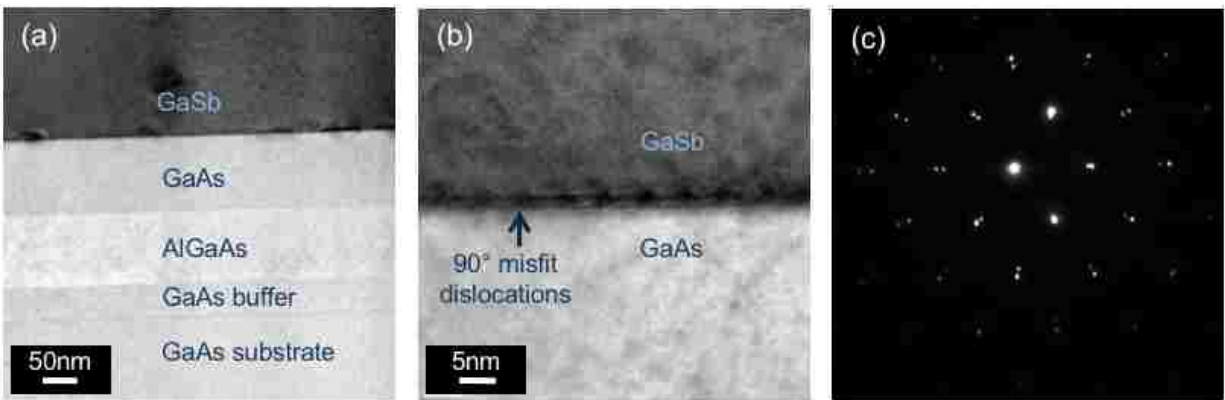
FIG. 3.4 TRANSMISSION ELECTRON MICROSCOPY (TEM) IMAGES AND THE SELECTED AREA ELECTRON DIFFRACTION (SAED) PATTERN OF STRUCTURE A. A) LOW RESOLUTION TEM OF STRUCTURE A EPI-LAYERS. B) HIGH RESOLUTION TEM IMAGE OF THE GASB/GAAS INTERFACE. C) SAED PATTERN OF THE OF THE GASB/GAAS INTERFACE.
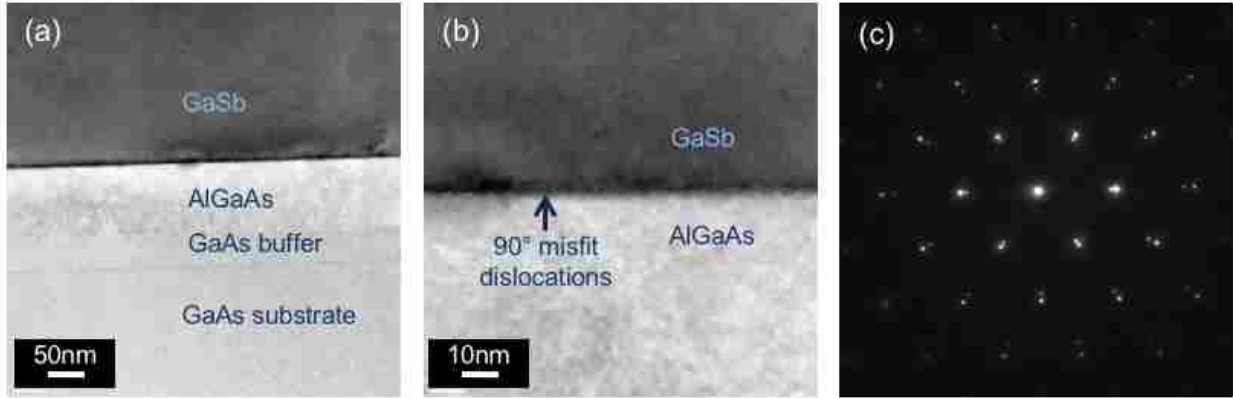
FIG. 3.5 TRANSMISSION ELECTRON MICROSCOPY (TEM) IMAGES AND THE SELECTED AREA ELECTRON DIFFRACTION (SAED) PATTERN OF STRUCTURE B. A) LOW RESOLUTION TEM OF STRUCTURE A EPI-LAYERS. B) TEM IMAGE OF THE GASB/ALGAAS INTERFACE. C) SAED PATTERN OF THE OF THE GASB/ALGAAS INTERFACE.

Fig 3.6 shows XTEM micrographs of structure A and B that includes the 3 μm GaSb layer. As can be seen in the images, some threading dislocations are observed. The average threading dislocation density (TDD) was calculated by adding the lengths of the dislocations on the XTEM image and dividing by the volume of the GaSb layer. The TDD for the GaSb epi-layer grown on the GaAs epi-layer was calculated to be 2.8 x 10^8 defects per cm^2 and 1.5 x 10^8 defects per cm^2 for the GaSb grown on the AlGaAs epi-layer.
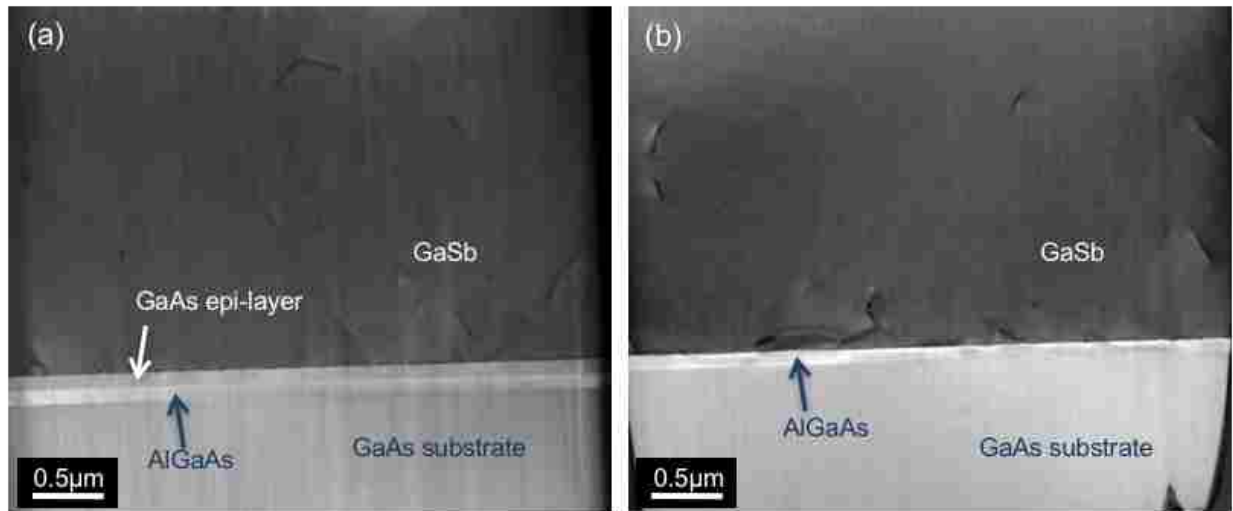
FIG. 3.6 TRANSMISSION ELECTRON MICROSCOPY (TEM) IMAGES. (A) LOW RESOLUTION TEM OF STRUCTURE A. (B) LOW RESOLUTION TEM OF STRUCTURE B.

56

3.3.1 Substrate Removal of GaAs

The most common etchants for GaAs substrate removal are ammonium hydroxide and hydrogen peroxide ($NH_4OH:H_2O_2$), and citric acid and hydrogen peroxide ($C_6H_8O_7:H_2O_2$) solutions [17]. Subsequently, the AlAs or AlGaAs etch stop layer can be removed using hydrofluoric acid (HF) [7], which results in the complete isolation of the epitaxial layer. For this experiment, $NH_4OH:H_2O_2$ solution is selected as the selective etchant for GaAs [5].

The samples used for this study are cleaved into squares of 1 cm x 1 cm for easy handling. The samples are chemically cleaned to remove any impurities by rinsing them with acetone, isopropanol, methanol, and deionized (DI) water and then dried with nitrogen. The samples are then bonded to a glass slide with crystalbond^{TM} 509 adhesive on a hot plate at a temperature of 120°C. Each sample is placed on the glass with the epitaxial layer side down. Slight pressure is applied to the sample to avoid accumulation of air between the wax and the epitaxial layer. Once the sample cools down, the etch process can start.
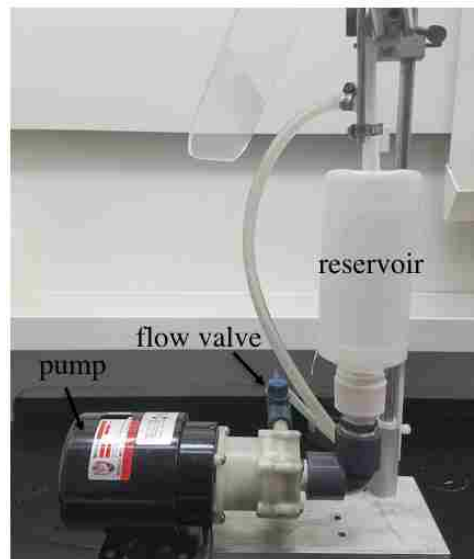
FIG. 3.7 SCHEMATIC OF THE JET ETCHER

The etches are performed with a homemade jet etcher as shown in Fig 3.7. The jet etcher has a 600 ml open vertical reservoir that is connected to a 0.025 horsepower March® pump BC-2CP-

MD that recirculates the etchant solution back into the reservoir. The sample is placed into a sample holder that is suspended about 3cm deep into the opening of the reservoir and approximately 1cm from the jet tip. The stream flow falls directly on the sample and is controlled by a flow valve to achieve a laminar flow across the surface of the sample.

All etching experiments are performed at room temperature. Prior to etch GaAs, a fresh $NH_4OH:H_2O_2$ solution at a volume ratio of 1:33 is prepared [5]. Once the sample is placed in the sample holder, the $NH_4OH:H_2O_2$ solution is poured into the jet etcher reservoir. Then, the pump is turned on, and the valve open until a steady flow covers the surface of the sample.
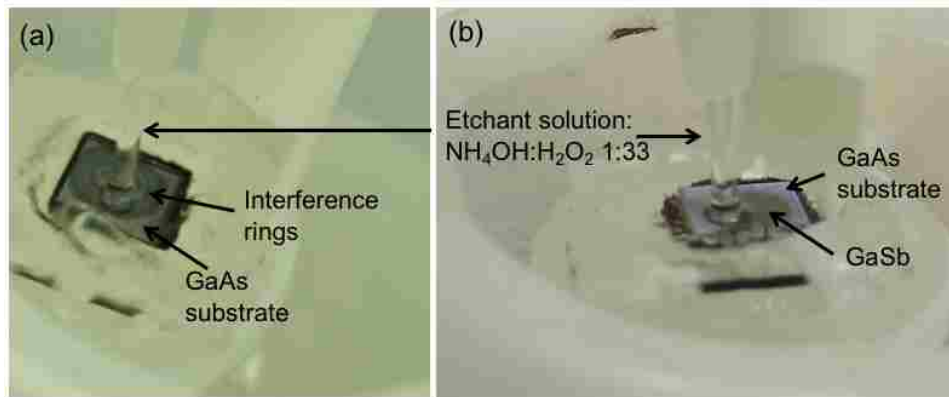
FIG. 3.8 IMAGE OF ETCHANT REACHING (A) THE ALGAAS INDICATED BY INTERFERENCE RINGS AND (B) THE GASB EPITAXIAL LAYER.

For samples A and B, a distinct color change is observed as the etch approaches the $Al_{0.85}Ga_{0.15}As$ etch stop layer as shown in Fig 3.8a. This color change phenomenon is due to thin-film interference effects and oxidation of the $Al_{0.85}Ga_{0.15}As$ layer. When the entire substrate is removed, as evidenced by the thin-film interference, the etch is stopped by quenching the sample in DI water. The $Al_{0.85}Ga_{0.15}As$ etch stop layer is then removed by soaking the sample for 30 seconds in an $NH_4F:HF$ solution at a volume ratio of 6:1. The sample is then rinsed in DI water and dried with nitrogen. For sample C, the color change due to thin-film interference is not as obvious as for samples A and B as sample C does not have an etch stop layer.

Nonetheless, once the etch reaches the GaSb layer a specular gray color is observed as shown in Fig 3.8b. As the GaAs is completely removed, the whole surface turns to the color of GaSb. At this point, the etch is stopped, and the sample is rinse in DI water and dry with nitrogen.

Fig. 3.9 shows results from omega-two theta HR-XRD study of the three structures before and after the etch process. The pre-etch diffraction spectrum of structure A distinctly shows all three layers of the structure. The GaAs substrate along with the AlGaAs etch stop layers are clearly visible along with the GaSb epitaxial layer. In the post-etch diffraction spectrum, only the GaSb and GaAs epitaxial layer peaks are present indicating that the GaAs substrate and etch stop layer were successfully removed. Similarly, post-etch diffraction spectrum of structure B and C only shows the GaSb epitaxial layer peak. This is a clear indication that the selective etch has worked for all three structures.
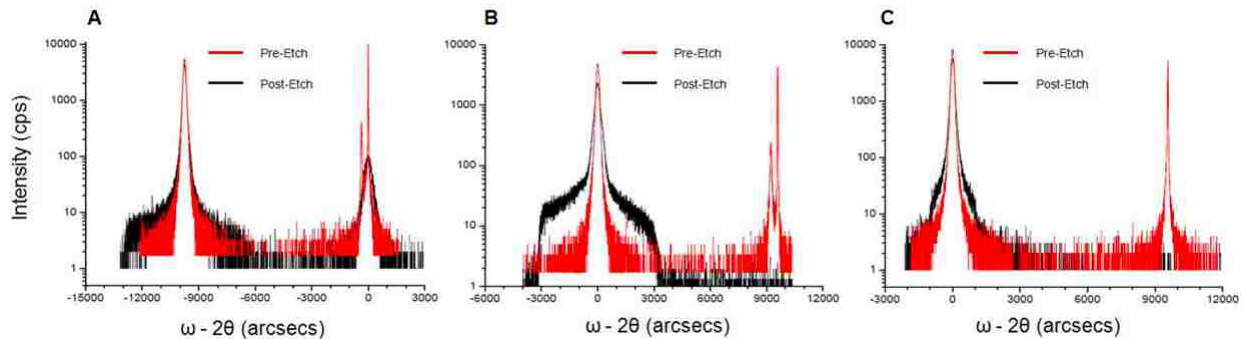
FIG. 3.9. PRE- AND POST-ETCH OMEGA -2 THETA (004) HIGH-RESOLUTION X-RAY DIFFRACTION SPECTRA OF GASB EPILAYERS FOR THE THREE STRUCTURES GROWN.

Finally, the surface quality of the etched surfaces is characterized. A comprehensive analysis of the surface quality was done using both Nomarsky microscopy and atomic force microscopy. However, Nomarsky images of the etched surfaces are featureless and highly specular. The investigation of the surfaces at higher resolutions using atomic force microscopy (AFM) shows some variations in the surface roughness values. Sample C which does not include any AlGaAs

etch stop layer and is the direct growth of GaSb on GaAs has resulted in the lowest root-mean-square (RMS) roughness value of 1.3 nm. This result encouraged the further investigation of the etch contrast between GaSb and GaAs which is described in the next subsection.

3.3.1.1 Etch Contrast between GaAs and GaSb

While numerous studies have been done to investigate the selective etching of GaAs versus AlGaAs [2-5], there is almost no report of a similar study between GaAs and GaSb. The only publication that was found to report on a selective etchant for GaAs against GaSb is by DeSalvo *et al.* who showed that citric acid solution etches GaAs more rapidly than GaSb, with a selectivity of 349 [19]. A possible reason for the lack of studies in selective etching between GaAs and GaSb is the complex nature of the mismatched growth of GaSb on GaAs. Nonetheless, with the IFM technique that decreases the dislocations on metamorphic GaSb epitaxial layers, the etch contrast between GaAs and GaSb becomes important for the realization of novel thin film antimonide devices. In this study, the etch rates of $NH_4OH:H_2O_2$ and $C_6H_8O_7:H_2O_2$ for GaAs and GaSb are investigated to determine the etch contrast between GaAs and GaSb.

To establish the etch rates of GaAs and GaSb using $C_6H_8O_7:H_2O_2$ and $NH_4OH:H_2O_2$ solutions, (100)-oriented GaAs and GaSb substrates are used. Prior to the etching experiments, the substrates are patterned using AZ4330 photoresist, cleaved into 5 mm x 7 mm rectangles, and mounted on a glass slide. $C_6H_8O_7:H_2O_2$ etchant solution is prepared with a volume ratio of 10:1 according to the recipe in DeSalvo's publication [19]. $NH_4OH:H_2O_2$ etch solution is prepared with a volume ratio of 1:33. GaAs substrates are etched for 1 min, 5 min, 10 min, 15 min, and 30 min, while GaSb substrates are etched for 1 min, 15 min, 30 min, 60 min, and 120 min on

account of the slower anticipated etch rates of GaSb compared with GaAs. The etches are initially performed with both a stirring magnet and a jet etcher. The stirring magnet approach leaves a residue on the edges of the sample, while the jet etching process gives a clean, residue-free surface and edges as shown by the scanning electron microscopy (SEM) images in Fig 3.10. Thus, all etches in this study are performed using a jet etcher. It must be noted that the use of a stirring magnet versus a jet etcher under very similar etch conditions could result in very different etch rates. Upon performing the etch for a specific duration, the samples are thoroughly rinsed with DI water and dried with N_2. The remaining photoresist is then removed with acetone. A stylus profilometer with uncertainty of 1 nm is used to measure the etch depths of the samples and SEM is used to characterize the etch profiles.
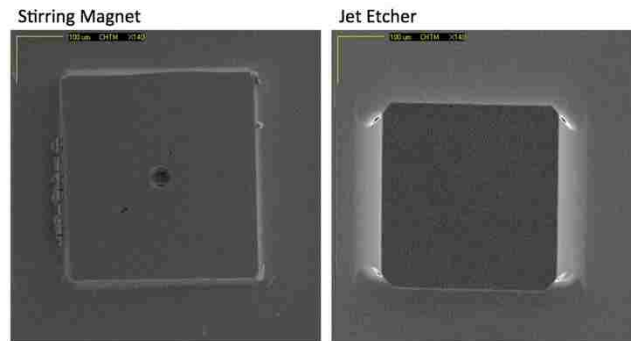
FIG. 3.10 SEM IMAGES OF MESAS ETCHED BY SOLUTION AGITATED WITH A STIRRING MAGNET AND A JET ETCHER

Fig. 3.11 shows plots of average etch depth versus etch time for both etchant solutions. The error bars in the graphs represent the standard deviation from the mean etch depth. The calculated etch rates from these measurements are summarized in Table 3.1. The etch rates of the GaAs substrates increase with time. The etch rates were expected to be constant, especially for the $C_6H_8O_7$:H_2O_2 solution. Nonetheless, is clear that the etch rate of GaAs with NH_4OH:H_2O_2 is considerably faster than with $C_6H_8O_7$:H_2O_2. For GaSb substrates, the etch rate decreases

drastically after the 1 min etch time. It is believed that this is due to initial faster etching of the

native oxide on the GaSb surface. After 1 min etch time, the etch rate of GaSb using

$C_6H_8O_7$:H_2O_2 stays almost constant but the etch rate of GaSb using NH_4OH:H_2O_2 keeps

decreasing with increased etch time. The variation in etch rate with etch time may be due to

degradation of the etchant solutions. The selectivity of each etchant was calculated by dividing

the etch rate of GaAs by the etch rate of GaSb at the common etch times of 1 min, 15 min, and

30 min. The resulting selectivities for $C_6H_8O_7$:H_2O_2 range from 12 ± 5 to 143 ± 2, and those for

NH_4OH:H_2O_2 range from 300 ± 200 to $11,000 \pm 2000$. Despite the fluctuations in etch rate and

selectivity, the NH_4OH:H_2O_2 solution shows a greater etch rate differential between GaAs and

GaSb than the $C_6H_8O_7$:H_2O_2 solution.
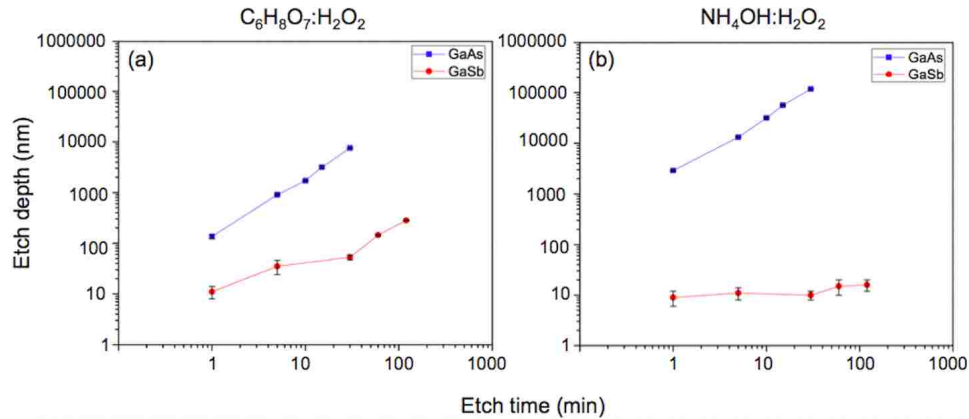
FIG. 3.11 ETCH DEPTH MEASUREMENTS FOR GaAs AND GaSb SUBSTRATES AS A FUNCTION OF ETCH TIME: AFTER ETCHING THE SUBSTRATES WITH (A) $C_6H_8O_7$:H_2O_2 AND (B) NH_4OH:H_2O_2.

TABLE 3.1. Etch rate summary

	Etch Rate, Mean ± Standard Deviation (nm/min)					
	GaAs Substrate		GaSb Substrate		Selectivity	
Etch Time (min)	$C_6H_8O_7$:H_2O_2	NH_4OH:H_2O_2	$C_6H_8O_7$:H_2O_2	NH_4OH:H_2O_2	$C_6H_8O_7$:H_2O_2	NH_4OH:H_2O_2
1	135 ± 30	2880 ± 582	11.10 ± 3.58	9.00 ± 3.22	12 ± 5	300 ± 200
5	181 ± 9	2636 ± 109				
10	171 ± 5	3167 ± 111				
15	211 ± 11	3723 ± 75	2.33 ± 0.76	0.71 ± 0.23	90 ± 30	5000 ± 2000
30	253 ± 3	3900 ± 39	1.77 ± 0.01	0.34 ± 0.05	143 ± 2	$11,000 \pm 2000$
60			2.40 ± 0.09	0.25 ± 0.08		
120			2.33 ± 0.03	0.13 ± 0.04		
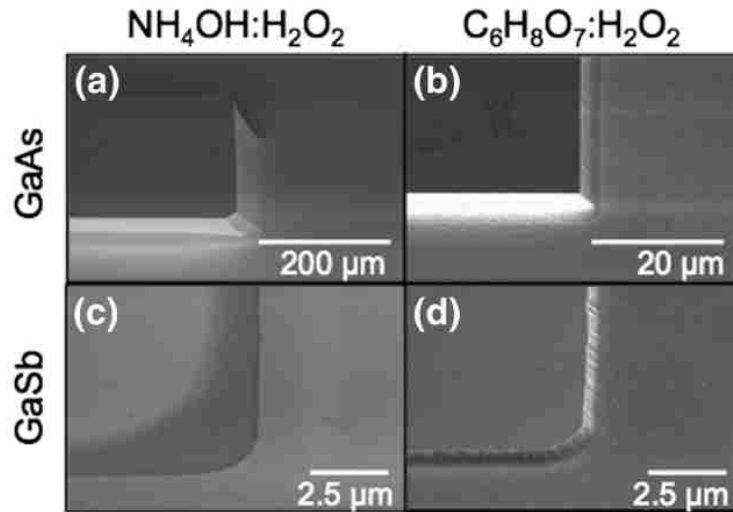
FIG. 3.12 SEM IMAGES COMPARING THE ETCH PROFILES OF GaAs AND GaSb: (A) AND (B) GaAs SUBSTRATE AFTER BEEN ETCHED FOR 15 MIN IN $C_6H_8O_7$:H_2O_2 AND NH_4OH:H_2O_2, RESPECTIVELY; (C) AND (D) GaSb SUBSTRATE AFTER BEEN ETCHED FOR 2 HOURS IN THE MENTIONED SOLUTIONS.

Fig. 3.12 shows SEM images comparing the etch profiles of GaAs and GaSb. Fig. 3.12a and 3.12b show GaAs substrates after being etched for 15 min with NH_4OH:H_2O_2 and $C_6H_8O_7$:H_2O_2, respectively. Similarly, Fig 3.12c and 3.12d show GaSb substrates after being etched for 2 hours with the mentioned solutions. From the scale on the SEM images, it is evident that the deepest etch profile is for GaAs etched with NH_4OH:H_2O_2. In addition, Fig. 3.12c and 3.12c show that the etchants have a minimal effect on GaSb substrates. Nevertheless, $C_6H_8O_7$:H_2O_2 gives GaSb substrates a slightly more pronounced etch profile and a rougher surface than NH_4OH:H_2O_2. These results provide an excellent estimate for the behavior of the etchants in substrate removal and isolation of GaSb epitaxial layers grown on GaAs substrates.

3.3.1.2 GaAs Substrate Removal without Etch Stop Layer

To investigate the effectiveness of the two etchants for isolation of GaSb membranes, 2 μm thick layers of GaSb are metamorphically grown on GaAs substrates using the previously

described technique of forming interfacial misfit dislocation arrays. The grown samples are cleaved into 1 cm x 1 cm squares, chemically cleaned, and bonded to a glass slide with epitaxial side down. The GaAs substrates are etched with $NH_4OH:H_2O_2$ and $C_6H_8O_7:H_2O_2$ using the jet etcher. The crystal quality and surface morphology of the GaSb membranes before and after the substrate removal process are characterized with HR-XRD and AFM. The RMS surface roughness of the samples was estimated on areas of 3 μm x 3 μm. Eight AFM scans were done for each sample.

Both etchant solutions successfully achieved removal of the GaAs substrate and subsequent isolation of the GaSb membranes without the need for an etch-stop layer, as the significant difference in the etch rate of GaSb and GaAs is sufficient to etch the substrate with minimal damage to the GaSb epitaxial layer.

Fig. 3.13 shows $\omega - 2\theta$ HR-XRD results from symmetric scans. Figure 3.13a shows the diffraction spectrum before the etch process, which indicates the presence of GaSb and GaAs. The presence of two distinct peaks with the absence of a pseudomorphic growth region is very typical of metamorphic layers grown using interfacial misfit dislocation arrays [19]. The full-width at half-maximum (FWHM) of the GaSb peak is 250 ± 8 arcsec, indicating good crystal quality. After symmetric and asymmetric XRD scans, calculations show that the GaSb epitaxial layer is almost 100% relaxed. After the etch process, the substrate peaks no longer appear in the diffraction spectrum, indicating its successful removal. The remaining GaSb epitaxial layer peak after removing the GaAs substrate with $C_6H_8O_7:H_2O_2$ has FWHM of 270 ± 10 arcsec, and the one remaining after using $NH_4OH:H_2O_2$ has FWHM of 290 ± 10 arcsec. Therefore, it can be concluded that isolated GaSb layers have the same crystal quality than when they were on the substrate.
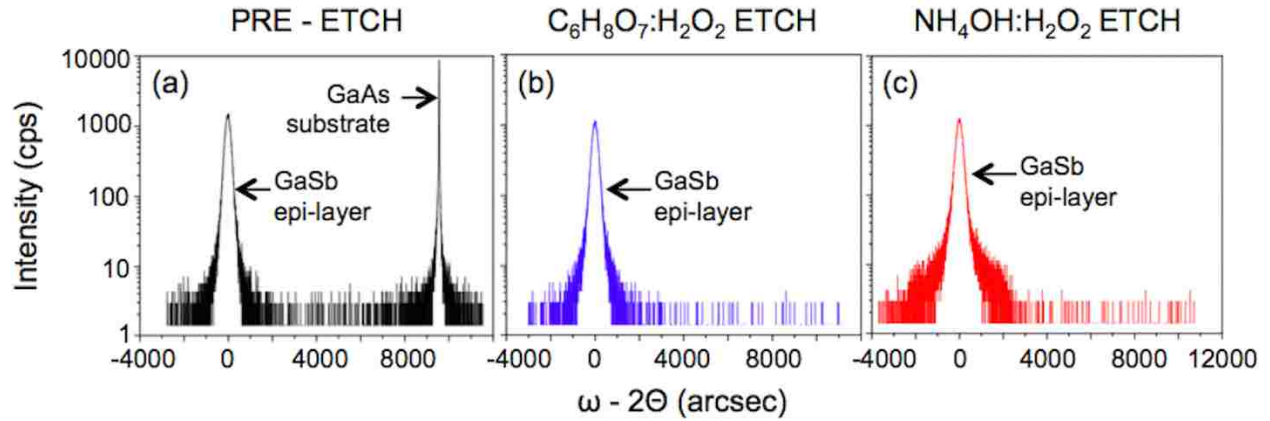
FIG. 3.13 PRE- AND POST-ETCH $\omega - 2\theta$ (004) HIGH-RESOLUTION X-RAY DIFFRACTION SPECTRA OF GASB/GAAS SAMPLES: (A) BEFORE THE ETCH PROCESS, AND AFTER ETCHING AWAY THE GAAS SUBSTRATE WITH (B) $C_6H_8O_7$:H_2O_2 AND (C) NH_4OH:H_2O.

The surface morphology of the GaSb membranes before and after substrate removal are shown by AFM micrographs in Fig. 3.14. The GaSb epitaxial layer metamorphically grown on GaAs exhibits an RMS surface roughness value of 1.5 ± 0.4 nm. The surface roughess of the GaSb film isolated by etching the substrate with $C_6H_8O_7$:H_2O_2 has an RMS value of 2.6 ± 0.8 nm and that isolated by using NH_4OH:H_2O_2 has an RMS value of 0.9 ± 0.2 nm. The GaSb surface etched with NH_4OH:H_2O_2 is smoother than the epitaxial surface.
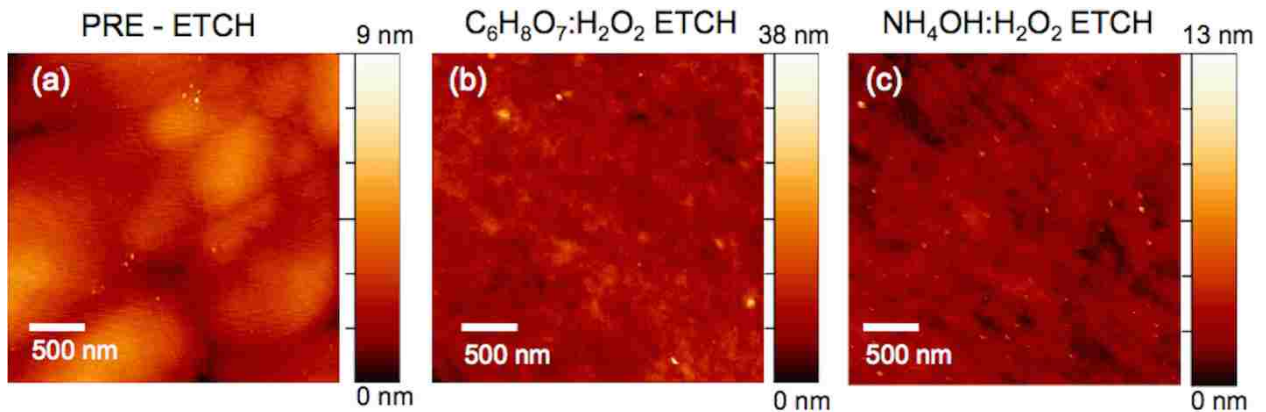
FIG. 3.14 PRE- AND POST-ETCH $\omega - 2\theta$ (004) HIGH-RESOLUTION X-RAY DIFFRACTION SPECTRA OF GASB/GAAS SAMPLES: (A) BEFORE THE ETCH PROCESS, AND AFTER ETCHING AWAY THE GAAS SUBSTRATE WITH (B) $C_6H_8O_7$:H_2O_2 AND (C) NH_4OH:H_2O.

It has been shown that the ammonium hydroxide base etchant has a greater etch rate differential for the GaSb/GaAs material system than the citric acid base etchant. The selectivity of $NH_4OH:H_2O_2$ for GaAs/GaSb ranges from 300 ± 200 to $11,000 \pm 2000$, whereas that of $C_6H_8O_7:H_2O_2$ ranges from 12 ± 5 to 143 ± 2. The selectivity of the etchant solutions increased with time, as the etch rates seem to be strongly dependent on etch time. Despite the difference in selectivity, successful isolation of 2 μm thick GaSb epitaxial layers is demonstrated by etching away the substrate with either etchant without the need for an etch-stop layer. The combination of this highly selective etch process, and the interfacial misfit dislocation growth technique offers an alternative for III-Sb-based optoelectronic devices, which often need thinning or complete removal of GaSb substrates to improve their performance.

3.3.1.3 Freestanding Thin Film Metamorphic GaSb diodes after Substrate Removal

Metamorphic p-i-n GaSb diodes are grown on GaAs substrates to study the performance of such devices without substrates. A photodetector mask with top-top contacts was used to process the diodes. The photodetector mask has apertures of 50 um, 100 um, 150 um, 200 um, 300 um. The diodes are fabricated by standard photolithography and dry etching. Fig 3.15 shows a schematic of the processed diode. The processing was initiated by etching the mesas 0.5 μm below the i-GaSb epitaxial layer, using an inductively coupled plasma reactor with BCl_3 gas. Next, top and bottom metal contacts were deposited via e-beam evaporator. The contacts for p-GaSb consist of Ti/Pt/Au and the ones for n-GaSb consist of Ni/Ge/Au/Pt/Au. The diodes are fully processed and tested before removing the substrate.

p-contact
Ti(500 Å)/ Pt(500 Å)/ Au(3000 Å)

1 µm p-GaSb 10^{17} cm^{-3}

0.25 µm i-GaSb

2 µm n-GaSb 10^{17} cm^{-3}

SI-GaAs

n-contact
Ni(87 Å)/Ge(560 Å)/ Au(233 Å)/ Pt (476 Å)/ Au(3000 Å)
Annealed at 290 °C for 45 sec.
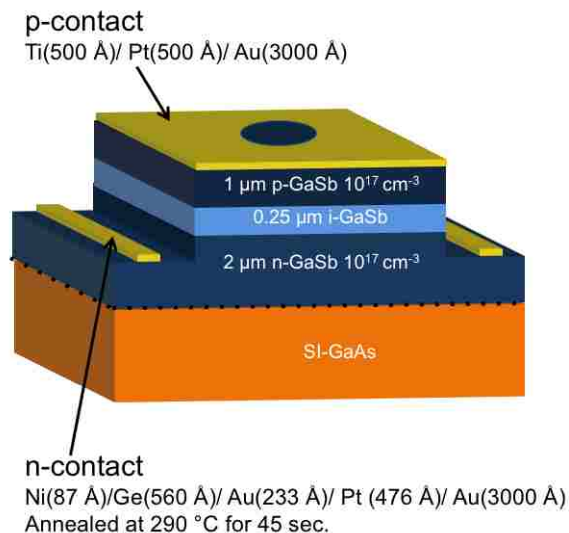
FIG. 3.15 SCHEMATIC OF PROCESSED P-I-N GASB DIODE

After characterizing the diodes on the substrate, the samples are cleaved into 1 cm x 1 cm

pieces and bonded to a glass slide with the processed side down using a crystalbond^{TM} 509

adhesive. Then, the GaAs substrate is etched away with a $NH_4OH:H_2O_2$ 1:33 solution in the jet

etcher as described in the previous section. Once the substrate is removed, the sample is left in

acetone overnight to dissolve the crystalbond^{TM} 509 adhesive and detach the diode from the glass

slide. Once the adhesive is dissolved, the isolated thin film floats on the acetone, and it is ready

to be transfer to a host substrate. However, the transfer is a difficult procedure. The film cannot

be pick up by tweezers as it is fragile and it can break. The diodes can be scooped out with a

glass slide, and if the contacts are facing up, then they can be tested on the glass slide. However,

if the metal contacts of the diodes are facing the glass slide, then they need to be retransferred.

In this case, a piece of scotch tape is used to lift the diodes from the glass slide. The process is

summarized in Fig 3.16. A photograph and a Nomarski image of the transferred diodes to scotch

tape are shown in Fig 3.17. Nomarski images shows some fractures on the bottom contacts.
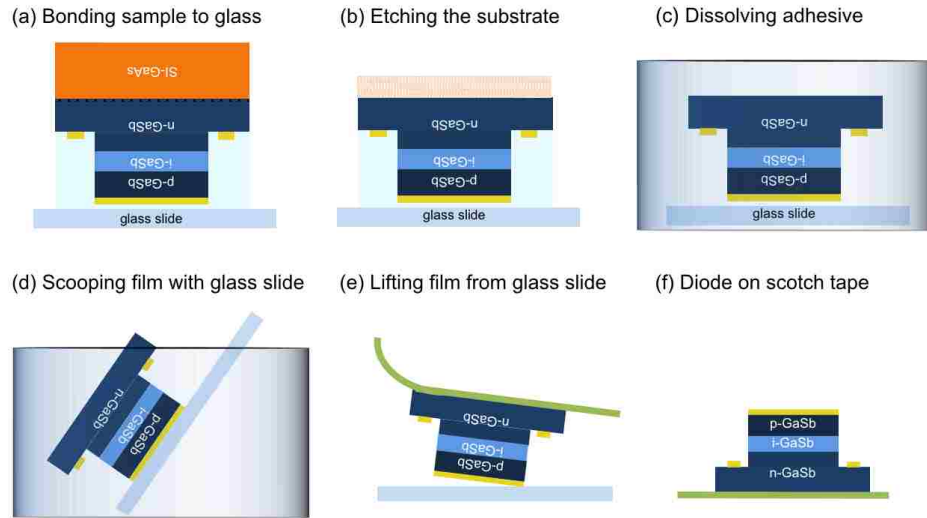
FIG. 3.16 SCHEMATIC OF PROCEDURE FOR SUBSTRATE REMOVAL AND TRANSFER OF THIN FILM DIODE TO HOST SUBSTRATE
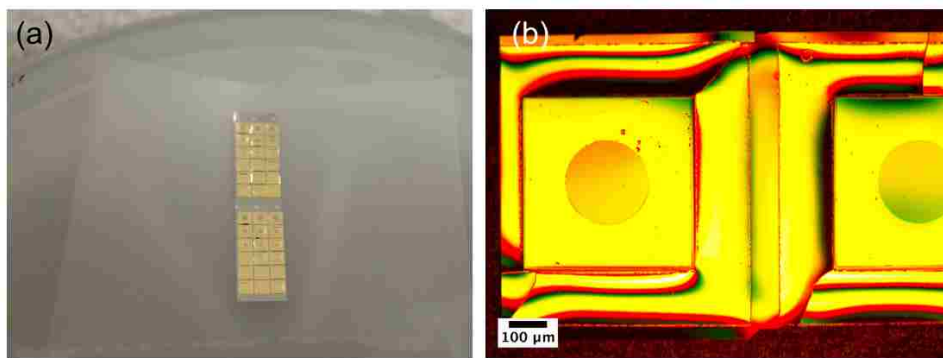
FIG. 3.17 (A) PHOTOGRAPH AND (B) NOMARSKI IMAGE OF DIODES TRANSFERRED TO SCOTCH TAPE

The thin film diodes were tested with by 4-probe measurement before and after substrate removal. A representative plot of the dark J-V characteristics is presented in Fig 3.18. In the forward bias regime, the photodiode shows a turn-on voltage of about 0.3 V when is on the GaAs substrate and when is on the scotch tape. In the reverse bias region, the diode exhibits high leakage current without a defined breakdown voltage. This may be due surface leakage from the mesa walls and to the residual threading dislocations from the lattice mismatch.
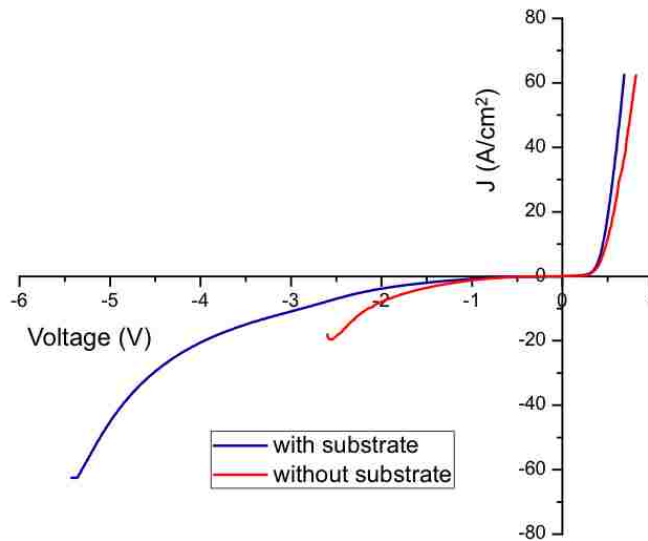
FIG. 3.18 DARK J-V CHARACTERISTICS OF P-I-N DIODES BEFORE AND AFTER SUBSTRATE REMOVAL

Having a working thin film diode is very promising for the achievement of thin film TPV devices. However, a different process must be developed for the TPV cells as they must have contacts on both sides of the film.

3.3.2 Epitaxial Lift Off of Metamorphic GaSb Thin Films

Epitaxial lift-off (ELO) of metamorphic GaSb epitaxial layers is a more attractive isolation technique than the substrate removal technique. Growing on GaAs substrates minimizes the cost of III-Sb semiconductors as GaAs substrates are less expensive and available in larger sizes than GaSb substrates and ELO can even further reduce this cost since the GaAs substrate can potentially be reused. The ELO process involves the lateral etch of a sacrificial layer with a highly selective etchant that enables the separation of the device from the substrate with minimal damage to either. Hence, ELO technology has the potential to considerably reduce the cost of devices as the original substrate can be reused for more growths [20].

69

ELO is mostly used in AlAs/GaAs systems where the GaAs epitaxial layer is separated from the GaAs substrate by the lateral etch of an AlAs or a high aluminium content AlGaAs sacrificial layer with hydrofluoric (HF) acid [7]. The high selectivity of HF for AlAs leaves the GaAs epitaxial layer and GaAs substrate intact [7].

Structure A and B (described above) are used to explore the possibility of applying lift off techniques to isolate GaSb metamorphic membranes from GaAs substrates. Along with these structures, a GaAs/AlGaAs/GaAs was etched to compare the process to the well-known system. The samples are cleaved into 1 cm x 1cm squares and rinsed with acetone, methanol, isopropanol and DI water. The epitaxial side of the sample was adhered to a piece of thermal tape. The samples bonded to the thermal tape were then immersed in a 49% hydrofluoric acid (HF) solution. After been submerged in HF for 24 hours, lift off progress of the GaAs/GaSb epitaxial layer from structure A is observed as shown in fig 3.19a. After two days in HF, the films lifted off completely from the GaAs substrates as shown in Fig 3.19b.
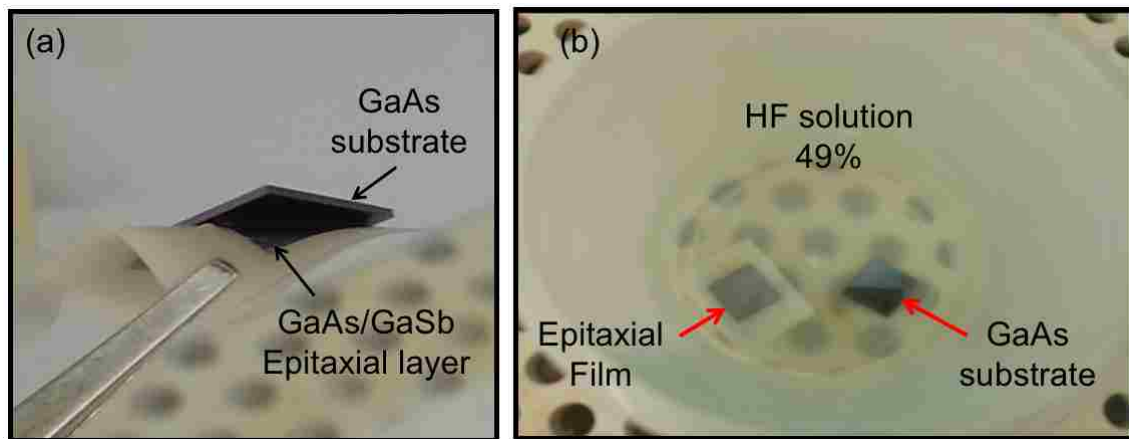
FIG. 3.19 IMAGES OF THE ELO PROCESS: (A) ELO PROGRESS AFTER 1 DAY SUBMERGED IN 49% AND (B) COMPLETE ISOLATION AFTER 2 DAYS IN HF.

After the complete etch of the AlGaAs sacrificial layer, the samples are rinsed with DI water and dried with nitrogen. A Nomarski microscope is used to study their surface morphology. Fig

3.20 shows images of the epitaxial layers after ELO. Fracturing is evident in the GaAs epitaxial layer from the control sample but Nomarski images, Fig 3.21, reveal fracturing for the other two structures as well. In addition, the GaSb epitaxial layer from structure B shows some signs of oxidation on the edges which may be due to HF etching at the edges.
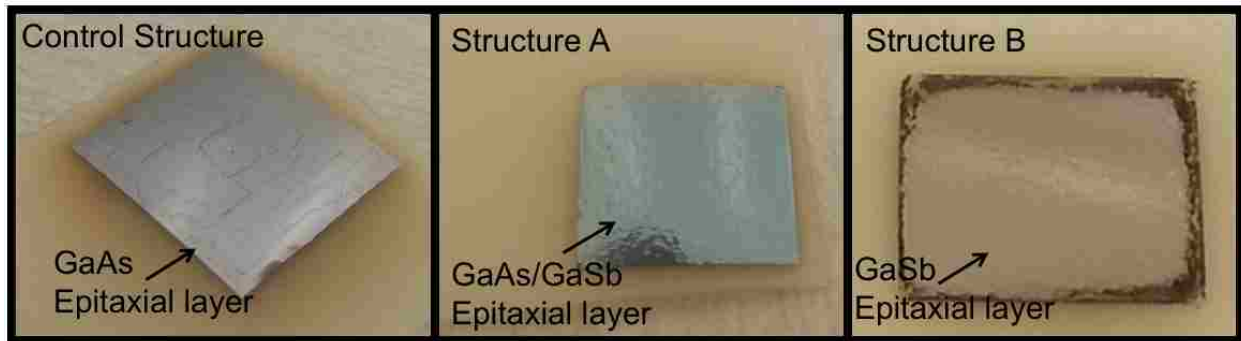
FIG. 3.20 IMAGES OF EPITAXIAL LAYERS AFTER ELO
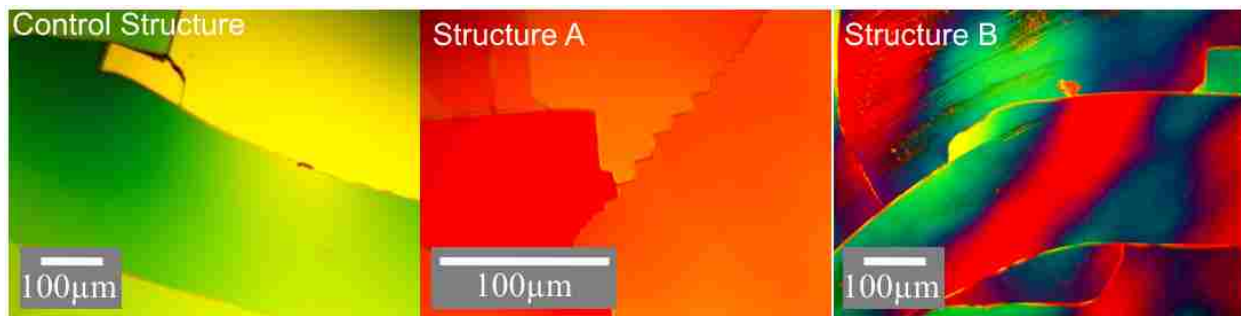
FIG. 3.21 NOMARSKI IMAGES OF EPITAXIAL LAYERS AFTER COMPLETE ETCH OF THE ALGAAS SACRIFICIAL LAYER

The degradation of the crystal quality is also observed in the diffraction spectra of HR-XRD as shown by Fig 3.22. The FWHM of the post-ELO peaks is significantly larger than the pre-ELO peaks. Although the application of the ELO process was successful, further optimization of the process must be done to improve the overall quality of the films.
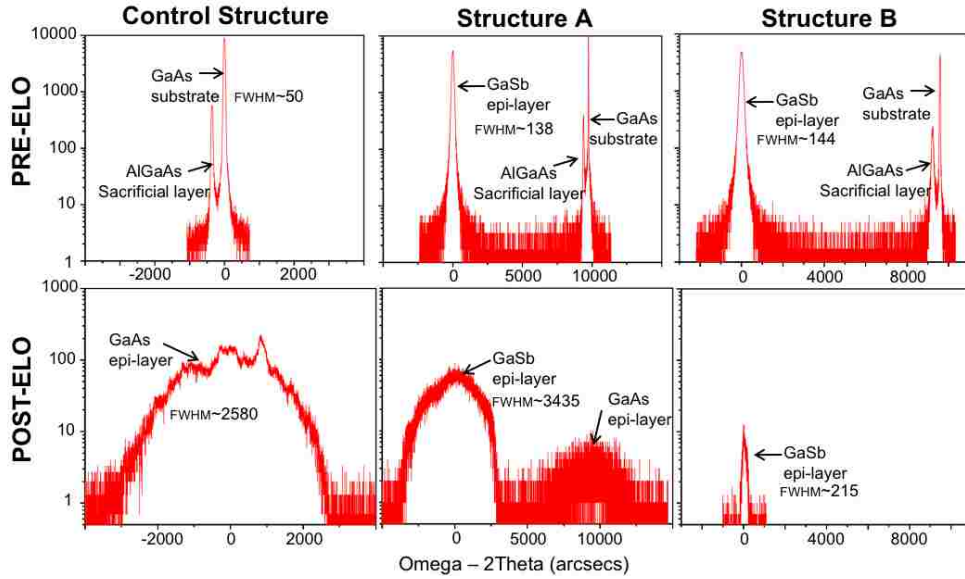
FIG. 3.22 PRE- AND POST-ELO $\omega - 2\theta$ (004) HIGH-RESOLUTION X-RAY DIFFRACTION SPECTRA OF ELO STRUCTURES

After doing some literature search, a way to avoid cracking of samples is found. Hageman *et al*. reported that a metal film of gold or copper between the structure and the Apiezon wax prevents crack formation in the thin film [20]. Hence, the samples are metallized with 2 μm of copper via electron beam evaporation. Then they are cleaved, and black wax (Apiezon wax) is melted on their surface. Before putting the samples in HF, the edge walls of the samples are cleaned with toluene to make sure there is no residue of black wax to obstruct the ELO process. Using copper completely solved the fracturing problem as shown in Fig 3.23b.
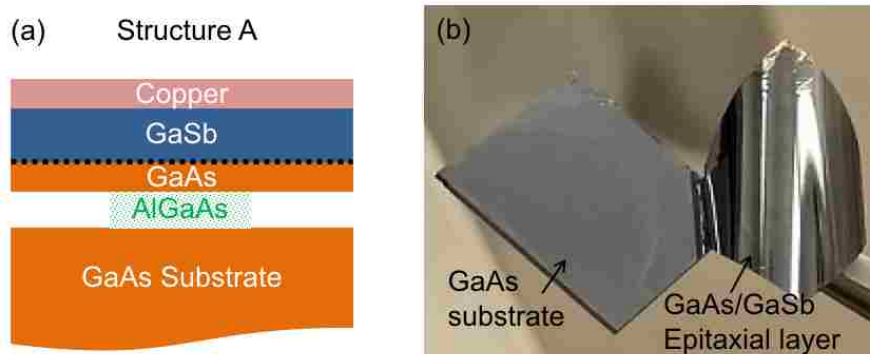
FIG. 3.23 (A) SCHEMATIC OF ELO FOR STRUCTURE A. (B) IMAGE OF EPITAXIAL FILM RELEASED AFTER ELO

72

The ELO of structure A releases a GaAs/GaSb epitaxial film as shown in Fig 3.23. The remaining 100 nm of GaAs in the GaAs/GaSb epitaxial film can be etch away with either $NH_4OH:H_2O_2$ or $C_6H_8O_7:H_2O_2$. As mentioned in the previous sections these solutions have a preference for GaAs than for GaSb.

The ELO of structure B releases the 3 µm thick GaSb epitaxial film as shown in Fig 3.24. After dissolving the black wax in toluene, the released film curls into a cone shape. Nonetheless, the released GaSb films shows some oxidation, probably due to HF etching. Berishev *et al.* studied a $H_2O_2:HF:C_4O_6H_6$(tartaric acid)$:H_2O$ solution for chemical polishing of GaSb wafers with HF concentrations varying from 0.0 to 5.0 mol . It was found that when the concentration of HF was lower than 1.5 mol, the resulting surface was mirror-like but when the concentration of HF was higher than 1.5 mol, the surface was rough and dark. Since the dark layer was insoluble in acids, it was believed to be formed by antimony oxide Sb_2O_5. It must be noted that when the HF concentration was 0.0 mol, there is was no etching of GaSb and no change in surface morphology. Therefore, oxidation can be attributed mainly to HF. Hence, structure A is a better option to make devices as the GaAs epitaxial layer protects the GaSb epitaxial layer from HF etching.
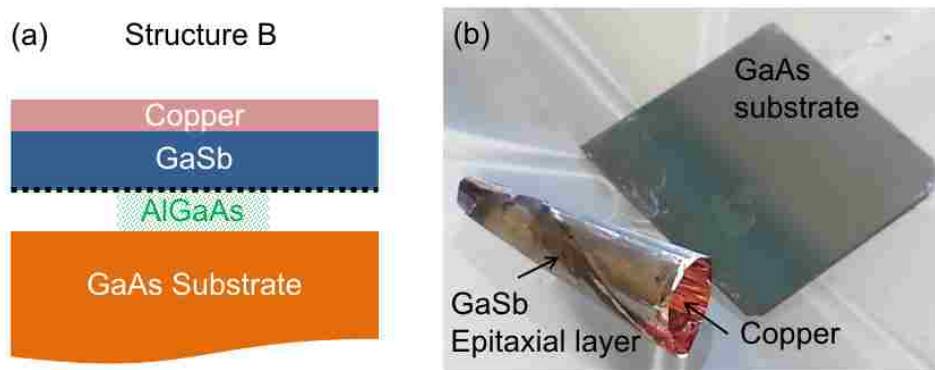
FIG. 3.24 (A) SCHEMATIC OF ELO FOR STRUCTURE B. (B) IMAGE OF EPITAXIAL FILM RELEASED AFTER ELO.

3.4 Design, Fabrication, and Performance of Metamorphic GaSb TPV devices

Since the isolation of GaSb membranes from GaAs substrates is possible, the next step is to fabricate metamorphic GaSb TPV devices. For this, the GaSb TPV structure described in the previous chapter, and summarized again in table 3.2, is grown on a GaAs substrate by the IMF technique.

TABLE 3.2. GaSb TPV structure on GaAs substrates

Layer	Material	Thickness (μm)	Doping type & concentration (cm^{-3})
Contact	GaSb	0.10	(p^{++}) 5 x 10^{18}
Window	AlSb	0.03	(p^{+}) 1 x 10^{18}
Emitter	GaSb	0.50	(p) 5 x 10^{17}
Base	GaSb	2.50	(n) 4 x 10^{17}
BSF	AlSb	0.30	(n^{+}) 1 x 10^{18}
Contact	GaSb	0.20	(n^{++}) 5 x 10^{18}
		n-type GaAs substrate	

The device fabrication is performed using standard photolithography and dry etching techniques. First, the back contacts (Ge/Au/Ni/Au) are deposited on the n-GaAs substrate via e-beam evaporation. To make the n-contacts ohmic, the sample is annealed at 380°C for 60 seconds. Next, the sample is patterned to deposit the metals for the top-contacts which are Ti/Pt/Au. Finally, the devices are isolated by etching the mesas below the p-n junction using an inductively coupled plasma reactor with BCl$_3$ gas.

Fig. 3.25 shows the J-V characteristics of a metamorphic GaSb TPV on a GaAs substrate (IMF cell), and a lattice-matched GaSb TPV on a GaSb substrate (control cell) under AM1.5G illumination. Both devices have an area of 0.5 cm x 0.5 cm. The IMF cell exhibits an open-circuit voltage (V$_{OC}$) of 0.12 V, a short-circuit current density (J$_{SC}$) of 18.38 mA/cm^2, a fill factor (FF) of 34%, and an efficiency (η) of 0.74%. In contrast, the control cell shows a V$_{OC}$ of 0.31 V, a J$_{SC}$ 25.24 mA/cm^2, a FF of 52 % and a η of 4.3 %.
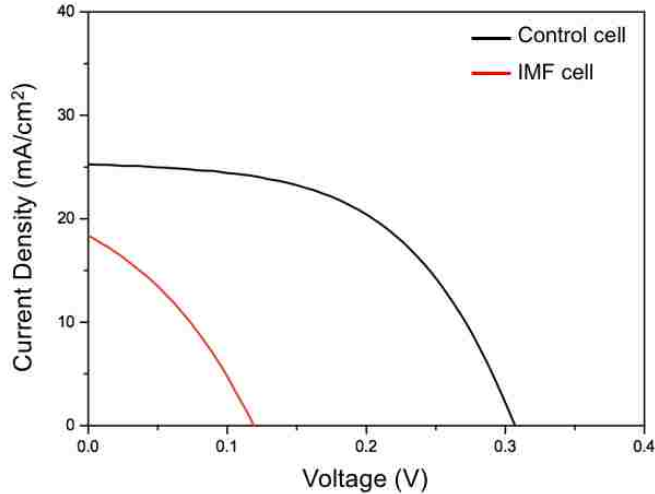
FIG. 3.25 J-V CHARACTERISTICS OF GASB TPV CELLS UNDER AM1.5G ILLUMINATION

The control cell outperforms the IMF cell, which is not a surprise. Similar results had been reported before [21-22]. Juang *et al.* reported J-V characteristics of IMF GaSb TPV diodes with circular mesas of 400 μm in diameter under 1 sun illumination. These diodes exhibited a V_{OC} of 0.12 V, a J_{SC} 15.5 mA/cm^2, and a FF of 40 %. In conclusion, the residual threading dislocations due to the lattice-mismatch are degrading the performance of the metamorphic devices. GaSb cells on GaAs substrates is a promising idea if the threading dislocation density is further reduced. The next chapter shows the work done to improve the performance of these metamorphic GaSb TPV devices. Meanwhile, these IMF cells are used to demonstrate the integration thin film GaSb devices to CVD diamond.

3.5 Integration of Metamorphic GaSb Thin Films Diodes to CVD Diamond

For the integration of freestanding thin film TPV devices to thermal grade CVD diamond, two approaches are attempted. The first approach is a top-side approach which involves the processing of the diodes while still attached to the GaAs substrate. Then the fabricated diode membrane is isolated from the substrate and subsequently transferred onto the diamond. The second approach is an inverted or bottom-side approach which starts with the metallization of the

75

epitaxial surface (a metal blanket for the bottom contacts) followed by the bonding of the GaSb/GaAs to CVD diamond. Then, the substrate is etched off leaving behind the GaSb membrane on CVD diamond, which can then be processed for contacts. The top-side approach is an easier process for the fabrication of the metal grid, but the transfer of the membrane and bonding it to CVD diamond is very difficult. The bottom-side process provides a robust bond to diamond but requires fabrication of metal grid on the membrane attached to CVD diamond, which presents some challenges.

3.5.1 Top-side Approach
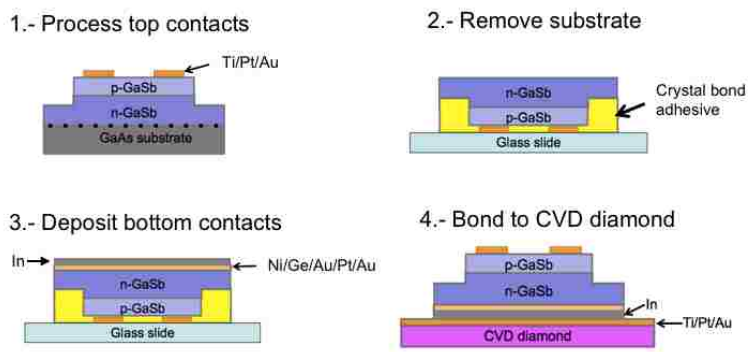
FIG. 3.26 SCHEMATIC OF FLOW PROCESS FOR TOP-SIDE APPROACH

The process for the top-side approach starts with the fabrication of a freestanding thin film TPV that is then bonded to the CVD diamond. Fig 3.26 illustrates the four basic steps of the top-side approach. In the first step, the top contacts are deposited, and the devices are isolated by mesa etching. In the second step, the samples are mounted on a glass slide, and the substrate is etched away (ELO is not optimal for this approach as there is no metal blanket on the sample surface to avoid fracturing of the semiconductor films). In the third step, the back contacts are deposited along with an indium (In) layer to help for the subsequent bonding step. In the fourth step, the

device is detached from the glass carrier and bonded to the CVD diamond.

To demonstrate the top-side approach, the metamorphic GaSb TPV structure from the previous section is used. After processing the top contacts and isolating the devices by mesa etching, the sample is cleaved into individual devices to proceed with substrate removal. Once the GaAs substrate is removed, the back side of the TPV is exposed and ready to be metallized with n-type metal contacts. Up to this point, the process has been straight forward. However, depositing the bottom contacts, step 3, is problematic.

During metal evaporation, the sample can be exposed to high temperatures, and since the crystalbond^{TM} 509 adhesive that is holding the thin film TPV to the host substrate melts at 121ºC, there is concern that the adhesive could melt. An option will be to dissolve the adhesive and re-transfer the thin film to another carrier. However, as described in the freestanding thin film metamorphic GaSb diode section, once the semiconductor film is detached from the glass carrier, it is completely fragile and can disintegrate with minimum manipulation. Subsequently, adhesives that could stand higher temperatures were investigated, but they were permanent adhesives so the film could not be release afterwards. Hence, the only choice was to try and deposit the back contacts while the TPV was still attached to the glass carrier with the crystalbond^{TM} 509 adhesive. The adhesive did melt but only on the edges of the sample.

The metal sequence deposited for the back contacts of n-GaSb is 87 Å Ni/ 560 Å Ge/ 233 Å Au/ 476 Å Pt/ 3000 Å Au. These contacts need to be annealed at 290ºC for 45 sec to make them ohmic. However, since the sample will be exposed to heat during the bonding process, the annealing step is skipped. After depositing the n-contacts, the sample is loaded to a thermal evaporator to deposit a 3 μm thick Indium layer which bonding layer due to its low melting point (157ºC).

The next step is to bond the thin film cell to the CVD diamond. Hence, while the fully

processed metamorphic GaSb TPV cell is released from the glass carrier, the CVD diamonds are

coated with 500 Å Ti/ 500 Å Pt/ 3000 Å Au. Once this is done, the freestanding thin film TPV is

transferred to the coated CVD diamond. Now the thin film devices can be handle with tweezers.

The metal blanket deposited for the bottom contacts gives them support and they break less.

Subsequently, the device/indium/diamond stack is placed in a graphite press. Then the graphite

press is placed inside an oven at 160 ºC for 15 min.

3.5.2 Bottom-side Approach

The process flow for the bottom-side approach is shown by the schematic in Fig 3.27. An

inverted structure of the TPV is grown, so the bottom contacts are deposited first along with the

Indium layer used for bonding. In the second step, the sample is bonded to the CVD diamond

just as described in the bonding step of the top-side approach without the complications of

transferring the thin film. In the third step, the substrate is removed. Lastly, in the fourth step,

the top-contacts are processed.
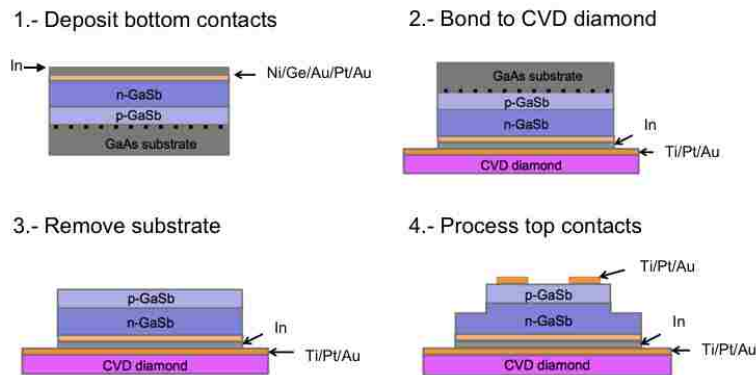
FIG. 3.27 SCHEMATIC OF FLOW PROCESS FOR BOTTOM-SIDE APPROACH

Even though GaAs substrate removal technique has been highly optimized, it did not work as

predicted for the bottom-side approach. Removing the substrate with any of the two solutions

mentioned above end up delaminating the exposed metal on the CVD diamond surface. This is not ideal as this metal is used to probe the bottom contacts of the TPV. To test if the jet etcher was causing the delamination of the metal was left in a stagnant solution of $C_6H_8O_7:H_2O_2$. After a couple of days, the substrate is completely etched away, and there are no signs of delamination as observed in Fig 3.28.

FIG. 3.28 DEMONSTRATION OF GASB AND CVD DIAMOND INTEGRATION BY BOTTOM-SIDE APPROACH AFTER STEP 3

After successful substrate removal, the fragile GaSb membrane is left intact on the CVD diamond. Now, the challenge is to go through all the top-contact processing steps without destroying the thin GaSb film. Although the samples survived the process, the metal grid did not stick to the surface. During metal lift-off, all the metal came off. The photolithography procedure must be optimized for these thin membranes (work still in progress).

3.5.2.1 Bottom-side Approach for Epitaxial Lift-off

The bottom-side approach is crucial if the TPV is isolated by ELO technique. For ELO, it is recommendable to metallize the surface of the sample to prevent crack formation on the thin film. Hence, if the structure is inverted as in the bottom-side approach, the metal blanket for the bottom contacts can help in the prevention of cracks in the film. However, the sample cannot be bonded to the CVD diamond prior to the ELO process. The ELO thin film needs to be flexible so that as the sacrificial layer is etched away, the films curls up a little and allow the byproducts

escape the channel. Therefore, the bottom-side is slightly modified. The TPV is isolated first and then bonded to the CVD diamond.

In an attempt to demonstrate ELO, an inverted version of the GaSb TPV structure in table 3.2 is grown on a GaAs substrate with a 100 nm thick $Al_{0.85}Ga_{0.15}As$ sacrificial layer in between. The fabrication of the thin film ELO TPV cell starts with the metallization of the back contacts (Ni/Ge/Au/Pt/Au for n-GaSb). Then, the sample is bonded to a 50 µm thick Kapton film coated with Cr/Au by using an Au-Au cold welding technique [23]. Then, the sample is submerged in diluted hydrofluoric acid to etch the AlGaAs sacrificial layer. After leaving the sample in HF:H_2O 1:20 for 10 hours, three pieces resulted as shown in Fig 3.29c. Initially, it was believed that the 300 nm AlSb layer etched along with the AlGaAs sacrificial layer leaving the 200 nm GaSb contact layer attached to the Kapton film as shown in Fig 3.29.
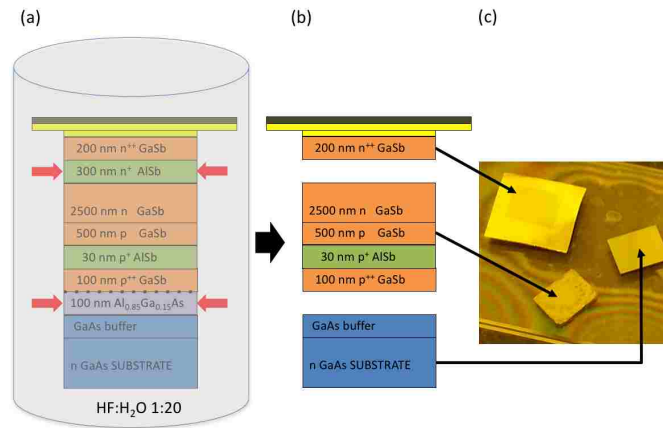
FIG. 3.29 SCHEMATIC THEORIZING WHAT HAPPENED DURING ELO PROCESS OF A METAMORPHIC GASB TPV CELL, (A) LATERAL ETCH OF ALSB AND ALGAAS, (B) AND (C) RESULTS AFTER ELO.

However, when the specimen in the Kapton film is tested by energy-dispersive x-ray spectroscopy (EDS), no GaSb is detected. The EDS spectrum only has an Au peak as shown in Fig 3.30. The middle piece is also analyzed by EDS. The Ga and Sb peaks in the EDS spectrum shown in Fig 3.31 confirms that the released film is GaSb. The process is repeated multiple

times. However, the result is always the same. The metal blanket is detaching from the cell during ELO. The reason for this is unknown. One of the metal may be etching laterally. This will have to be further investigated.
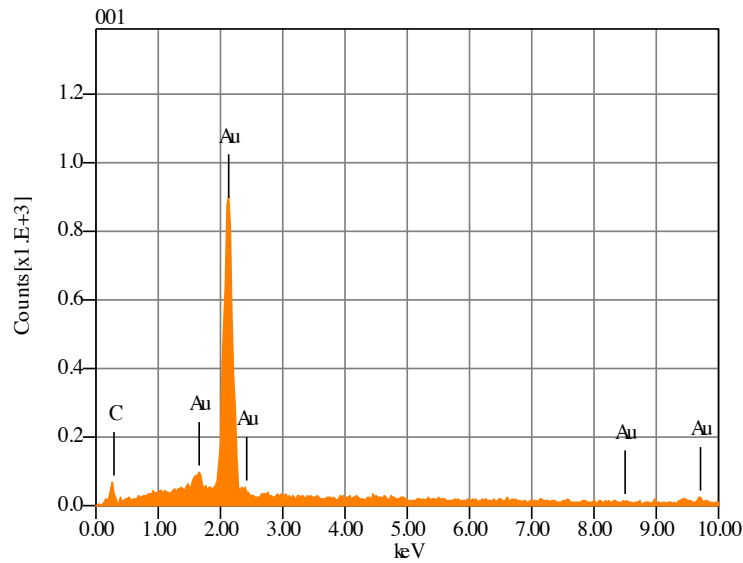
FIG. 3.30 EDS SPECTRUM OF SPECIMENS LEFT ON KAPTON FILM AFTER ELO OF METAMORPHIC GASB TPV
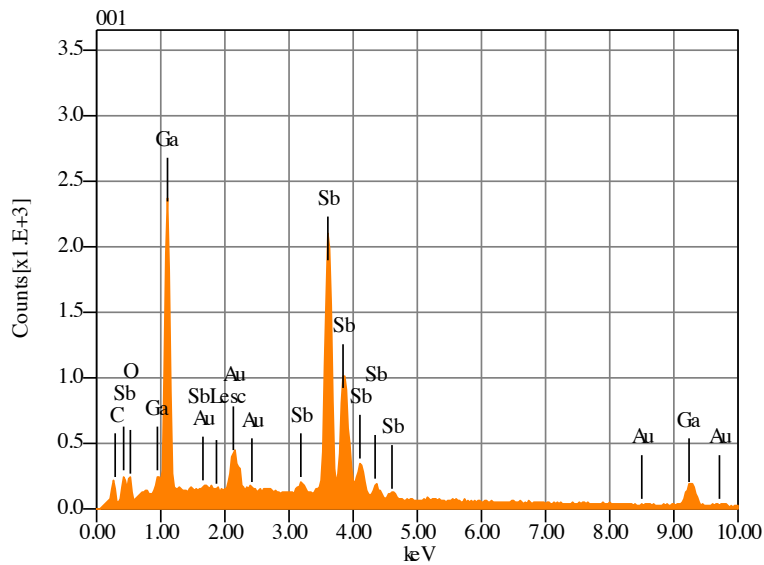
FIG. 3.31 EDS SPECTRUM OF SPECIMENS LEFT ON KAPTON FILM AFTER ELO OF METAMORPHIC GASB TPV

3.6 Conclusion

The possibility of using substrate removal and ELO techniques to fabricate thin film metamorphic GaSb solar cells and then bond them to CVD diamond has been investigated. Even though the ELO of GaSb PV structures was not successful and the GaSb cells on GaAs substrates show a lower efficiency than GaSb cells on GaSb substrates, there is room for improvement. Once the ELO process and the IMF growth mode are optimized, the combination of these techniques will allow the fabrication of low cost GaSb TPV cell and the possibility to integrate them to any other substrate.

References

1. Dier, Oliver, Chun Lin, Markus Grau, and Markus-Christian Amann. "Selective and non-selective wet-chemical etchants for GaSb-based materials." *Semiconductor science and technology*19, no. 11 (2004): 1250.

2. K. Kenefick, "Selective etching characteristics of peroxide/ ammonium-hydroxide solutions for GaAs/Al0.16Ga0.84As." Journal of The Electrochemical Society, vol. 129, pp. 2380-2382, 1982

3. DeSalvo, Gregory C., Wen F. Tseng, and James Comas. "Etch rates and selectivities of citric acid/hydrogen peroxide on GaAs, Al0. 3Ga0. 7As, In0. 2Ga0. 8As, In0. 53Ga0. 47As, In0. 52Al0. 48As, and InP." *Journal of The Electrochemical Society* 139, no. 3 (1992): 831-835.

4. J. Novak, M. Morvic, J. Betko, A. Förster, and P. Kordoš, "Wet chemical separation of low-temperature GaAs layers from their GaAs substrates." Materials Science and Engineering, vol. B 40, pp. 58-62, 1996.

5. H. J. Yeh, and J. S. Smith, "Integration of GaAs vertical-cavity surface emitting laser on Si by substrate removal." Applied Physics Letters, vol. 64, pp.1466-1468, 1994.

6. M. Konagai, M. Sugimoto, and K. Takahashi, "High efficiency GaAs thin film solar cells by peeled film technology." Journal of Crystal Growth, vol. 45, pp. 277-280, 1978

7. E. Yablonovitch, T. Gmitter, J. P. Harbison, and R. Bhat, "Extreme selectivity in the lift-off of epitaxial GaAs films." Applied Physics Letters, vol. 51, pp. 2222-2224, 1987.

8. Zheng, L., S. K. Haywood, N. J. Mason, and G. Verschoor. "p-GaSb/n-GaAs heterojunction diodes for TPV and solar cell applications." IEE Proceedings-Optoelectronics 147, no. 3 (2000): 205-208.

9. Wang, C. A., R. K. Huang, D. A. Shiau, M. K. Connors, P. G. Murphy, P. W. O'Brien, A. C. Anderson, D. M. DePoy, G. Nichols, and M. N. Palmisiano. "Monolithically series-interconnected GaInAsSb/AlGaAsSb/GaSb thermophotovoltaic devices with an internal backsurface reflector formed by wafer bonding." Applied physics letters 83, no. 7 (2003): 1286-1288

10. Kim, Jung Min, Partha S. Dutta, Eric Brown, Jose M. Borrego, and Paul Greiff. "Wafer-scale processing technology for monolithically integrated GaSb thermophotovoltaic device array on semi-insulating GaAs substrate." Semiconductor Science and Technology 28, no. 6 (2013): 065002

11. Qian, W., M. Skowronski, R. Kaspi, M. De Graef, and V. P. Dravid. "Nucleation of misfit and threading dislocations during epitaxial growth of GaSb on GaAs (001) substrates." *Journal of applied physics* 81, no. 11 (1997): 7268-7272.

12. Xin, Y-C., L. G. Vaughn, L. R. Dawson, A. Stintz, Y. Lin, L. F. Lester, and D. L. Huffaker. "InAs quantum-dot GaAs-based lasers grown on AlGaAsSb metamorphic buffers." *Journal of applied physics* 94, no. 3 (2003): 2133-2135.

13. Huang, S. H., G. Balakrishnan, A. Khoshakhlagh, A. Jallipalli, L. R. Dawson, and D. L. Huffaker. "Strain relief by periodic misfit arrays for low defect density GaSb on GaAs." *Applied physics letters* 88, no. 13 (2006): 131911.

14. J. W. Matthews and A. E. Blakeslee, *"Defects in epitaxial multilayers: I. Misfit dislocations"*, J. Cryst. Growth. **27**, 118 (1974).

15. J. W Matthews, A. E. Blakeslee, and S. Mader, *"Use of misfit strain to remove dislocations from epitaxial thin films,"* Thin Solid Films **33**, 253 (1976).

16. R. People and J. C. Bean, *"Calculation of critical layer thickness versus lattice mismatch for GexSi1–x/Si strained-layer heterostructures"*, Appl. Phys. Lett. **47**, 322 (1985).

17. Carter-Coman, Carrie, Robert Bicknell-Tassius, Rudolph G. Benz, April S. Brown, and Nan Marie Jokerst. "Analysis of GaAs substrate removal etching with citric acid: H 2 O 2 and NH 4 OH: H 2 O 2 for application to compliant substrates." *Journal of the Electrochemical Society* 144, no. 2 (1997): L29-L31.

18. Jallipalli, A., G. Balakrishnan, S. H. Huang, T. J. Rotter, K. Nunna, B. L. Liang, L. R. Dawson, and D. L. Huffaker. "Structural analysis of highly relaxed GaSb grown on GaAs substrates with periodic interfacial array of 90 misfit dislocations." *Nanoscale research letters* 4, no. 12 (2009): 1458.

19. DeSalvo, Gregory C., Ron Kaspi, and Christopher A. Bozada. "Citric Acid Etching of GaAs1− x Sb x, Al0. 5Ga0. 5Sb, and InAs for Heterostructure Device Fabrication." *Journal of The Electrochemical Society* 141, no. 12 (1994): 3526-3531.

20. Hageman, P. R., G. J. Bauhuis, A. Van Geelen, P. C. Van Rijsingen, J. J. Schermer, and L. J. Giling. "Large area, thin film epitaxial lift off III/V solar cells." In *Photovoltaic Specialists Conference, 1996., Conference Record of the Twenty Fifth IEEE*, pp. 57-60. IEEE, 1996.

21. B. C. Juang, R. B. Laghumavarapu, B. J. Foggo, P. J. Simmonds, A. Lin, B. Liang, and D. L. Huffaker, "GaSb thermophotovoltaic cells grown on GaAs by molecular beam epitaxy using interfacial misfit arrays," *Applied Physics Letters,* vol. 106, pp 111101, 2015.

22. D. DeMeo, C. Shemelya, C. Downs, A. Licht, E. S. Magden, T. Rotter, C. Dhital, S. Wilson, G. Balakrishnan, and T. E. Vandervelde, "GaSb Thermophotovoltaic Cells Grown on GaAs Substrate Using the Interfacial Misfit Array Method," *Journal of Electronic Materials,* vol. 43, pp. 902-908, 2014

23. Lee, Kyusang, Jeramy D. Zimmerman, Yifan Zhang, and Stephen R. Forrest. "Epitaxial lift-off of GaAs thin-film solar cells followed by substrate reuse." In *Photovoltaic Specialists Conference (PVSC), 2012 38th IEEE*, pp. 001698-001700. IEEE, 2012.

Chapter 4: Optimization Techniques to Further Reduce Threading Dislocations in Metamorphic GaSb TPV Cells Grown on GaAs Substrates by IMF Growth Mode

4.1 Introduction

As explained in the previous chapter, the strain energy produced by the 7.78% lattice-mismatch between GaSb and GaAs is relieved by the formation of 90º and 60º misfit dislocations. The 90º misfit dislocations propagate laterally along the GaSb/GaAs interface, and the 60º misfit dislocations propagate into the GaSb bulk layer [1]. The IMF growth mode allows for instantaneous strain relief at the heteroepitaxial interface through the formation periodic arrays of 90º misfit dislocations at the interface, and it reduces the formation of 60^0 misfit dislocations that causes threading dislocations [2-3]. However, as shown in the previous chapter, the residual threading dislocations severely affect the performance of the metamorphic GaSb TPV cells. Hence, two techniques have been investigated to further reduce threading dislocations that propagate to the p-n junctions. One technique focuses on further minimizing the formation of 60^0 misfit dislocations, and the other technique focuses on blocking the threading dislocations propagating into the p-n junction of the devices.

4.2 Optimization of Growth Temperature

The growth temperature has been shown to be a strong factor in determining which type of misfit dislocation is formed [4-5]. Kim *et al.* showed that the lattice mismatch strain between GaSb and GaAs is mainly accommodated by 90º misfit dislocations if GaSb is grown at 520 ºC and by 60^0 misfit dislocations if grown at 560 ºC [5]. The metamorphic GaSb devices in the previous chapter were grown at 500º C using the IMF growth technique. However, the formation of 60^0

misfit dislocations is still present as threading dislocation density (TDD) of samples is in the low 10^8 defects per cm^2. Therefore, it is important to find the optimal growth temperature.

For this study, 2 μm thick GaSb epitaxial layers are grown at 6 different temperatures ranging from 350ºC to 540ºC. After growth, the TDD in each sample is calculated using cross-section transmission electron microscopy (XTEM), plan-view transmission electron microscopy (PV TEM), and an X-Ray diffraction (XRD) <004> rocking curve analysis.

4.2.1 Growth Details

The samples are grown on GaAs (001) substrates in a VG V80 molecular beam epitaxy (MBE) reactor. The substrate temperature is measured using an optical pyrometer. The growth procedure is the same as described in the previous chapter. The oxide on the substrates is desorbed at 620^0C; a 200 nm GaAs smoothing layer is grown at 580^0C, following this, the As cracker is valved off to let arsenic desorb from the surface. Once the reflection high-energy electron diffraction (RHEED) pattern transforms from a 2 x 4 pattern to a 4 x 2 pattern, the sample is cool down to the growth temperature under Sb overpressure. As soon as the Sb flux reaches the Ga-rich surface, a 2 x 8 RHEED pattern is observed. The interaction of Sb with the Ga-rich surface is critical to the formation of the IMF array [3]. Within the first few monolayers of GaSb, the RHEED pattern turns into a 1 x 3 reconstruction. A constant V/III ratio of 5 is maintained between Sb and Ga across all samples as measured by an ionization gauge (this ratio is the optimized ratio for growing GaSb at 500 ºC). Also, the GaSb growth rate (calibrated by RHEED oscillations) is kept constant at 0.3ML/sec. The growth sequence is summarized by the diagram provided in Fig 4.1.
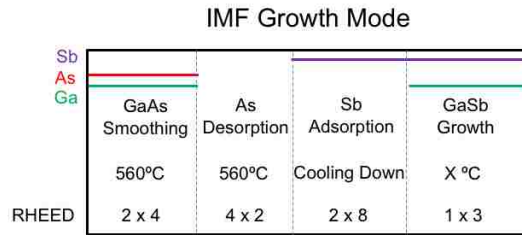
FIG. 4.1 SCHEMATIC OF GROWTH SEQUENCE FOR IMF FORMATION

4.2.2 Calculation of Threading Dislocation Density

The TDD can be calculated from XTEM images by adding the length of the dislocation lines and then dividing the total length by the volume of the sample. The volume is computed by multiplying the area of the image times the thickness of the TEM specimen. Fig 4.2 shows an example of how TDD is calculated from an XTEM image. The sum of the length of the dislocations lines is 2.685 µm. The area of the GaSb epitaxial layer in the XTEM image is 11.95 µm^2, and the thickness of the TEM sample is 0.150 µm. Hence, the TDD is 1.5 x 10^8 defects/cm^2.
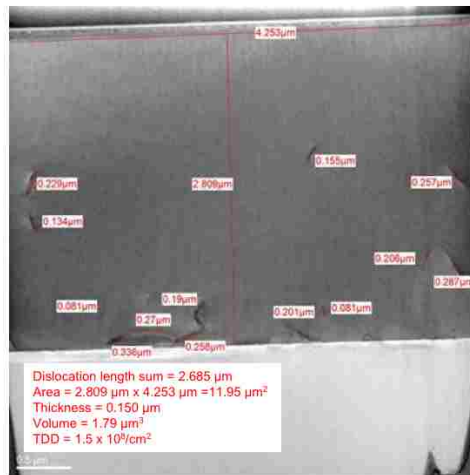
FIG. 4.2 TDD CALCULATION FROM XTEM IMAGE

The bright-field XTEM images along [110] direction of the 2µm thick IMF-grown GaSb epitaxial layers at different growth temperatures (420, 460, 500 and 540 °C) are shown in Fig 4.3. These XTEM images are used to calculate the TDD of the samples. Although not obvious from

87

the XTEM images, the TDD decreases as growth temperature decreases. The TDD is estimated to be 1.1×10^9 defects/cm^2 for the sample grown at 540 ºC and 7×10^7 defects/cm^2 for the sample grown at 420 ºC. The sample grown at 500 ºC (temperature used to grow the devices in the previous chapter) shows a TDD of 4.1×10^8 defects/cm^2.
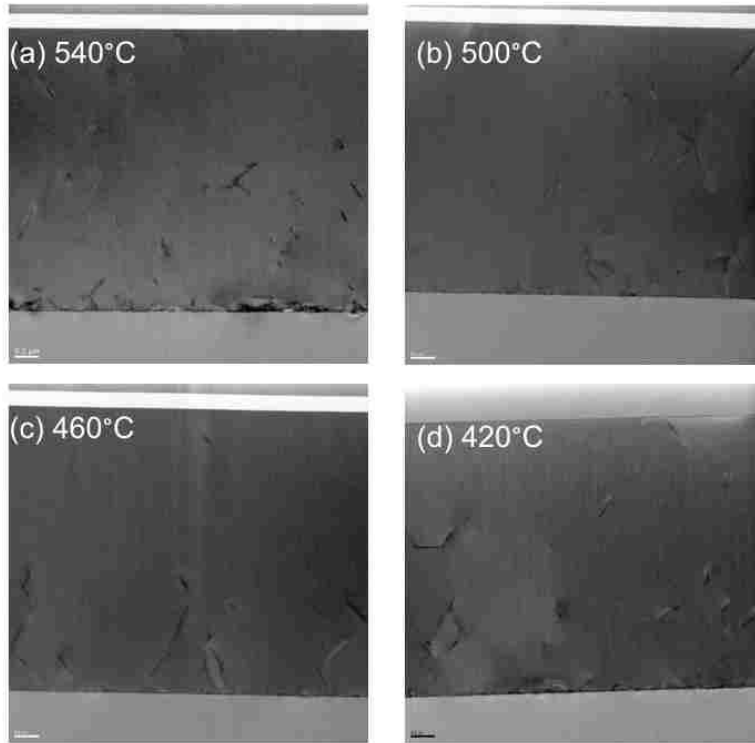
FIG. 4.3 XTEM IMAGES ALONG [110] DIRECTION OF THE 2μM THICK GaSb EPITAXIAL LAYERS GROWN AT (A) 540 ºC, (B) 500 ºC, (C) 460 ºC, (D) 420 ºC.

To verify the TDD obtained from XTEM, PV TEM images of the GaSb surfaces grown at the different temperatures are also analyzed. Fig 4.4 shows the PV TEM images of the samples grown at 420, 460, 500 and 540 ºC. The PV TEM images clearly show that TDD decreases with decreasing temperature. This is the same trend observed from the XTEM images. The TDD from the PV TEM images is calculated by directly counting the number of dislocations and dividing this number by the analyzed area. The TDD from PV TEM images is estimated to be

7.0×10^8 defects/cm^2 for the sample grown at 540 ºC and 1.3×10^8 defects/cm^2 for the sample grown at 420 ºC.
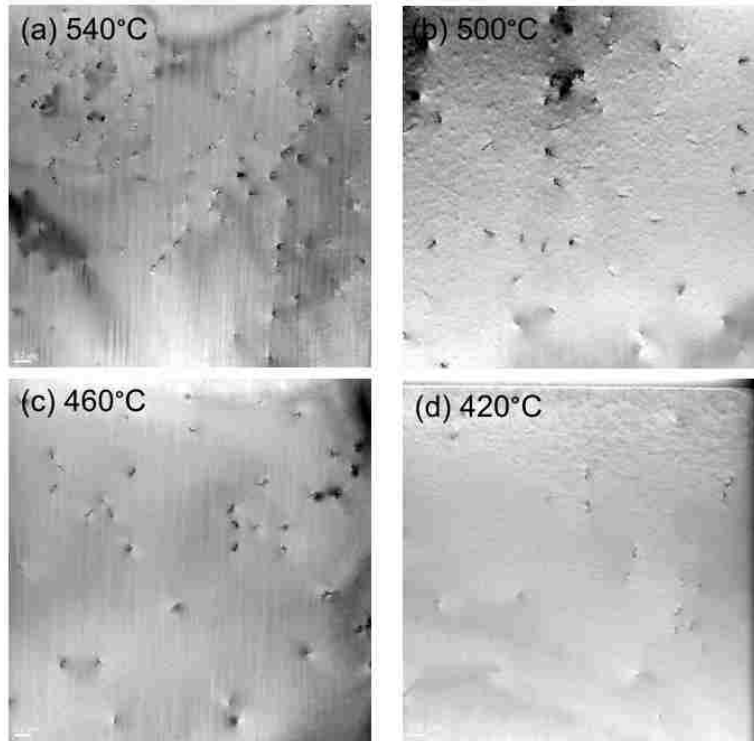
FIG. 4.4 PV TEM IMAGES OF GASB EPITAXIAL SURFACES GROWN AT (A) 540 ºC, (B) 500 ºC, (C) 460 ºC, (D) 420 ºC.

A third way to study TDD in the samples is by doing a comprehensive XRD rocking curve analysis. The TDD can be calculated from the FWHM of ω rocking curves measured at the maximum of the substrate and epitaxial layer diffraction peaks [6]. From the theory of Gay, Hirsch, and Kelly [6], the density of threading dislocation is related to the measured FWHM (rad) rocking curve by the equation

$$N_D = \frac{(FWHM)^2}{4.36 \times b^2} \qquad\qquad (2)$$

where the b is the length of the typical dislocation Burgers vector if the rocking curve width is just determined by the skew dislocations. For GaAs-related compounds with 60º dislocation loops, b could be assumed to be equal to 4.0Å. This theory predicts that the skew dislocations

should result in a Gaussian broadening of the rocking curve. Using equation (2), the threading

dislocation density for the sample grown at 540 ºC is found to be 1.1×10^9 defects/cm^2 while the

one grown at 420^0C has a TDD of 5.2×10^7 defects/cm^2. Once again, the trend is the same as

determined by TEM analysis. Hence, XRD rocking curve analysis is an excellent technique to

measure dislocation densities in a reduced amount of time.
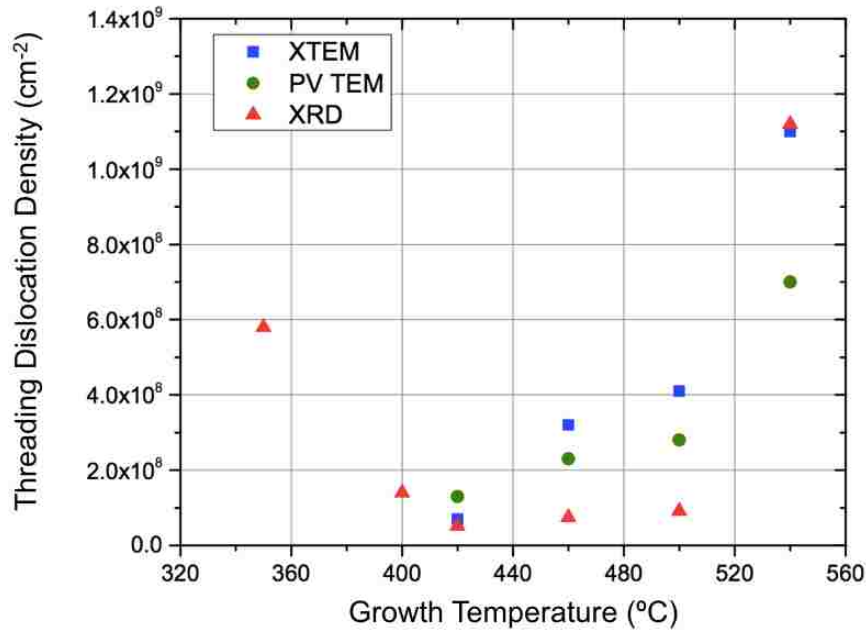
FIG. 4.5 THREADING DISLOCATION DENSITY (TDD) VERSUS GROWTH TEMPERATURE. TDD IS CALCULATED FROM
XTEM, PLAIN PV TEM, AND XRD

Fig 4.5 shows a graph summarizing the TDD results from XTEM, PV TEM, and XRD at the

different growth temperatures. To know if the TDD will keep decreasing with decreasing

temperature, two more samples were grown at colder temperatures (400 ºC and 350 ºC). The

TDD for this samples is calculated from XRD only as it gives accurate measurements and is not

as time consuming as TEM. Growing colder starts to increase the number of threading

dislocations as shown by the graph in Fig 4.5. The TDD at 350 ºC goes back up to 5.8×10^8

defects/cm^2. The optimal growth temperature is found to be 420 ºC. However, the residual TDD

at this temperature is still high for GaSb TPV devices. Hence, in the next section, a technique to block the threading dislocations is investigated.

4.3 AlSb Blocking Layers

Besides the IMF growth mode, several other buffer techniques had been investigated to reduce the dislocation density in GaSb films grown on GaAs substrates. Qian *et al.* tried to use buffer layers such as InGaSb, AlSb, and strained layer superlattice (SLS) AlSb/GaSb before growing GaSb [7]. The InGaSb and AlSb buffer layers did not make a difference, but the SLS buffer reduced the TDD from 7×10^8 cm^{-2} to 5×10^7 cm^{-2}. More studies on AlSb buffers followed, and it was concluded that thin (few nm) AlSb layers grown at low temperatures improves the quality of GaSb [8-10]. However, no TDD was reported in these studies. Compositionally graded buffers have also been used and again surface morphology of GaSb surface is stated to be improved but not TDD is reported [11-12].

A more promising technique is to use dislocations filter layers or blocking layers after the buffer layers. Fastenau *et al.* tried to grow InAsSb/AlAsSb n-B-n photodetectors on GaAs substrates using a thick (~4 μm) single-step GaSb buffers, a 1 μm thick compositional graded GaAs$_x$Sb$_{1-x}$ followed by a 3 μm GaSb buffer, and by using a AlAsSb/AlAsSb tensile strained (TS) SLS dislocation filter layer after a 1 μm thick GaSb metamorphic buffer layer [11]. The nBn photodetectors grown on the TS SLS buffer showed the best performance.

Hence, to further reduce TDD in metamorphic GaSb TPV cells, single-step GaSb buffers followed by AlSb blocking layers had been investigated. AlSb is a good option as it can be incorporated into the GaSb cell structure as a back-surface reflector layer. For this study, three samples were grown with 250-nm-thick AlSb blocking layers and GaSb buffer layer with different thicknesses (100, 250, and 500 nm).

The GaSb buffer layers are grown by IMF growth mode at the optimized growth temperature of 420 ºC as described in the previous section. However, the AlSb blocking layers and the GaSb epitaxial layers above them are grown at 500 ºC. If the structure is fully grown at 420 ºC, the surface morphology of the sample is very rough and full of defects as shown in the scanning electron microscope (SEM) image in Fig 4.6. XTEM across one of these square defects indicates that the defect originates at the AlSb layer as shown in Fig 4.7. This means that the growth conditions for AlSb are not optimal. AlSb needs to be grown at higher temperatures. Hence, for the next set of samples, the substrate temperature was slowly ramped up from 420 ºC to 500 º C right before growing the AlSb layer. At this temperature, the square defects are not observed anymore.
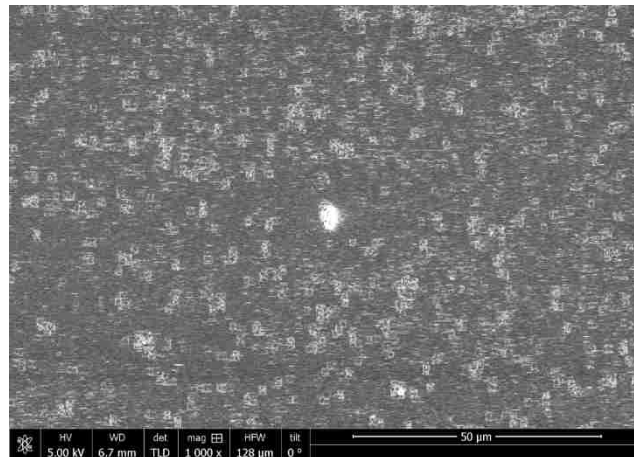
FIG. 4.6 SEM IMAGE OF GASB SURFACE MORPHOLOGY OF A SAMPLE GROWN WITH LOW TEMPERATURE ALSB DISLOCATION FILTER LAYER
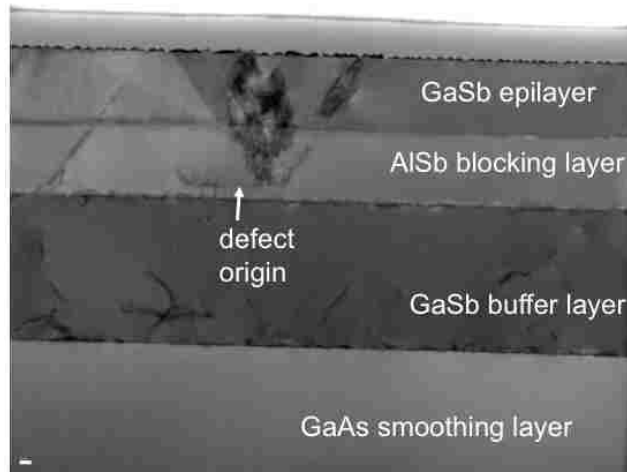
FIG. 4.7 XTEM IMAGE OF A SQUARE DEFECT IN METAMORPHIC GaSb EPITAXIAL LAYERS GROWN AT 420 °C ON A GaAs SUBSTRATES WITH AN AlSb DISLOCATION FILTER LAYER AND A GaSb BUFFER LAYER.

Fig. 4.8 shows the schematic of the samples grown along with corresponding cross-sectional and plan-view TEM images. Sample I is the best sample from the previous optimization technique which resulted in a TDD of 1.3 x 10^8 defects/cm^2 as calculated from PV TEM. The other three samples have the AlSb blocking layers. Sample II has a 100 nm GaSb buffer layer prior to the 250 nm AlSb blocking layer (BL). From PV TEM, its TDD is calculated to be 1.1 x 10^8 defects/cm^2 which does not differ much from sample I (without BL). Sample III has a 250 nm GaSb buffer layer and a TDD of 8.9 x 10^7 defects/cm^2. Finally, Sample IV, with the thicker GaSb buffer (500 nm thick), gives the lowest TDD of 3.6 x 10^7 defects/cm^2. Qian *et al*. reported 14 μm thick metamorphic GaSb layers on GaAs substrates with TDD of 2 x 10^7 defects/cm^2 [7]. Hence, having the same range of TDD with only 500 nm of GaSb buffer is a great improvement.

93
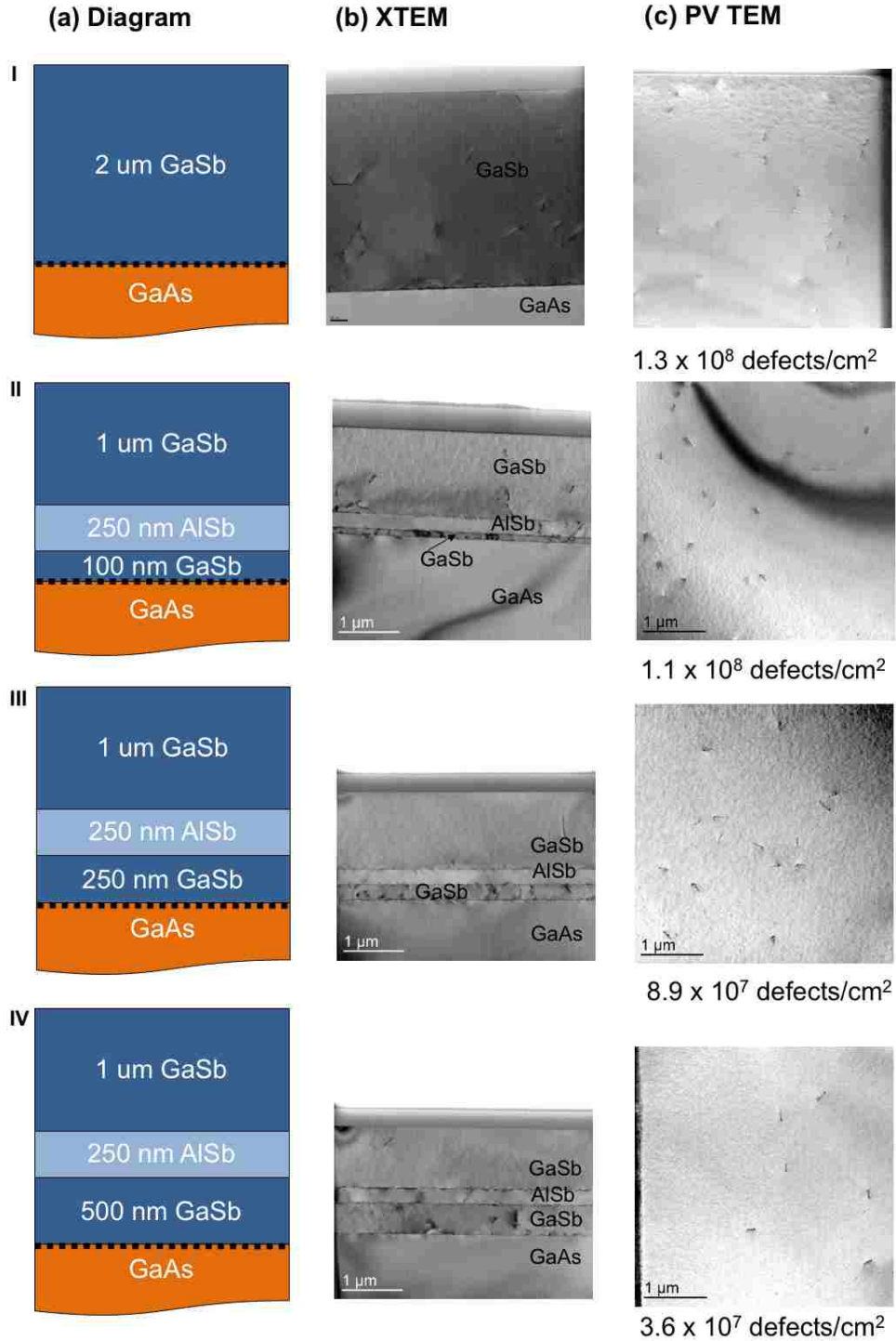
FIG. 4.8 (A) SCHEMATIC OF SAMPLES GROWN TO SEE THE EFFECT OF ALSB LAYERS IN THE FILTERING OF THREADING DISLOCATIONS (B) XTEM AND (C) PV TEM IMAGES OF THE CORRESPONDING SAMPLES.

4.4 Improvement of Open-Circuit Voltage

Now that the TDD has been reduced by almost an order magnitude, it is important to know how much impact reducing the TDD is going have on the performance of the metamorphic GaSb TPV cells. To investigate this impact, the three structures shown in Fig 4.9 are grown. The first sample is a lattice matched GaSb TPV cell grown on a GaSb substrate to use as a control sample (LM sample). The other two samples are metamorphic GaSb solar cells grown on GaAs substrates by inducing arrays of 90° interfacial misfit dislocations at the GaSb/GaAs interface. One sample has the AlSb blocking layer, and other does not.

The p-on-n GaSb solar cell structure consists of a 50 nm thick p-type (5×10^{18} cm^{-3}) GaSb contact layer, a 500 nm p-type (5×10^{17} cm^{-3}) GaSb emitter layer, a 2000 nm thick n-type (4×10^{17} cm^{-3}) base layer, and a 200 nm thick n-type (5×10^{18} cm^{-3}) GaSb contact layer. The IMF sample with the AlSb blocking layer (IMF BL sample) has a 500 nm GaSb layer after the GaAs buffer layer and then it is followed by a 250 nm AlSb layer and then the GaSb solar cell layers. For the regular IMF sample, the cell's layers are grown after the GaAs buffer layer. The growth conditions for the IMF samples are established as described by the optimization techniques above.
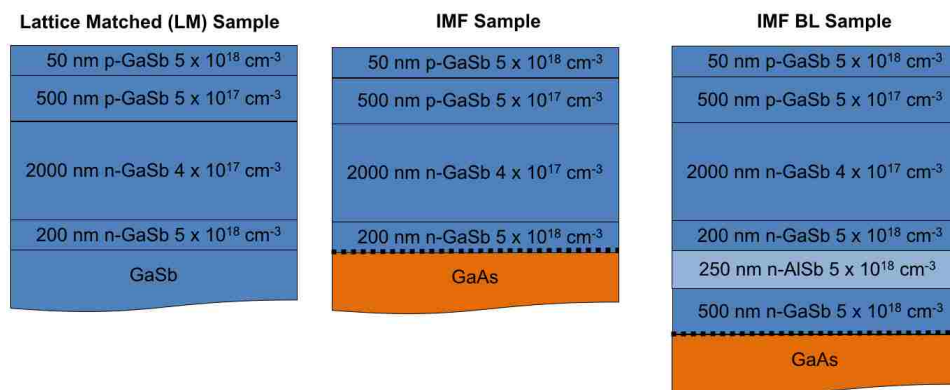
FIG. 4.9 SCHEMATIC OF GASB TPV CELL STRUCTURES GROWN TO COMPARE THE EFFECT OF ALSB BLOCKING LAYERS

Device fabrication is performed using standard photolithography techniques. Metals are deposited via e-beam evaporation. For the top grid, p-type Ti/Pt/Au ohmic contacts are deposited. For the bottom contacts, a metal sequence of Ni/Ge/Au/Pt/Au is deposited if the material is n-GaSb and Ge/Au/Ni/Au if it is n-GaAs. To make the n-contacts ohmic, the n-GaSb contacts are annealed at 290°C for 45 seconds, and the n-GaAs contacts are annealed at 380°C for 60 seconds. The devices are isolated by etching the mesas below the p-n junction using an inductively coupled plasma reactor with BCl_3 gas.

Fig. 4.10 shows the dark current density – voltage (J-V) characteristics of the three samples. It can clearly be seen that the reverse-bias leakage current of the IMF BL device has been reduced significantly in comparison to the IMF device without BL. At -1V, the dark current is -8 mA/cm^2 for the LM sample, -48 mA/cm^2 for the IMF BL sample, and -210 mA/cm^2 for the IMF sample. The one order of magnitude reduction in TDD has reduced the leakage current by about 77 %.
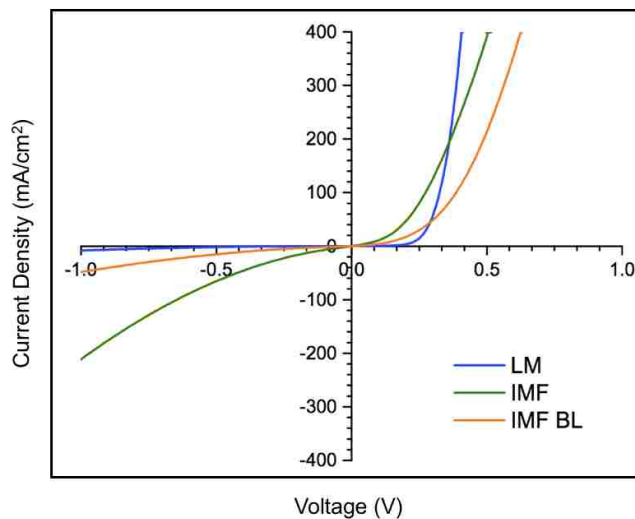
FIG. 4.10 DARK J-V CHARACTERISTICS OF GASB DIODES

Fig. 4.11 shows the J-V characteristics of the three samples measured under air mass zero (AM0) illumination. The 0.5 cm x 0.5 cm control cell exhibits an open-circuit voltage (V_{OC}) of 0.25 V, a short-circuit current density (J_{SC}) of 28.72 mA/cm^2, a fill factor (FF) of 57.25%, and an efficiency (η) of 2.98%. The same size IMF cell shows a V_{OC} of 0.13 V, a J_{SC} of 22.93 mA/cm^2, a FF of 33.58%, and a η of 0.71%. The IMF BL cell shows a V_{OC} of 0.16 V, a J_{SC} of 23.91 mA/cm^2, a FF of 34.53%, and a η of 0.95%. Table 4.1 has a summary of these parameters. Comparing the IMF-based cells, it is observed that the IMF BL sample has a higher V_{OC} than the IMF sample. A higher V_{OC} means that the crystal quality of the IMF BL sample has increased and that indeed the threading dislocation density in the sample has been reduced. Also, the J_{SC} has increased slightly. This increase in J_{SC} can be observed in the external quantum efficiency (EQE) measurements shown in Fig. 4.12. Throughout the wavelength range, the EQE curve for the IMF BL sample is higher than the IMF sample. Hence, the IMF BL sample was expected to have a higher J_{SC} than the IMF sample. The short circuit currents calculated from EQE measurements are 29.25 mA/cm^2 for the LM sample, 20.94 mA/cm^2 for the IMF BL sample, and 18.76 mA/cm^2 for the IMF sample.
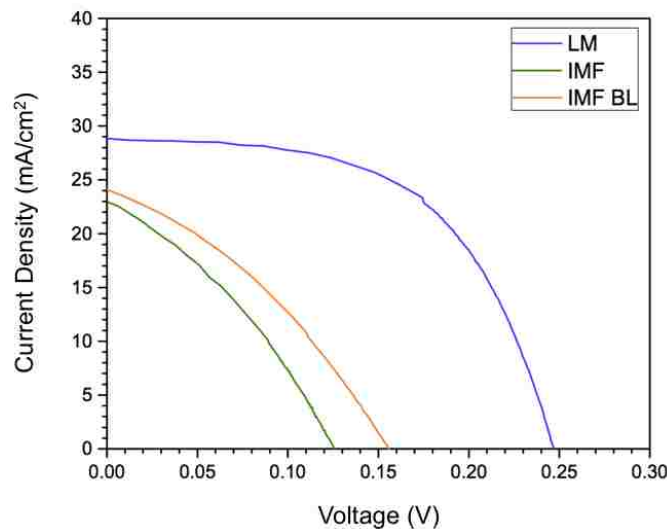
FIG. 4.11 J-V CHARACTERISTIC OF LATTICE-MATCHED AND METAMORPHIC GASB TPV CELLS UNDER AIR MASS ZERO ILLUMINATION

TABLE 4.1. Summary of GaSb cell's parameters

	LM	IMF	IMF BL
J_{sc} (mA/cm^2)	28.72	22.93	23.91
V_{oc} (V)	0.25	0.13	0.16
FF (%)	57.25	33.58	34.53
η (%)	2.98	0.71	0.95
R_s (Ωcm^2)	6	12	22
R_s (Ωcm^2)	100	44	47
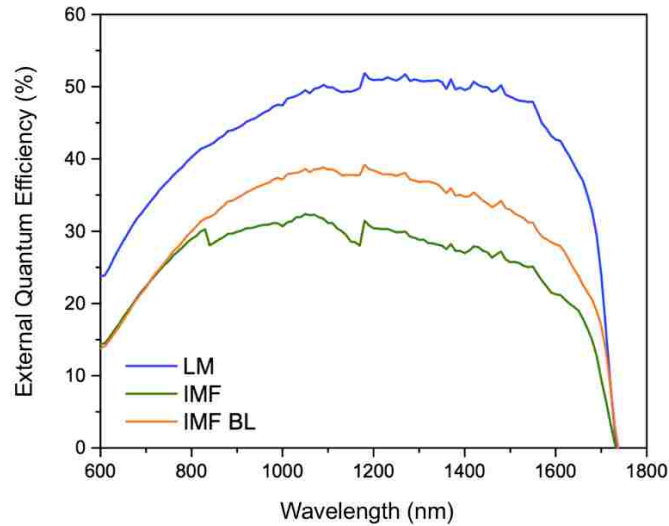
FIG. 4.12 EXTERNAL QUANTUM EFFICIENCY OF GASB TPV CELLS

4.5 Conclusion

In conclusion, we have shown that the performance of metamorphic GaSb solar cells grown on GaAs substrates by IMF technique can be improved by optimizing the growth temperature and by using AlSb layers that block the propagation of treading dislocations to the p-n junction. The leakage current has been reduced by 77 % and the V_{oc} has been increased by 23 %. These two parameters are dependent on the crystal quality of the material. Hence, the improvement of these parameters verifies that threading dislocation density in the sample with the AlSb blocking layer has been reduced.

References

1. Qian, W., M. Skowronski, R. Kaspi, M. De Graef, and V. P. Dravid. "Nucleation of misfit and threading dislocations during epitaxial growth of GaSb on GaAs (001) substrates." *Journal of applied physics* 81, no. 11 (1997): 7268-7272.

2. Huang, S. H., G. Balakrishnan, A. Khoshakhlagh, A. Jallipalli, L. R. Dawson, and D. L. Huffaker. "Strain relief by periodic misfit arrays for low defect density GaSb on GaAs." *Applied physics letters* 88, no. 13 (2006): 131911.

3. Huang, Shenghong, Ganesh Balakrishnan, and Diana L. Huffaker. "Interfacial misfit array formation for GaSb growth on GaAs." *Journal of Applied Physics* 105, no. 10 (2009): 103104.

4. Kang, J. M., M. Nouaoura, L. Lassabatere, and A. Rocher. "Accommodation of lattice mismatch and threading of dislocations in GaSb films grown at different temperatures on GaAs (001)." *Journal of crystal growth* 143, no. 3-4 (1994): 115-123.

5. Kim, Joon-Hyung, Tae-Yeon Seong, N. J. Mason, and P. J. Walker. "Morphology and defect structures of GaSb islands on GaAs grown by metalorganic vapor phase epitaxy." *Journal of electronic materials* 27, no. 5 (1998): 466.

6. Ayers, JE. "The measurement of threading dislocation densities in semiconductor crystals by X-ray diffraction." *Journal of Crystal Growth* 135.1 (1994): 71-77.

7. Qian, W., M. Skowronski, and R. Kaspi. "Dislocation density reduction in GaSb films grown on GaAs substrates by molecular beam epitaxy." *Journal of the Electrochemical Society* 144, no. 4 (1997): 1430-1434.

8. Kim, H. S., Y. K. Noh, M. D. Kim, Y. J. Kwon, J. E. Oh, Y. H. Kim, J. Y. Lee, S. G. Kim, and K. S. Chung. "Dependence of the AlSb buffers on GaSb/GaAs (001) heterostructures." *Journal of Crystal Growth* 301 (2007): 230-234.

9. Zhi-Qiang, Zhou, Xu Ying-Qiang, Hao Rui-Ting, Tang Bao, Ren Zheng-Wei, and Niu Zhi-Chuan. "Molecular Beam Epitaxy of GaSb on GaAs Substrates with AlSb Buffer Layers." *Chinese Physics Letters* 26, no. 1 (2009): 018101.

10. Ripalda, J. M., Ana M. Sanchez, A. G. Taboada, A. Rivera, B. Alén, Y. González, L. González, F. Briones, T. J. Rotter, and Geetha Balakrishnan. "Relaxation dynamics and residual strain in metamorphic AlSb on GaAs." *Applied Physics Letters* 100, no. 1 (2012): 012103.

11. Fastenau, Joel M., Dmitri Lubyshev, Yueming Qiu, Amy WK Liu, Edwin J. Koerperick, Jon T. Olesberg, and Dennis Norton Jr. "MBE growth of GaSb-based photodetectors on 6-inch diameter GaAs substrates via select buffers." *Journal of Vacuum Science & Technology B, Nanotechnology and Microelectronics: Materials, Processing, Measurement, and Phenomena* 31, no. 3 (2013): 03C106.

12. Yu, Hai-Long, Hao-Yue Wu, Hai-Jun Zhu, Guo-Feng Song, and Yun Xu. "Molecular Beam Epitaxy of GaSb on GaAs Substrates with Compositionally Graded LT-GaAs x Sb1-x Buffer Layers." *Chinese Physics Letters* 34, no. 1 (2017): 018101.

Chapter 5: InGaAs Thin Film Devices

5.1 Introduction

The bandgap of InGaAs can be varied from 1.42 eV (GaAs) to 0.36 eV (InAs) by varying the

In/Ga composition ratio. InGaAs with a bandgap of 0.75 eV and narrower is of great interest for

TPV applications, since the narrow gap allows for the heat sources temperature to be lower. The

0.75 eV InGaAs cell, with a In/Ga ratio of 0.53/0.47, is lattice-matched to InP and has a cut-off

wavelength of 1.65 μm which corresponds to a temperature of 1758 K. It can be matched to the

emission spectra of a 2000 K blackbody source, which has an emission peak around 1.5 μm [1].

The 0.60 eV InGaAs cell is 1.1 % lattice-mismatched to InP and has a cut-off wavelength of 2.1

μm which corresponds to a temperature of 1380 K. It can be matched to the emission spectra of

a 1500 K blackbody source, which has an emission peak around 2 μm [1]. Avoiding high

temperature sources can be advantageous as problems with source heat management,

temperature limitation of the material, and cooling of the cell can be minimized [1]. However,

going to lower temperatures means that InGaAs will need to be more and more lattice-

mismatched. The growth of lattice-mismatched materials introduces threading dislocations and

other defects to the epitaxial layers that can be detrimental to the cells. Even though the crystal

quality of lattice-mismatched materials can improve significantly through different techniques

[2], InGaAs cells lattice-matched to InP are preferred for this thesis. Lattice-matched

InGaAs/InP is the ideal system to demonstrate the benefits of integrating narrow bandgap thin

film TPV devices to CVD diamond heat spreaders. There are no threading dislocations to

degrade the performance of the cells as there are in the GaSb/GaAs system. Finally, the etch

chemistry is well understood and highly selective unlike the etch chemistry in the GaSb/GaSb system.

5.2 Design and Growth of InGaAs TPV Structures

Thermophotovoltaic cells need to be designed to operate at high power densities. For this reason, most InGaAs TPV cells have an n-on-p polarity. Electrons have higher mobility than holes. The higher mobility of the majority carriers in a heavily-doped n-type emitter layer allows the emitter to have a low sheet resistance, which is important when high currents are going through the cell [3-4]. Also, higher electron mobility means longer diffusion lengths for the minority carriers in the p-type layer. The base of the cell is thicker than the emitter, and hence long diffusion lengths are important specially since the longer-wavelength photons are absorbed in the base layer [4].

TABLE 5.1. InGaAs TPV structure lattice matched to InP

Layer	Material	Thickness (μm)	Doping type & concentration (cm^{-3})
Contact	In$_{0.53}$Ga$_{0.47}$As	0.30	(n) 1 x 10^{19}
Window	In$_{0.52}$Al$_{0.48}$As	0.05	(n) 3 x 10^{18}
Emitter	In$_{0.53}$Ga$_{0.47}$As	0.20	(n) 2 x 10^{18}
Base	In$_{0.53}$Ga$_{0.47}$As	2.50	(p) 2 x 10^{17}
BSF	In$_{0.52}$Al$_{0.48}$As	0.05	(p) 3 x 10^{18}
Contact	In$_{0.53}$Ga$_{0.47}$As	0.20	(p) 1 x 10^{19}
		p-type InP substrate	

The design of In$_{0.53}$Ga$_{0.47}$As/InP lattice-matched structures for TPV cells has been successfully developed by many groups. InGaAs cells were used for bottom junction cells in tandem solar cells before they were used for TPV applications. Wilt *et al*. reported the first study to incorporate lattice-matched InGaAs to TPV systems [5]. Two n-on-p structures were compared. One structure had a thin InP window layer, and the other had a thicker window layer. More recently, Emziane *et al*. used a modeling approach to optimize the thickness and doping

concentrations of the base and emitter [6]. The model predicted maximum efficiency with doping concentrations of 3 x 10^{17} cm^{-3} for the n-type emitter and 8 x 10^{16} cm^{-3} for the p-type base and with thicknesses of about 0.2 μm and 2.5 μm for the emitter and base, respectively [6]. The structure of the lattice-matched InGaAs cells used in this thesis is based on studies mentioned above. The structure summarized in table 5.1.
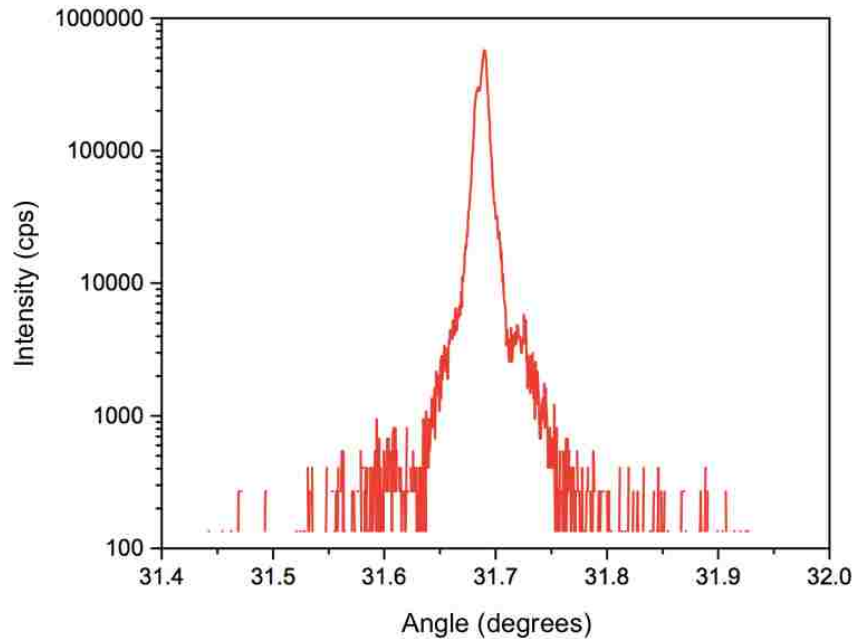
FIG. 5.1 $\Omega - 2\Theta$ (004) XRD SPECTRA OF InGaAs LATTICE-MATCHED TO InP

The samples used in this study are grown in a VG-V80 molecular beam epitaxy (MBE) reactor on epi-ready p-doped InP (001) substrates. The native oxide on the InP substrates is thermally desorbed at 550 ºC and is verified by a transformation in the Reflection High Energy Electron Diffraction (RHEED) pattern from a (2 x 1) to a (4 x 1) pattern. For oxide desorption, arsenic (As) is used as the surface stabilizing agent as the reactor used for the study does not have an elemental Phosphorous source. Following oxide desorption, the substrate temperature is brought down to 490 ºC and a 0.2 μm thick In$_{0.53}$Ga$_{0.47}$As is grown followed by a 0.05 μm p$^+$-

103

In$_{0.52}$Al$_{0.48}$As back surface field layer (BSF), a 2.50 µm p - In$_{0.53}$Ga$_{0.47}$As base, a 0.20 µm n - In$_{0.53}$Ga$_{0.47}$As emitter, a 0.05 µm n$^+$- In$_{0.52}$Al$_{0.48}$As window, and a 0.30 µm n^{++} - In$_{0.53}$Ga$_{0.47}$As contact layer as summarized in Table 5.1. The dopants used are Si for n-type and Te for p-type. The ω - 2θ (004) x-ray diffraction (XRD) spectra in Fig 5.1 shows that the grown structure is lattice-matched to the InP substrate.

5.3 Isolation of InGaAs TPV from InP Substrates

The isolation of epitaxial films from InP substrates can be achieved by two different techniques, shown in Fig 5.2. The first one is substrate removal where the InP substrate is completely dissolved in a selective etchant. The second one is epitaxial lift off (ELO) where a sacrificial layer, grown between the epitaxial layers of interest and the substrate, is etched laterally. In the following paragraphs, the two processes are described in more detail.
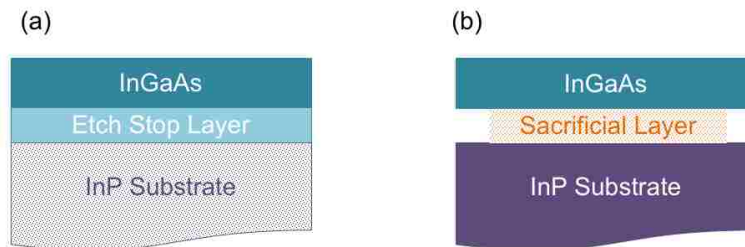
FIG 5.2. SCHEMATIC OF (A) SUBSTRATE REMOVAL AND (B) EPITAXIAL LIFT OFF TECHNIQUES

5.3.1 Substrate Removal of InP

In the substrate removal technique, the epitaxial layers are separated from their growth substrate by completely dissolving the substrate. The epitaxial layers are protected with an etch stop layer that is grown between the epitaxial layers of interest and the substrate as shown in Fig 5.2a. The solution used to dissolve the substrate must have a greater affinity for the substrate than for the etch stop layer. Subsequently, if the etch stop layer needs to be removed, a highly selective

etchant must be used to avoid damage to the material of interest.

Selective etchants for InP and its lattice matched compounds had been studied since the 1980's [7-11]. The first system studied was InGaAsP/InP. Phatak and Kelner reported that a solution of HCl:H_3PO_4 (1:1) selectively etches the InP substrate material without damaging the InGaAsP epitaxial layer [7]. Then, various solutions were tested to selectively etch InGaAs and InAlAs over InP [8, 11]. In summary, InP substrates can be etched away with either HCl or HCl:H_3PO_4. For the etch stop layer, either InGaAsP or InGaAs can be used. After substrate removal, the etch stop layer can be removed, if desired, using an etchant that has a high selectivity for the etch stop layer and not for the materials above it. In this thesis, an etch stop layer is not needed since the selectivity of HCl-based etchants for InP over InGaAs (the active material of the cell) is practically infinite [12].

5.3.2 Epitaxial Lift Off from InP Substrates

Schumacher *et al*. reported the first demonstration ELO from InP substrates using an AlAs sacrificial layer [13]. The device grown was an InGaAs p-i-n photodiode. After processing the photodiode, the AlAs layer was etched by submerging the wafer in 10% hydrofluoric (HF) acid, same as in GaAs systems. ELO was successful as HF does not affect InP or InGaAs. However, the dark current of the thin film photodiode degraded when compared to on-substrate diodes without the AlAs layer. This degradation was attributed to the induced dislocations by the 3.4 % lattice-mismatch between AlAs and InP although they did use buffer layers to accommodate for the lattice-mismatch.

Two decades later, Lee *et al*. used a 10 nm thick AlAs sacrificial layer to release InP Schottky-barrier solar cells from InP substrates [14]. In this paper, the focus was to see how many times the InP substrate could be reused. For this, InP protective layers and InGaAs etch

stops layers that were later removed were grown before and after the sacrificial layer. The performance of their thin film cells was comparable to their control cells, and no dislocation issues were mentioned. To avoid the problems that dislocations bring, Bailey *et al.* studied selective etchants to isolate InP epitaxial layers from InP substrates using a lattice matched InGaAs sacrificial layer [15]. The etchants with the highest selectivities were $HF:H_2O_2:H_2O$ (1:1:10) and $C_6H_8O_7:H_2O:H_2O_2$ (1:1:8).
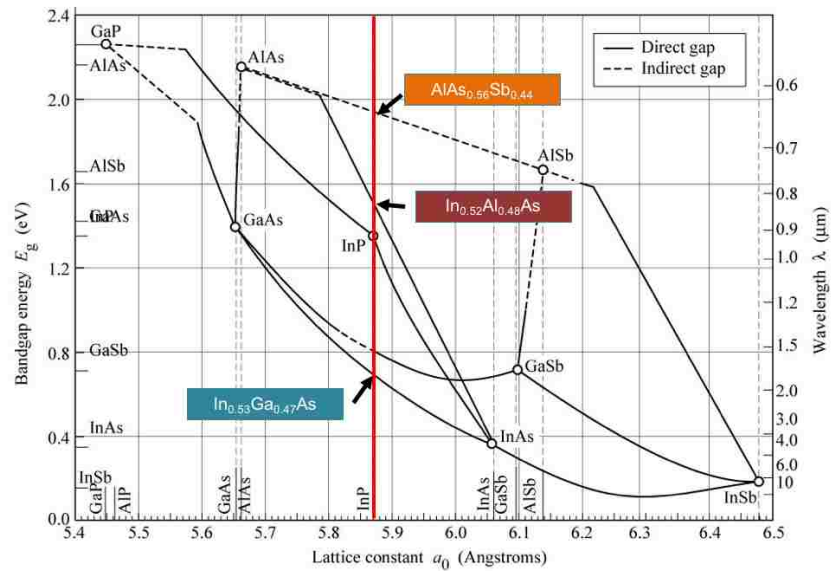
FIG 5.3. BANDGAP ENERGY AND LATTICE CONSTANT OF III-V SEMICONDUCTORS; HIGHLIGHTING MATERIALS LATTICE-MATCHED TO INP

However, for this thesis, InGaAs cannot be used as the sacrificial layer because it is the active material of the TPV cell and AlAs should be avoided since it is highly mismatched. Studying the bandgap energy versus lattice constant shown in Fig 5.3, it can be observed that there are two more materials besides InGaAs that are lattice matched to InP and could be used as a sacrificial layer for their high Al content. The first material is $In_{0.52}Al_{0.48}As$. However, this is used as a window and back surface reflector in the InGaAs TPV cell. Hence, it cannot be used as sacrificial layer, and it may even have to be protected from etchants such as HF. HF attacks

106

materials with high Al composition.   The second material is $AlAs_{0.56}Sb_{0.44}$. With 100% Al

content, $AlAs_{0.56}Sb_{0.44}$ can very well act as a sacrificial layer as it can be etched away with HF.

However, the growth of $AlAs_{0.56}Sb_{0.44}$ is complex, since it has two group V elements.   The

nonunity sticking coefficient of group V species makes the growth of mixed group V compounds

by MBE difficult [16].

5.4 Integration of Thin Film InGaAs TPV Cells to CVD Diamond
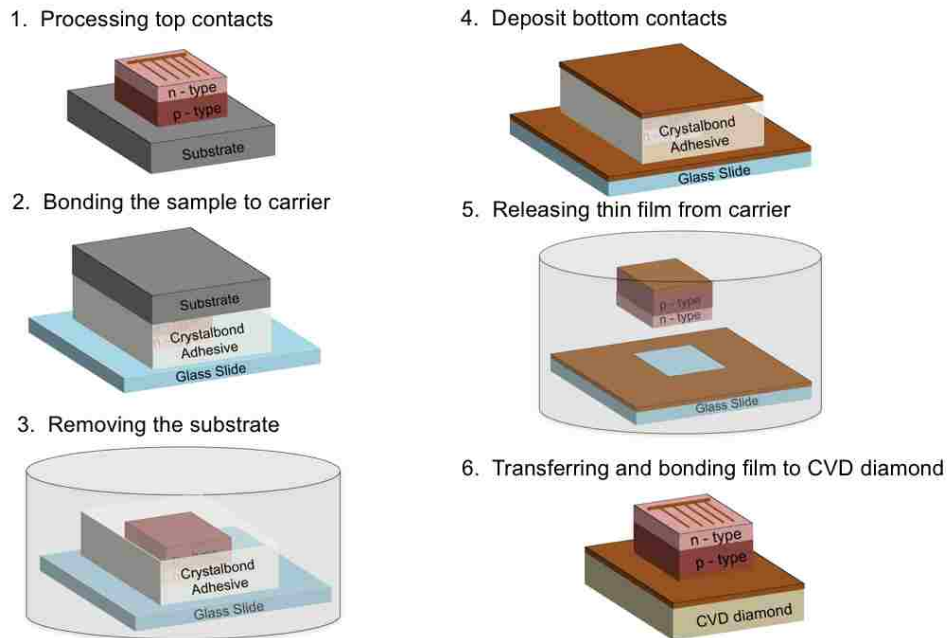
FIG 5.4. SCHEMATIC OF THE PROCESS FOR THE INTEGRATION OF THIN FILM INGAAS CELLS TO CVD DIAMOND HEAT SPREADERS

Fig 5.4 shows a schematic of the process used to integrate the thin film InGaAs cells to CVD

diamond heat spreaders. This is a top-side approach where the top contacts are processed while

the devices are still attached to the substrate followed by the removal of the substrate and

subsequently transferred onto the diamond. The top-side approach offers a convenient way to

process the top-contacts of the diode, but it challenges the transfer and bonding of the membrane

to the CVD diamond. Nonetheless, the integration is successful, and each step of the process is described in detail in the following paragraphs.

5.4.1 Processing Top Contacts

The first task is to figure out what are the best ohmic contacts for n-InGaAs. Therefore, a literature search is conducted. Lin el al gives an extensive review and experimental data on ohmic contacts for n- and p-type InGaAs [17]. In the study, it was determined that palladium-based contacts (Pd/Ti/Pt/Au) give the lowest contact resistances for both n- and p-type InGaAs. The lowest specific contact resistances achieved were $\rho = 3.2$ x 10^{-8} for n^+-InGaAs and $\rho = 1.9$ x 10^{-8} for p^+-InGaAs [17]. Also, Lin *et al.* recommended to prepare the InGaAs surface with an UV-ozone exposure followed by a treatment with buffer oxide etch solution (BOE) to minimize specific contact resistance [17]. Hence, for the InGaAs TPV cells in this study, Pd-based contacts are used along with the recommended treatment.

The top contacts are fabricated via standard photolithography and metal evaporation process. Before fabrication begins, the sample goes through a rigid cleaning process so it can be free of particles, organic residues, and native oxides. The wafer is rinsed with acetone, isopropanol, methanol, and deionized (DI) water and dried with nitrogen. Then, the sample is exposed to ultra-violet (UV) light in the mask aligner (as there is no UV-ozone) for 1 minute and then submerged in BOE for 2 minutes to remove the native oxides.

After patterning the sample with photoresist, the sample goes through a descumming process with oxygen plasma to remove excess photoresist and assure good adhesion of the metal. After the descumming process, the native oxide is etched with BOE for 2 min and rinsed with DI water for 15 s. Then, the samples are immediately loaded into the electron-beam evaporator chamber. Once a pressure of 2 x 10^{-6} Torr is achieved, Ti is evaporated for 2 min with the shutter close to

minimize oxygen residuals in the chamber [17]. This brings the chamber's pressure down to around 7 x 10^{-7} Torr. Next, Pd/Ti/Pt/Au metal layers are evaporated with thickness of 90 Å / 150 Å / 150 Å / 3000 Å. After lift-off, the contacts are annealed at 400 ºC for 60 s under N_2 atmosphere.
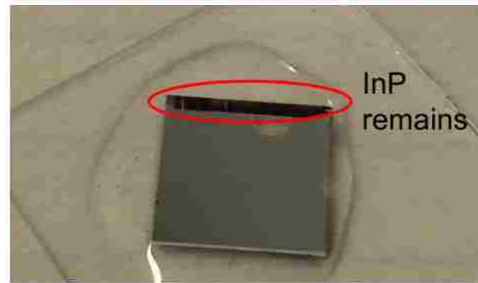

FIG 5.5. IMAGE OF INGAAS AFTER ETCHING AWAY THE INP SUBSTRATE

The last step in processing the top contacts is to do mesa isolation. Since only one cell can be placed in a 1 cm x 1 cm CVD diamond, the mesa isolation could be skipped if the cells are cleaved individually before the substrate is removed. However, it has been noticed that most of the time there is a residue of the substrate on the edges after substrate removal as shown in Fig 5.5. Hence, the mesa isolation is preferred as it allows for a clean back surface and detachment of various cells at a time. Therefore, the samples are patterned for mesa isolation and etched all the way down to the substrate using an inductively coupled plasma reactor with BCl_3 gas.

5.4.2 Bonding the Sample to the Carrier

Once the cells have the metal grid, the next step is to remove the substrate. However, a carrier is needed to keep the fragile thin film undamaged while the growth substrate is removed. For this, a glass slide is used. The sample is bonded to the glass with a crystalbond[TM] 509 adhesive. Crystalbond[TM] 509 was chosen because it is a temporary adhesive that can be easily dissolved in acetone, is resistant to most chemicals, and is vacuum compatible. The disadvantage is that it

melts at 121 ºC and while that is good for the bonding step is not favorable if the wafer needs to go through high temperature processes. Nonetheless, a small of amount of crystalbond^{TM} 509 is melted on a glass slide on a hot plate at a temperature of 120 ºC. Then, the sample is placed epitaxial-layer down onto the slide, and some pressure is applied to assure good bonding. After the sample is cool down, it is ready for substrate removal as it shown in Fig 5.6.

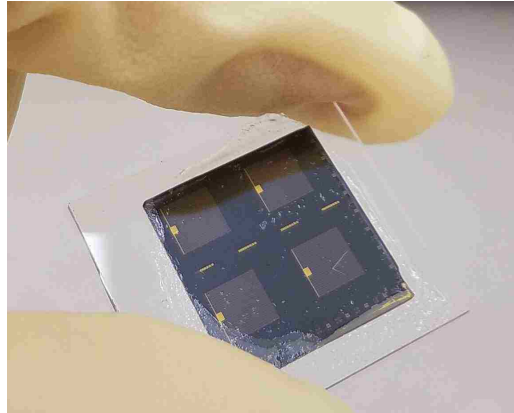**FIG 5.6.** IMAGE OF INGAAS CELLS BONDED TO GLASS CARRIER

5.4.3 Removing the Substrate

The sample is immersed in a HCl:H$_2$O (4:1) solution to etch away the substrate. The reaction of the dilute HCl with InP is instantaneous. As soon as the sample is immersed in the HCl solution bubbling occurs as shown in Fig. 5.7. The bubbling is an indication that gas has formed.


FIG 5.7. IMAGE OF HCL ETCHING INP

Notten *et al.* proposed a two-step chemical mechanism for the dissolution of InP in concentrated HCl solutions that explains the formation of gas [18]. The first step in the mechanism presented is the exchange of bonds between the surface atoms of the substrate and atoms of the HCl molecules. In this step, the original H-Cl and In-P bonds are replaced with In-Cl and P-H bonds as illustrated by the reaction below [18].
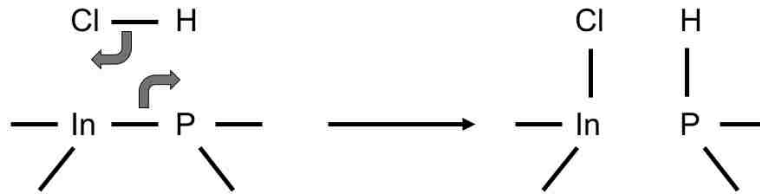
In the second step, the two remaining bonds of indium and phosphorus to neighboring atoms are broken to break free from the lattice and form new bonds with the chlorine and hydrogen atoms as illustrated by reaction 2. In summary, Indium dissolves as Indium trichloride ($InCl_3$), and phosphorus evolves as phosphine (PH_3) gas.
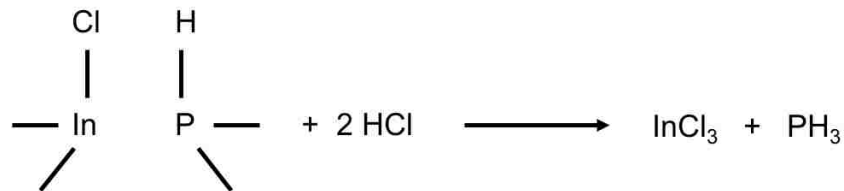
A 500 μm thick InP substrate for a sample of 2 cm x 2 cm can be dissolved in approximately 2 hours. After complete removal of the InP substrate, the sample is rinsed with DI water and dried with nitrogen. Fig 8 shows the sample after removing the InP substrate.
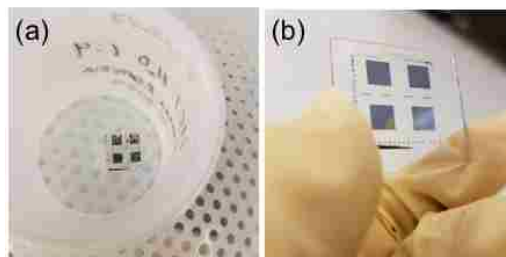

FIG 5.8. IMAGE OF SAMPLE (A) IN HCL AFTER INP IS ETCHED AWAY (B) CLOSER LOOK AFTER SAMPLE IS DRIED

5.4.4 Depositing Bottom Contacts

After the substrate is removed, a metal blanket is deposited on the p^+ - InGaAs surface while the thin film cell still attached to the glass carrier. The metal sequence is the same as for n^+ - InGaAs as Lin's study shows that Pd/Ti/Pt/Au gives the lowest specific contact resistance for both n^+ - and p^+ - InGaAs [17]. The concern on this step is that the adhesive holding the thin film cell to the glass carrier may melt as the temperature in the evaporator chamber during metal deposition can be high. Indeed, the adhesive melts but only on the edges of the sample. However, if the adhesive layer is thin enough, not sing of melting appear as shown in Fig 5.9. At this point, the end product is a fully process thin film TPV cell ready to be released from the host substrate.
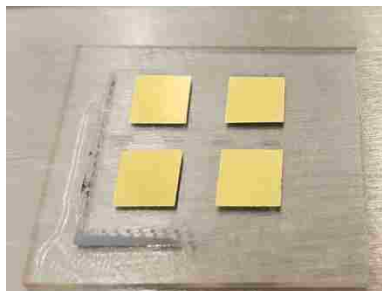
FIG 5.9. IMAGE OF THIN FILM SAMPLE AFTER BACK CONTACT METAL DEPOSITION

5.4.5 Releasing Thin film TPV Cell from Carrier

Releasing the thin film TPV cell from the host substrate is straight forward. The sample is simply left in acetone overnight. Fig 5.10 shows the samples released from the carrier. Once the acetone dissolves the adhesive, the glass carriers are removed from the container, and the acetone is replaced with DI water. Then, the fully processed devices float on the surface of the water as shown in Fig 5.10a. The problem arises in the next step where the delicate film devices need to be transferred to the final substrate, CVD diamond in this case. The thin films are extremely

fragile that they break into pieces with minimum handling as seen in Fig 5.10b.

FIG 5.10. IMAGE OF THIN FILM SAMPLE AFTER (A) BEEN RELEASED FROM THE CARRIER
AND (B) ATTEMPT TO TAKE OUT OF THE SOLUTION

After trial and error, the solution to this problem was to make the back-contact metal thicker.
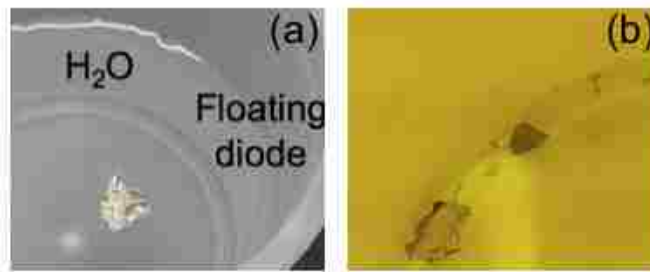
Therefore, a 1 µm thick Ag layer is deposited before the 300 nm Au cap layer during the back-contact metallization. The support that the thick metal layer gives to the InGaAs film facilitates

the transferring process. Fig 5.11 shows yield of thin film InGaAs cells and how they can be

handled with the tweezers without breaking into pieces.
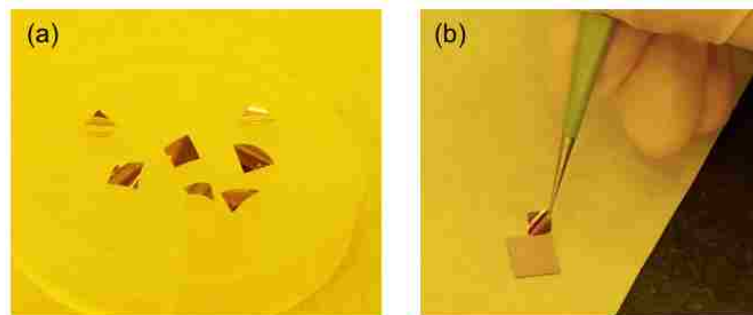
FIG 5.11. IMAGE OF (A) YIELD OF THIN FILM INGAAS CELLS AND (B) TRANSFER OF THIN CELL TO CVD DIAMOND

5.4.6 Bonding the Thin Film TPV Cell to the CVD Diamond Heat Spreader

The InGaAs diode is bonded to the diamond heat spreader by using Au-Au cold-welding

technique [14]. First, the surface of the CVD diamond heat spreader is coated with Ti, Pt, and

Au via electron-beam evaporation with a thickness of 50 nm, 50 nm, and 300 nm respectively.

Next, the thin film TPV cell is transferred to the Au coated CVD diamond, and the stack is

placed in a graphite press as shown in Fig 5.12. Then the graphite press is placed inside an oven

at 250 ºC for 15 min. This boning technique is also used with Au coated Kapton plastic films as shown in Fig 5.12c.

FIG 5.12. IMAGE OF (A) THIN FILM INGAAS CELL ON AU COATED CVD DIAMOND BEFORE BONDING, (B) GRAPHENE PRESS USED FOR BONDING, AND (C) THIN FILM CELL AFTER BONDING

5.5 Characterization of Thin Film InGaAs Devices

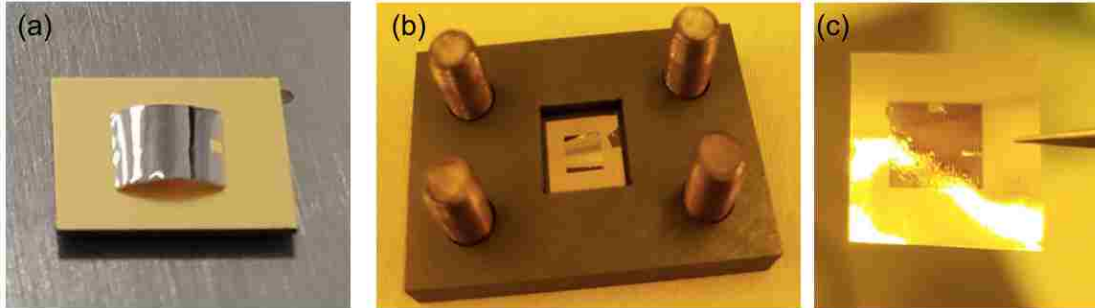Fig 5.13 shows the J-V characteristics, under AM1.5G illumination, for the expected ideal InGaAs cell, the thin film InGaAs TPV cell on the CVD diamond, and the InGaAs cell on the growth substrate. Assuming 100% quantum efficient for all photons greater than 0.75 eV, an ideal InGaAs cell can have an open-circuit voltage (V_{OC}) of 0.40 V, a short-circuit current density (J_{SC}) of 57.6 mA/cm^2, a fill factor (FF) of 77%, and an efficiency (η) of 17.88%. The 0.5 cm x 0.5 cm InGaAs cell on InP substrate without anti-reflection coating (ARC) exhibits an V_{OC} of 0.265 V, a J_{SC} of 39 mA/cm^2, a FF of 61%, and a η of 6.36%. In comparison, the same size thin-film cell on CVD diamond with a SiN$_4$ ARC shows a V_{OC} of 0.275 V, a J_{SC} of 61 mA/cm^2, a FF of 58%, and a η of 9.79%. The SiN$_4$ ARC helps the thin-film InGaAs cell achieve a J_{SC} close to that of the ideal InGaAs cell. The J_{SC} of the thin-film is higher than the ideal probably due to a slightly higher power density of the sun simulator than the normalized one sun. The thin-film InGaAs TPV cell outperforms the cell remaining on the growth due to the difference in ARC. For a fair comparison, a new sample was grown to fabricate a new batch of cells where all cells

either have or not have ARC. The J-V characteristics of the new batch for the samples on the substrate are presented in Fig 5.14. The V_{oc} of the devices has improved considerably now it is getting closer to the ideal V_{oc} of 0.40 V. This is probably due to the better crystal quality of the improved lattice-matching.
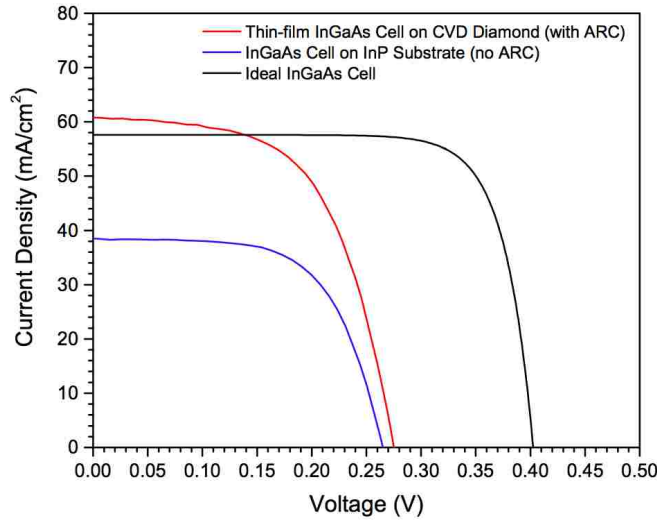

FIG. 5.13. J-V CHARACTERISTICS OF THIN AND THICK INGAAS TPVS UNDER AM1.5G ILLUMINATION
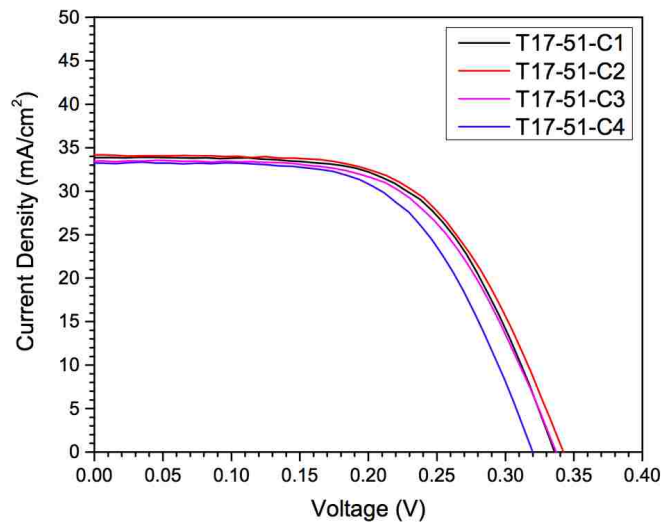
FIG. 5.14. J-V CHARACTERISTICS OF SUBSTRATE BASED INGAAS TPVS UNDER AM1.5G ILLUMINATION

Fig 5.15 shows the new results for the substrate based and thin-film based InGaAs cells without anti-reflection coating. The performance of the thin-film cell on CVD diamond is close to the performance of the InGaAs cell on the InP substrate. The enhanced performance of the previous thin-film cell was only due to the anti-reflection coating.
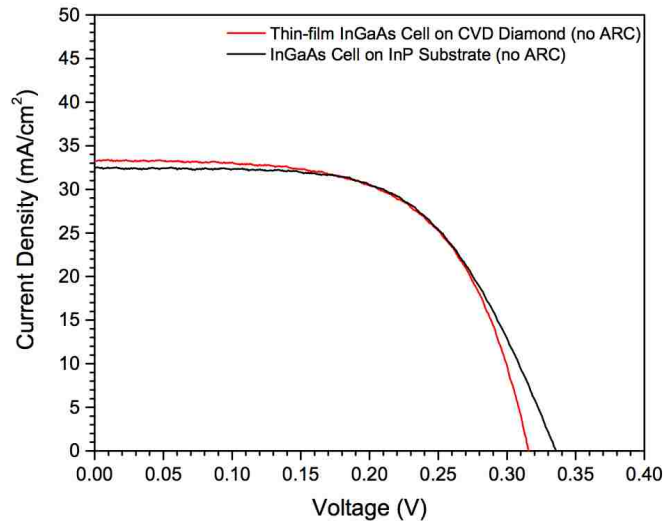
FIG. 5.15. J-V CHARACTERISTICS OF INGAAS TPVS WITHOUT ANTI-REFLECTIVE COATING UNDER AM1.5G ILLUMINATION

5.6 Conclusion

The fabrication and integration of thin film InGaAs TPV cells to CVD diamond have been successful. Thin-film InGaAs TPV cells lattice matched to InP substrates have a great potential to increase the overall efficiency of a TPV system. In the near future, the ELO of InGaAs from InP will be developed to to be able to reuse the InP substrate and reduce the cost of the cells.

References

1. Jain, R. K., Wilt, D. M., Jain, R., Landis, G. A., & Flood, D. J. (1996, February). Lattice-matched and strained InGaAs solar cells for thermophotovoltaic use. In AIP Conference Proceedings (Vol. 358, No. 1, pp. 375-386). AIP.

2. Wanlass, M. W., Ahrenkiel, S. P., Ahrenkiel, R. K., Carapella, J. J., Wehrer, R. J., & Wernsman, B. (2004, November). Recent Advances in Low-Bandgap, InP-Based GaInAs/InAsP Materials, and Devices for Thermophotovoltaic (TPV) Energy Conversion. In AIP Conference Proceedings (Vol. 738, No. 1, pp. 427-435). AIP.

3. Sharps, P. R., & Timmons, M. L. (1996, February). Development of p-on-n GaInAs TPV devices. In AIP Conference Proceedings (Vol. 358, No. 1, pp. 458-466). AIP.

4. Wojtczuk, S. (1995, July). InGaAs TPV Experiment-based Performance Models. In Second NREL TPV Conference (p. 387).

5. Wilt, D. M., Fatemi, N. S., Hoffman Jr, R. W., Jenkins, P. P., Brinker, D. J., Scheiman, D., ... & Jain, R. K. (1994). High efficiency indium gallium arsenide photovoltaic devices for thermophotovoltaic power systems. *Applied physics letters*, *64*(18), 2415-2417.

6. Emziane, M., Nicholas, R. J., Rogers, D. C., & Cannard, P. J. (2007, February). Fabrication and Assessment of Optimized InGaAs Single-Junction TPV Cells. In AIP Conference Proceedings (Vol. 890, No. 1, pp. 149-156). AIP.

7. Phatak, S. B., & Kelner, G. (1979). Material-Selective Chemical Etching in the System InGaAsP/InP. Journal of The Electrochemical Society, 126(2), 287-292.

8. Conway, K. L., Dentai, A. G., & Campbell, J. C. (1982). Etch rates for two material selective etches in the InGaAsP/InP system. Journal of Applied Physics, 53(3), 1836-1838

9. Stano, A. (1987). Chemical etching characteristics of InGaAs/InP and InAlAs/InP heterostructures. *Journal of the Electrochemical Society*, *134*(2), 448-452.

10. He, Y., Liang, B. W., Tien, N. C., & Tu, C. W. (1992). Selective chemical etching of InP over InAlAs. Journal of The Electrochemical Society, 139(7), 2046-2048.

11. Tong, M., Nummila, K., Ketterson, A. A., Adesida, I., Aina, L., & Mattingly, M. (1992). Selective Wet Etching Characteristics of Lattice-Matched InGaAs/InAlAs/InP. Journal of The Electrochemical Society, 139(10), L91-L93.

12. C. Seassal, J.L. Leclercq, and P. Viktorovitch, J. Micromech. Microeng. 6, 261 (1996).

13. Schumacher, H., Gmitter, T. J., LeBlanc, H. P., Bhat, R., Yablonovitch, E., & Koza, M. A. (1989). High-speed InP/GaInAs photodiode on sapphire substrate. Electronics Letters, 25(24), 1653-1654.

14. Lee, K., Shiu, K. T., Zimmerman, J. D., Renshaw, C. K., & Forrest, S. R. (2010). Multiple growths of epitaxial lift-off solar cells from a single InP substrate. Applied Physics Letters, 97(10), 101107.

15. Bailey, S. G., Wilt, D. M., DeAngelo, F. L., & Clark, E. B. (1993, May). Preferentially etched epitaxial liftoff of indium phosphide. In Photovoltaic Specialists Conference, 1993., Conference Record of the Twenty Third IEEE (pp. 783-785). IEEE.

16. Hall, E., Kroemer, H., & Coldren, L. A. (1999). Improved composition control of digitally grown AlAsSb lattice-matched to InP. Journal of crystal growth, 203(3), 447-449.

17. Lin, J. C., Yu, S. Y., & Mohney, S. E. (2013). Characterization of low-resistance ohmic contacts to n-and p-type InGaAs. Journal of Applied Physics, 114(4), 044504.

18. Notten, P. H. L. (1984). The etching of InP in HCl solutions: a chemical mechanism. Journal of The Electrochemical Society, 131(11), 2641-2644.

Chapter 6: Conclusions and Future Work

The fabrication of large area (1 cm x 1 cm) GaSb TPV cells with good diode behavior were achieved after mitigating the highly-faceted defects and irregular defects that occurred during growth. The epitaxial lift-off of small area GaSb epitaxial layers from GaSb substrates was demonstrated despite the lack of high selectivity in the InAs/AlSb/GaSb material system. However, techniques to achieve larger ELO GaSb films without etching the edges remain to be explored.

While solving the issues in GaSb homoepitaxy, GaSb epitaxial layers were grown on GaAs substrates by inducing arrays of 90 º misfit dislocations at the GaSb/GaAs interface. This technique was expected to reduce the propagation of threading dislocations into the GaSb epitaxial layer and allow the release of GaSb epi-layers since the etch chemistry in GaAs systems is well understood and highly selective. Indeed, the isolation of GaSb membranes from GaAs was successfully by substrate removal and epitaxial lift-off techniques. However, the residual threading dislocations due to the lattice-mismatch degraded the performance of the metamorphic devices. Achieving thin film metamorphic GaSb devices is promising if the threading dislocation density in the GaSb epitaxial layer is further reduced.

To improve the performance of these metamorphic GaSb TPV devices, two techniques were investigated to further reduce the propagation of threading dislocations to the p-n junctions. One technique focused on further minimizing the formation of threading dislocations and the other technique focused on blocking the propagation of such dislocations into the p-n junction of the devices. The combination of these techniques allowed the improvement of leakage current and open circuit voltage of the metamorphic GaSb solar cells.

Finally, the integration of thin-film narrow-bandgap TPV devices to CVD diamond heat spreaders was demonstrated by growing lattice-matched InGaAs TPVs on InP substrates. In this system, there are no threading dislocations and the substrate removal etch chemistry is well understood and highly selective.

6.1 Future Work

The InAs/AlSb/GaSb material system lacks the two key elements for successful epitaxial lift off. There is no high selectivity between the sacrificial layer and the film to be released, and there is no curvature of the GaSb epitaxial films as it is being released from the substrate. Hence for the future releas of GaSb epitaxial films from GaSb substrates, a solution to lack of selectivity and lack of curvature must be found.

A possible way to increase the selectivity of the sacrificial layer will be by growing alternative layers of materials with high selectivity and low selectivity such as AlAs and AlSb as shown in Fig 6.1. Materials with different properties can be grown this way even when they are not lattice matched. Thin layers of lattice mismatched materials can be grown without any strain if the critical thickness is not exceeded. It would be important that the stack of sacrificial layer begins and ends with the highly selective material to prevent damage to the GaSb epitaxial film. Although, the use of InAs protective layers will also be useful to release large area undamaged GaSb films.
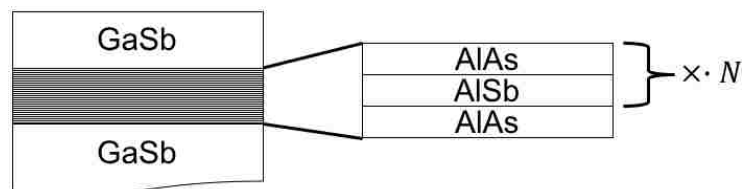

FIG 6.1 SCHEMATIC OF A STRUCTURE TO INCREASE THE SELECTIVITY OF THE SACRIFICIAL LAYER

Regarding the lack of curvature, it would be important to figure out what strain can be used to induce curvature of the GaSb film as it is being released from the substrate. Perhaps mechanical stress from a metal coat or built in mechanical stress in the epitaxial structure. The lack of curvature slows down the etching of the AlSb sacrificial layer by preventing the exchange of reactants and products. The AlSb sacrificial layers present a much lower etch rate than AlAs sacrificial layers in diluted hydrofluoric acid. Hence, a better understanding of the etching of AlSb epitaxial layers is essential.

For the InGaAs TPV cells, it would be ideal to release the InGaAs cells from their InP substrate by epitaxial lift off since the substrate can be used again, and hence, the cost of the cells can be reduced. As explained in chapter 5, $AlAs_{0.56}Sb_{0.44}$ is an ideal candidate to act as a sacrificial layer in the release of $In_{0.53}Ga_{0.47}As$ epitaxial layers from InP substrates as it is lattice-matched to them and can be etched away with hydrofluoric acid due to its 100 % Al composition.

However, to use the ELO technique, the bottom-side approach for the integration of ELO films to the CVD diamond heat spreaders should be optimized. When attempted, the bottom-side approach for ELO was not successful. The high aluminum content window layers and one of the metals in the contact-metal stack reacted with the etchant. Hence, the side walls of window layer should be protected, and the metal sequence must be designed so that it does not get etched by HF and still forms good ohmic contacts. In addition, bonding the sample to a plastic carrier is not practical for TPVs. However, plastic carriers are not needed anymore since the cells seem to have enough support to stand free with at least 1μm thick metal on their surface. Once the ELO problems are solved, the freestanding thin-films can be transferred and bonded to CVD diamond just as it was done for the freestanding InGaAs TPV cells after etching away the InP substrate.

Hence, the remaining step to be optimized is the photolithography steps to be able to fabricate the top contacts.